Department of Physics
University of Jyväskylä
Research Report No. 7/2010

Fission yield studies with SPIG-equipped IGISOL: A novel method for nuclear data measurements

by
Pasi Karvonen

Academic Dissertation
for the Degree of
Doctor of Philosophy

To be presented, by permission of the
Faculty of Mathematics and Natural Sciences
of the University of Jyväskylä,
for public examination in Auditorium FYS-1 of the
University of Jyväskylä on September 24, 2010
at 12 o'clock noon

Jyväskylä, Finland
September 2010

Preface

The work reported in this thesis was carried out in the IGISOL group during the years 2004-2010 at the Department of Physics of the University of Jyväskylä, Finland.

I would like to thank my supervisors Docent Heikki Penttilä and Professor Juha Äystö for the opportunity to work in the IGISOL group and for all encouragement and guidance. I am also grateful to all the past and present members of the IGISOL group who have supported me during this laborious but very fascinating process. In particular, I would like to warmly thank Dr. Arto Nieminen for the original design of the SPIG system, Dr. Tetsu Sonoda for all support in the development of the present SPIG, Dr. Andrey Popov for various gas flow simulations and Dr. Iain Moore for all English corrections, guidance and expertise. The JYFLTRAP group deserves acknowledgment for providing us a fantastic instrument for the fission yield studies.

In general, I wish to thank all JYFL workers for the pleasant working atmosphere. It would not have been possible to carry out this work without the expertise of the staff of the electronics and mechanical workshops and I am thankful to them for all discussions and advice, and for patience in carrying out most of my ideas and designs.

I would like to thank Mr. Juha Keränen for numerous coffee break discussions and fishing trips, greatly counterbalancing the work behind this thesis. I am also grateful to my parents and sisters and their families for all encouragement and support and to my parents-in-law for ”wife”- and babysitting, which greatly helped me to concentrate on the writing of this work. I am forever thankful to my lovely wife, Elina, who has patiently stood beside me through all good and not so good times, and to our wonderful sons, Lauri and Kalle, for keeping priorities in right order. Finally, I would like to remember our deceased daughter Martta. Although I never had a chance to meet her alive, she taught to me more about the real life than anyone can ever do.

Jyväskylä, September 2010
Pasi Karvonen

Author

Pasi Karvonen
Department of Physics
University of Jyväskylä
Finland

Supervisors

Docent Heikki Penttilä
Department of Physics
University of Jyväskylä
Finland

Prof. Dr. Juha Äystö
Department of Physics
University of Jyväskylä
Finland

Reviewers

Priv. Doz. Dr. Peter Thirolf
Faculty of Physics
Ludwig Maxmillians Universiteit
Munchen, Germany

Dr. Franz-Joseph Hambsch
Institute for Reference Material and Measurements
EC Joint Research Centre
Geel, Belgium

Opponent

Prof. Dr. Peter Dendooven
Kernfysisch Versneller Instituut
University of Groningen
Netherlands

Abstract

Karvonen, Pasi
Fission yield studies with SPIG-equipped IGISOL:
A novel method for nuclear data measurements
Jyväskylä: University of Jyväskylä, 2010, xii + 158 pp.
Department of Physics, University of Jyväskylä, Research Report 7/2010.
ISBN (pdf) 978-951-39-4025-6
ISBN (paper copy) 978-951-39-4024-9
ISSN 0075-465X

This thesis work consists of two sections. In the first section, the development of a so-called Laser Ion Source Trap (LIST) device is described. The LIST device is based on a double SPIG (SextuPole Ion Guide) system, providing the possibility to improve the elemental selectivity of the IGISOL method via highly discriminative laser ionization occurring outside the ion guide. The improved selectivity enables the production of isotopically pure beams. The double SPIG can be used without laser ionization and replaces the conventional skimmer electrode. In this work, the SPIG is compared to the skimmer and is shown to remarkably improve both the efficiency and beam quality of the IGISOL facility.

The second section introduces a novel method for isotopic fission yield measurements. Accurate fission product yield data are important in many fields of physics. Previous experimental techniques are either limited to certain mass regions of the fission products, or lead to inaccurate and/or time consuming yield deduction. The technique described in this work is a successful combination of the universal IGISOL method and an unambiguous isobaric purification of the JYFLTRAP facility. This combination is able to provide pure samples of almost any isotope produced in fission. These samples are directly counted using a highly sensitive MCP - detector, significantly shortening the measurement time as compared to traditional detection methods such as a γ-spectroscopy.

Acknowledgments

This work has been supported by the Academy of Finland under project Production and research of exotic nuclei at the IGISOL (project No. 202256 and No. 111428) as well as the Finnish Centre of Excellence Programme 2000-2005 (Project No. 44875: Nuclear and Condensed Matter Physics Programme at JYFL) and the Finnish Centre of Excellence Programme 2006-2011 (Project No. 213503, Nuclear and Accelerator Based Physics Programme at JYFL), and by European Union within EURISOL design study.

Author of this work expresses gratitude for financial support from the rector of the University of Jyväskylä. The Graduate School in Particle and Nuclear Physics (GRASPANP) is acknowledged for financing travels to schools and conferences.

Contents

List of Tables

List of Figures

1. Introduction

The ion guide technique, a powerful tool for producing very exotic isotopes, was developed at the University of Jyväskylä in the early 1980's [1, 2]. The speed and chemical non-selectivity of the technique allow the production of very short-lived isotopes of almost any element. The weaknesses of the original concept were a high energy spread of the transported beam and a relatively poor transport efficiency between the ion guide and mass separator achieved by a static electric field. The situation improved about ten years later, when the static field was replaced by a radiofrequency (rf) field and a SPIG (SextuPole Ion Guide) apparatus which was introduced for the first time in [3]. The use of the SPIG reduces the energy spread of the transported beam and improves the efficiency as compared with the skimmer-based technique.

The non-selectivity is a unique, but not always desirable feature of the technique. In many cases, only few particular isotopes produced in nuclear reactions are of interest and other isotopes and particularly molecular ion beams only make the reaching of this goal more difficult. A concept based on laser ionization of neutral reaction products inside a LIST (Laser Ion Source Trap) apparatus, physically separated from the ion guide was introduced in 2004 [4]. A laser ionization scheme represents a probe of the unique fingerprint of an element and therefore it is possible to produce ion beams with a very high selectivity. The LIST device developed in this work is based on a double SPIG system, whose physical dimensions match the properties of the FURIOS laser system [5]. The same device can also be used as a traditional SPIG without laser ionization.

The performance of the double SPIG system in an ion guide mode without the laser system is studied via several reactions and ion guides. The results are compared with the traditional skimmer system, showing a general yield improvement of a factor of 5 for the SPIG in fission reactions. An even higher improvement is reached in light-ion fusion evaporation reactions leading to a factor of ∼8 higher yields as compared to the skimmer system. It is, however, quite surprising that the SPIG has not been able to provide any improvement in heavy-ion fusion evaporation reactions. In addition to the transmission efficiency, the SPIG also improves the resolving power of the mass analysis after the dipole magnet of the IGISOL. A general improvement factor of ∼2 is seen in the $A = 100$ mass region, being slightly better for lower masses and slightly worse for heavier, respectively. In order to understand the operation of the SPIG under different conditions, a set of ion optic simulations has been performed using SIMION3D ion optics simulator [6]. The results of the simulations are compared to the results of experimental measurements where possible, showing a very good agreement especially in the transmission efficiency of the SPIG.

The chemical non-selectivity of the ion guide method can be an advantage and has been utilized in isotopic fission yield measurements. Yield distribution data from fission reactions induced by various projectiles and projectile energies on several different actinide targets are required for the development of fission models such as [7] and next generation ISOL-based facilities such as EURISOL [8], for example. Additionally, yield distributions provide valuable information for next generation nuclear power plant development. In particular, reactors utilizing energetic neutron-induced fission do not produce significant amounts of radiotoxic minor actinides via neutron capture processes. The yield distributions for higher neutron energies are however insufficiently known. New experimental data are needed both for simulations and model development [9–11].

Fission reactions and independent yield distributions in thermal neutron-induced fission are well studied resulting in rather complete fission yield distributions for the low mass region of fission products of various actinides. These distributions are mainly produced using reactor-coupled recoil separators such as Lohengrin [12] coupled to the ILL high-flux reactor in Grenoble. However, the present available experimental data from independent and even relative isotopic fission yields for proton- and fast neutron-induced fissions are extremely sparse. The ion guide technique is a very efficient tool for exploring such distributions. The difficulty of a proper fission yield determination with the ion guide technique has been mainly related to the insufficient mass resolving power for isobaric separation. The only way to resolve isotopes from each other has been via studies based on radioactivity. This has been a problem in particular for the yields of the most neutron-rich species, since their decay schemes are often poorly known.

At traditional ISOL facilities the chemical selectivity of the ion production technique allows the use of direct ion counting [13, 14]. This has made possible the efficient measurement of the yields of isotopes produced in fission after only modest mass separator resolution. However, these studies have been limited to highly volatile elements only.

The first on-line test of the double SPIG system at JYFL was a fission yield experiment. This experiment was the second of three experiments, which were used in the development of a novel method for the fission yield determination with a Penning trap. The new method is a combination of the non-selectivity of the ion guide technique with high efficiency ion counting after isobaric purification provided by JYFLTRAP [15]. This combination provides an accurate and fast deduction of the isotopic fission yield distributions for a large number of fission products.

The development of the new method is introduced in this work. Possible sources of errors and mass dependencies of the both the IGISOL and JYFLTRAP facilities are carefully studied and the analysis process of the measurement data is described in detail. The results of the new method are compared with the existing data produced with and without the ion guide technique. The adequacy of the JYFLTRAP purification and MCP (Multi Channel Plate) detector-based ion counting is tested by comparing the results with the data measured by both direct ion counting and γ-ray spectroscopy. In all aforementioned cases, the agreement between the existing data and the data produced with the new method is generally good, although difficulties related to yield fluctuations disturbed the analysis in this work and led to the reduced accuracy of the yield data in some cases.

This work has been partially reported in the following publications:

1. **LIST developments at IGISOL.**
   P. Karvonen, T. Sonoda, I. D. Moore, J. Billowes, A. Jokinen, T. Kessler, H. Penttilä, A. Popov, B. Tordoff and J. Äystö.
   Eur. Phys. J. Special Topics 150, 283-284 (2007).

2. **A sextupole ion beam guide to improve the efficiency and beam quality at IGISOL.**
   P.Karvonen, I.D.Moore, T.Sonoda, T. Kessler, H. Penttilä, K. Peräjärvi, P. Ronkanen and J. Äystö.
   Nucl. Instr. and Meth. B 266 (2008) 4794-4807.

3. **Determining independent fission product yields with a Penning trap.**
   H. Penttilä, P. Karvonen, T. Eronen, V-V. Elomaa, U. Hager, J. Hakala, A. Jokinen, A. Kankainen, I. D. Moore, K. Peräjärvi, S. Rahaman, S. Rinta-Antila, V. Rubchenya, A. Saastamoinen, T. Sonoda, and J. Äystö.
   Eur. Phys. J. A 44, 147-168 (2010).

4. **Upgrade and yields of the IGISOL facility.**
   P. Karvonen, H. Penttilä, J. Äystö, J. Billowes, P. Campbell, V-V. Elomaa, U. Hager, J. Hakala, A. Jokinen, A. Kankainen, I.D. Moore, K. Peräjärvi, S. Rahaman, S. Rinta-Antila, J. Rissanen, J. Ronkainen, A. Saastamoinen, T. Sonoda, B. Tordoff, and C. Weber.
   Nucl. Instr. and Meth. B 266 (2008) 4454-4459.

2. Sextupole ion guide development at IGISOL

One of the main subjects of this thesis work is the development of the SextuPole Ion Guide (SPIG), used as a coupling element between an ion guide and mass separator. The use of the SPIG to guide ions is not a new invention; it was originally developed at the Institute for Nuclear Study at the University of Tokyo in the early 1990's in order to improve the beam quality of the traditional, skimmer-based IGISOL technique [3]. The SPIG structure was later adapted to the LISOL (Leuven Isotope Separator On-Line) separator facility at Louvain-la-Neuve [16] and it was also tested at the IGISOL facility, JYFL, in connection with HIGISOL ion guide developments [17].

The SPIG system introduced in this work differs from the aforementioned sextupole ion guides mainly because of additional operational modes. Although the most common application of the present SPIG system is the ion guiding mode as it was originally proposed in [3], it has been designed to act as a LIST (Laser Ion Source Trap) device together with the FURIOS laser ion source system [5]. A detailed description of the development of the SPIG system is given in this chapter as well as a short description of the traditional IGISOL method. The operation of the SPIG is explained via simulations and its performance at IGISOL as compared to the traditional skimmer electrode is shown with a few experimental results.

2.1. An introduction to the traditional IGISOL method

The traditional IGISOL, Ion Guide Isotope Separator On-Line, method was first developed at the University of Jyväskylä in the early 1980's. The idea of the method is to produce mass separated secondary beams of radioactive isotopes directly from nuclear reactions. This method is applicable for producing isotopes of almost any element within very short time scales, which makes it a fascinating tool for the studies of exotic and short-lived isotopes. More detailed description of the development of the IGISOL technique and different types of ion guides can be found in [18–20] and references therein.

The principle of the traditional IGISOL method is shown in Fig.2.1. Radioactive isotopes are produced via nuclear reactions by bombarding a thin stationary target with a medium energy (typically tens of MeV per nucleon) primary beam. The thin target is one of the key features of the IGISOL method: a significant fraction of the reaction products have enough recoil energy to pass through the target. The reaction products enter a buffer gas filled chamber, which is generally called an ion guide or a gas catcher (right in the figure). While the energy of the highly charged products is dampened due to numerous collisions with the buffer gas atoms, their charge states are also reduced via charge exchange reactions both with the buffer gas and the impurities such as nitrogen, oxygen and noble gases. Due to the high ionization potential of the buffer gas (usually helium), a considerable fraction of the products retains the charge state of +1 as they are finally exited from the ion guide within the buffer gas flow. The evacuation time of the products typically varies from sub-millisecond scale to several hundreds of milliseconds mainly depending on the buffer gas type, the geometry and size of the buffer gas volume and the aperture of the exit nozzle.

Another key feature of the IGISOL technique is the differential gas pumping system. Buffer gas flowing out from the ion guide is removed from the vacuum system within a few steps before the ions are accelerated up to the full 30 - 40 keV energy. After ejection from the ion guide the products enter the first section of the pumping system. In this section, ions are separated from the buffer gas by a cone shaped skimmer electrode (in the middle of the figure) having a typical aperture size of $\sim$1 mm and an electrical potential of several hundred volts with respect to the ion guide. A relatively high electric field is required for effective overcoming of the scattering effect caused by a high, of order 1 mbar background pressure in the skimmer - ion guide zone. The ions that survive through the skimmer aperture are accelerated towards the mass separator by an extractor electrode (left in the figure) located in the second differential pumping section. A typical gas pressure in this section is already as low as 10^{-3} - 10^{-4} mbar making it possible to transfer the products with only a minimal number of ion - gas atom collisions. A final acceleration to the ground potential takes place just after the extractor electrode in the third, high vacuum pumping section wherein the gas pressure is of order of 10^{-6} mbar. The mass separation of the accelerated ions is done using a 55° electrical dipole magnet that separates the ions according to their mass and charge ratio. A beam of desired m/q - ratio is selected by slits located at the focal plane of the dipole and transferred to the measurement stations or to JYFLTRAP [15] for further studies.

Although the ion guide method provides a fast and universal tool for the production of very exotic nuclei, it has some disadvantages. The efficiencies of the traditional ion guides are usually quite poor, typically well below 1 % although efficiencies up to 10 % have been reached in light-ion induced fusion reactions with light-ion ion guides. In addition to the poor efficiency, the energy spread of the beam, especially when the skimmer electrode is used, is typically a few 10 - 100 eV

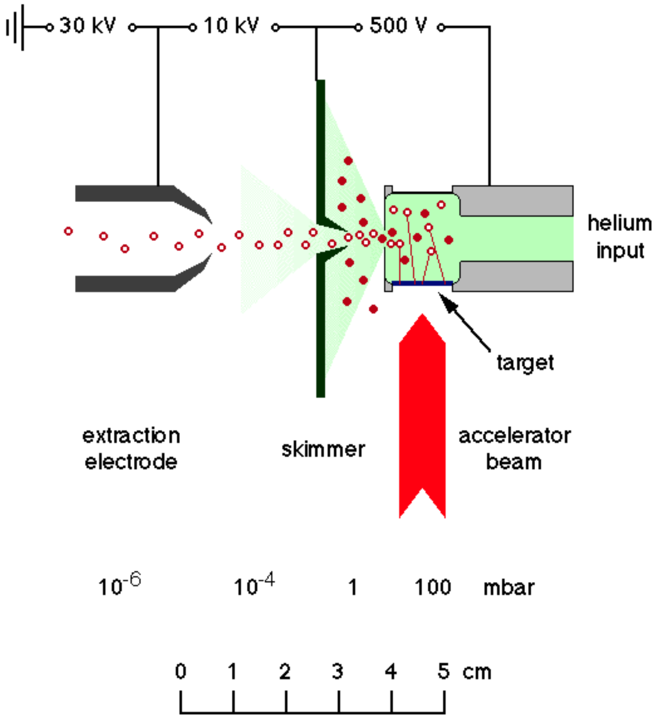

Figure 2.1.: The principle of the ion guide technique. The nuclear reaction products emanating from the target material are captured inside the buffer gas filled stopping volume, thermalized as 1^+ ions and finally accelerated towards the mass separator. Typical acceleration voltages and buffer gas pressure ranges are also shown [21].

depending on the gas pressure in the skimmer zone as well as on the potential difference applied between the skimmer electrode and the ion guide. This energy spread leads to a low mass resolving power (MRP, $M/\Delta M$) of the beam after the separator. Even though the typical MRP of 200 - 300 provided by the skimmer electrode is suitable for traditional decay spectroscopy purposes, it definitely causes some limitations for further beam manipulation techniques such as ion trapping and laser spectroscopy.

2.2. Radio-frequency multipoles in general

RF multipoles are rather common devices. Nearly complete theories based on quadrupoles and higher order multipoles can be found in [22] and [23], for example. Therefore, only the information that is needed to describe the functionality of the SPIG is given below. Reference [23] is used as a main source of information.

2.2.1. Characteristics of the multipoles

The basic dimensions and electrical coupling of the linear multipole (sextupole in this case) are shown in Fig.2.2. A multipole order n, often called the multiplicity of a multipole, is expressed as a sum of the rod pairs in the multipole structure (n = 3 for sextupole). Linear multipoles have a cylindrical geometry. The rods, having a radius r_{rod} and a length l_0, are distributed around the center of the multipole in such a way that the angle between adjacent rods equals π/n and the minimum distance between the rod and the center of the multipole is r_0 (inscribed radius). The electrodes that generates an “ideal” multipole field have actually a hyperbolic shape although, due to an easier manufacturing, circular rods are commonly used in practice.

2.2.2. Effective potential approximation

The exact equations of motion of ions in higher order (n>2) multipoles are very complex to solve analytically. Instead, the motion can be studied via simulations as discussed in section 2.4. However, as long as the motion remains adiabatic, the radial potential field generated by the multipole can be approximated using a time-averaged effective potential

$$V_r^* = \frac{q^2 n^2 U_{RF}^2}{4m\omega^2 r_0^2}\left(\frac{r}{r_0}\right)^{2n-2}, \tag{2.1}$$

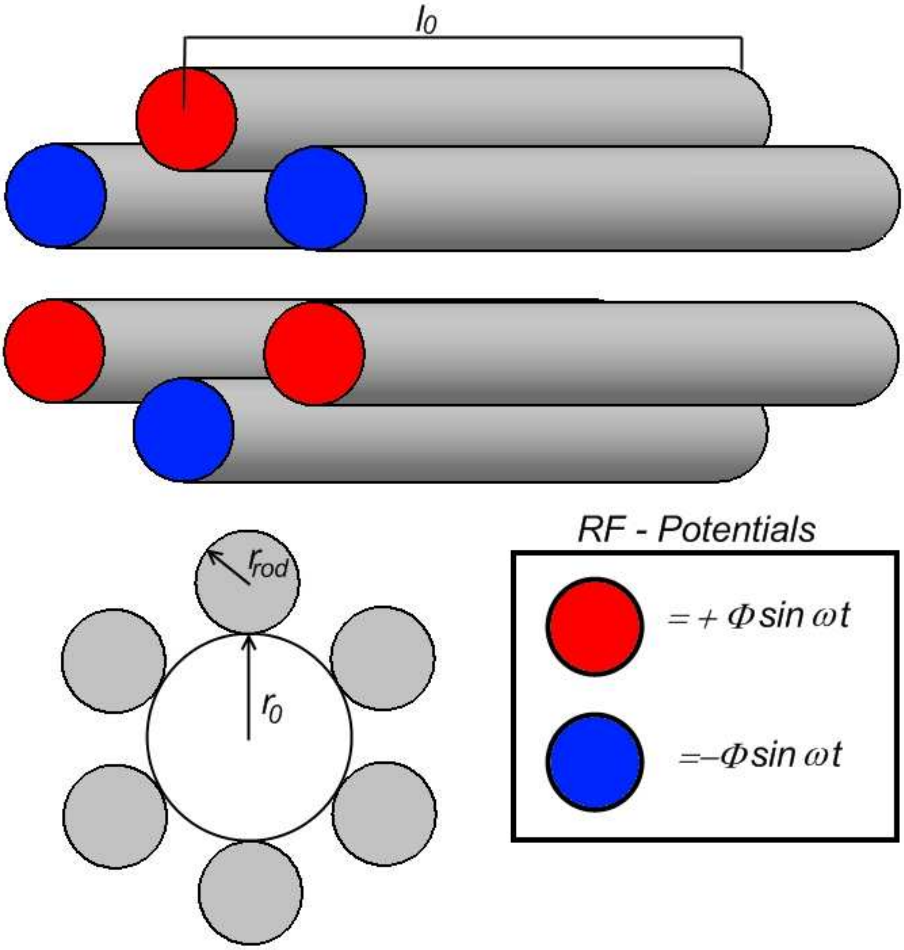

Figure 2.2.: An example of a linear sextupole (n=3) arrangement. Six rod electrodes having a diameter of r_{rod} and a length of l_0 are equally distributed on a circle of radius r_0. Electrical potentials applied to the rods are indicated as red and blue faces. The amplitude of an rf signal, Φ, is the same for all rods while the polarity of adjacent rods is inverted.

where U_{RF} is the amplitude and ω is the angular velocity of the rf signal, q and m are the charge and mass of the ion, respectively, and r is the radius of the ion trajectory with respect to the multipole center.

Fig.2.3 shows normalized shapes and depths of the effective potentials calculated for several multipole types. The higher order multipoles produce a deeper and steeper potential shape than the lower order multipoles. In principle, the deeper the potential well the better the trapping of a charged particle improving the handling of more energetic particles and providing a higher tolerance against charge repulsion effects. A deeper well leads however to an increased flatness of the potential near the multipole center. This flat part of the potential defines the region wherein the particle motion is less disturbed by the rf field.

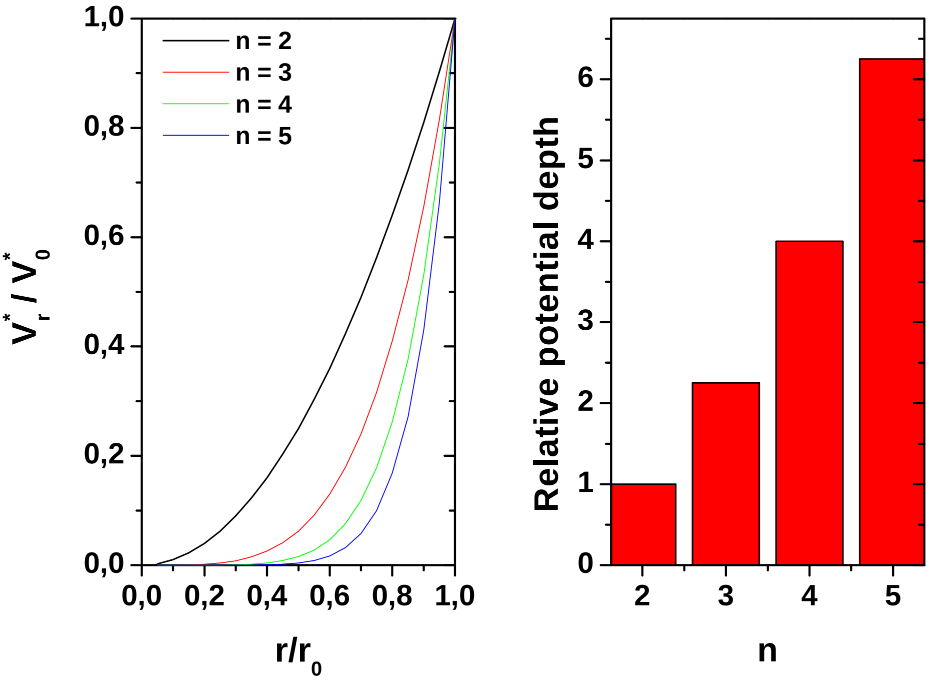

Figure 2.3.: Normalized effective potentials calculated for four different types of multipole (2 = quadrupole, 3 = sextupole, 4 = octupole and 5 = decapole). The shapes of the resultant potentials are illustrated in the left panel, in which the normalized potential as a function of the relative radius r/r_0 is shown. The right panel shows the maximum depths of the effective potential wells of multipoles normalized to that of the quadrupole (n = 2). In all cases, identical operational parameters were used.

2.3. Double SPIG at JYFL

Soon after the major upgrade of the IGISOL facility in 2003 - 2004, a laser ion source project called FURIOS (Fast and Universal Resonant laser IOn Source) was launched [5]. One idea for FURIOS was to improve the selectivity and efficiency of the IGISOL facility by the methods of laser ionization both inside and outside of the gas cell.

2.3.1. Laser ion source trap

A method whereby a selective laser ionization of neutral reaction products occurs inside a laser ion source trap (LIST) device, physically separated from an actual ion source/guide, was first introduced in [4]. This method was originally proposed to improve the selectivity of the resonance ionization laser ion source (RILIS) [24] at ISOLDE, wherein a competitive process, surface ionization due to high temperatures of the ion source, reduces the selectivity gained by the traditional laser ionization. In the original LIST method a segmented rf quadrupole acts as an ion trap for laser produced ions. All unwanted surface ions released from the ion source are repelled by using an electrostatic potential and neutral atoms are guided inside the trap within a gas flow. Inside the trap, the atoms are selectively ionized by laser pulses. These so-called laser ions are cooled down to the thermal velocity of the buffer gas and are finally released as a short bunch towards the mass separator. Two prototypes of the original LIST proposal were developed at the RISIKO off-line separator in Mainz [25]. A total efficiency of order 1 % compared to the conventional laser ion source was observed in [26] during the first tests of these devices. Although the resultant efficiency is rather low, intensities up to several 10^6 ions per 6 μs ion bunch were recorded with high selectivity and beam quality.

The LIST method also offers some advantages for the ion guide based facilities. In light-ion induced-fission reactions for example, a significant number of fragments are lost due to recombination processes in the plasma caused by the fragments themselves passing through the stopping gas. These recombination losses are not a problem if the fragments are allowed to neutralize on purpose inside the ion guide. A laser-based re-ionization process is then applied in a region where the probability of the recombination is significantly lower. In contrast to the lack of selectivity of the ion guide method, laser ionization offers the high selectivity of the reaction products. Laser ionization is based on the atomic energy level separation which forms a unique fingerprint of the element. Therefore only the products that belong to the selected element will be re-ionized by the laser light. After the isotopic mass separation of these products, pure beams of single elements can be expected. In addition to the selectivity of the method, a better beam quality should also be realized. Especially in the case of rf multipoles, the quality of the transported beam is very sensitive to the space charge effect. Since the LIST method utilizes only neutral atoms, the charge density inside the multipoles remains very low and effects due to space charge should be minimized. These effects are discussed in more detail in Section 2.4.5.

In addition to JYFL, the IGISOL-based LIST method has been developed at the LISOL facility in Louvain-la-Neuve. Several possible LIST modes are described in [27]. Instead of a new LIST device, the LISOL LIST was realized with an existing SPIG system. The required charge repulsion was provided by the base dc potential of the SPIG system, which was raised with respect to the ion guide in order to block any positively charged particles. Another solution for repelling the charged particles was also introduced in [27]. In contrast to a longitudinal repulsive electric field, which is rather inefficient for short distances, a transverse electric field was tested. This electric field was generated by so-called ”ion collector” plates located inside the ion guide. Usually a high charge density inside any traditional ion guide prevents the successful transport of ions by using static electric fields, as discussed in [28]. Therefore, the use of this solution requires a special geometry which contains a low charge density region. One example of such a geometry is that of the dual chamber cell, described in [29].

In this work, the LIST method is used together with the ion guide as shown in Fig.2.4. Reaction products are allowed to neutralize inside the ion guide and are transported within a narrow gas jet into a double SPIG structure, which now acts as the LIST device. All positively charged particles are reflected back towards the ion guide using a repulsive electric field generated by a repeller electrode. Neutral atoms are selectively ionized inside the first SPIG element using high repetition rate laser pulses. The laser ions are captured in the rf field, transported through the extractor electrode and finally accelerated towards the mass separator. The LIST process ensures that all ions accelerated towards the mass separator have been produced via highly selective laser ionization. As a result, a substantial increase of the selectivity can be expected. Only the development of the double SPIG system is described in this work, omitting the laser part of the method, which is discussed in more detail in [30].

2.3.2. Dimensions and realization

The original LIST method was proposed to be realized with a segmented rf quadrupole [4], however the earlier experiences from the SPIG strengthened the confidence that higher order multipoles were also sufficient to improve the beam quality and the efficiency of the IGISOL facility. Moreover, the higher order multipoles are able to

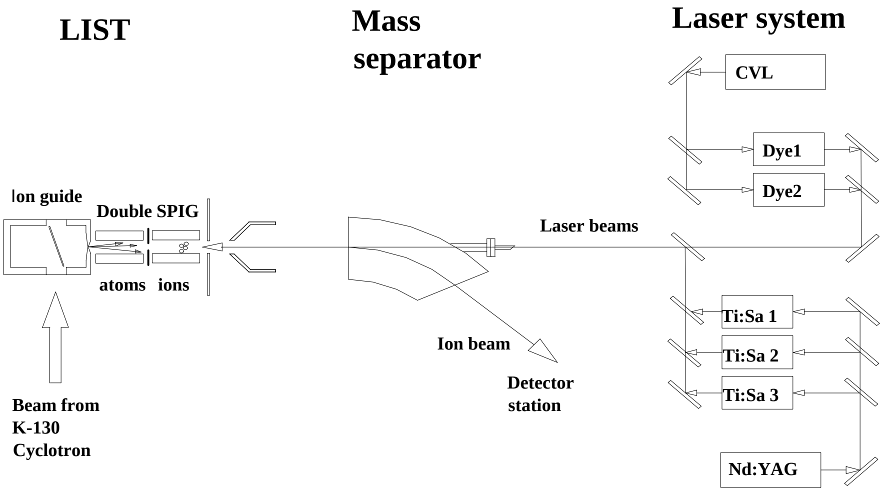

Figure 2.4.: Schematic presentation of the LIST method at IGISOL. See text for more details.

handle the higher charge densities, although at the cost of the beam quality. Therefore a compromise between the charge handling capacity and the beam quality led to the selection of a sextupole structure as a basis of the LIST device.

The LIST device of this work is a so-called double SPIG system originally engineered by A. Nieminen. It was designed to meet the requirements of the LIST method, which means the dimensions of the device were set by the properties of the laser beams from the FURIOS laser facility. The most important dimensions and operating parameters of this double SPIG system are listed in Table 2.1

Studies of the gas jet properties performed in works [30] and [31] revealed the fact that the background pressure in the vicinity of the jet region is an important parameter. An increase in the pressure seems to lead to a narrower gas jet, improving an overlap between neutral atoms and counter-propagating laser beams. Because of this, the SPIG system has been divided into two separate elements, of which the first one, located just after the ion guide, is surrounded by a stainless steel cylinder in order to increase the pressure in that region. The pressure inside the first SPIG element can be coarsely controlled via an adjustable iris separating the SPIG elements. The buffer gas is later pumped away from the SPIG system through the gaps between the rods of the second, open SPIG element.

Table 2.1.: Dimensions and maximum operating parameters of the IGISOL double SPIG system.

Dimension	**Value [mm]**
Repeller aperture	6
Repeller thickness	3
SPIG inscribed radius	5
SPIG rod radius	2
Iris aperture	1-22
SPIG 1 axial length	78.5
SPIG 2 axial length	81.5
Total axial length of the device	165.5
End electrode aperture	6
Parameter	**Value**
RF frequency	3-4 MHz
RF amplitude	max. 300 V_{0-p}
Repeller voltage	0±300 V
SPIG rod dc voltages	0-300 V
End electrode voltage	0-500 V

The desired size of the laser spot is of order 6 mm. This sets the minimum value for the inscribed radius of the sextupole elements as well as for the aperture sizes of both the repeller and the end electrode. Rough simulations that were made in the design phase of the SPIG system showed that an inscribed radius equal or greater than 5 mm is required for a sufficient capturing efficiency with reasonable rf parameters. This radius was thus selected for both sextupole elements. The radius of the stainless steel circular rod electrodes is 2 mm.

The overlap region between the pulsed laser beam and the gas jet has to be long enough for the maximum laser ionization efficiency. This determines the minimum length of the enclosed SPIG element in which the laser ionization occurs. The repetition rate of the laser is 10 kHz which means a time interval of 0.1 ms between the pulses. The maximum axial velocity of neutral particles closely follows the velocity of the buffer gas jet exiting from the ion guide. In the design phase of the SPIG, the gas jet velocity was assumed to be supersonic in nature ($\sim$1000 m/s for He gas). For such a velocity, at least a 100 mm long ionization region is required before the interaction between laser pulses and each atom in the jet can be ensured. For practical reasons, argon is often used in the LIST mode. It has a lower ionization potential and higher recombination coefficient than helium, which makes the neutralization of the reaction products easier. Moreover, it also provides much better stopping power for energetic reaction products inside the ion guide. For argon, the minimum required length of the interaction region is about 33 mm due to the lower axial velocity ($\sim$330 m/s).

The complete SPIG system is illustrated in Fig.2.5. The rods have been aligned by plastic support rings that are shielded against charging up with conductive shield plates. RF signals are coupled to the SPIG rods via ring shaped copper contacts, directly connected to the fastening screws of the rods. A complete discussion about the SPIG rf and dc control system is given in Appendix A. In addition to the SPIG elements, the system contains two additional electrodes: the repeller and the end electrode. The repeller electrode can be used to prevent any positively charged ions entering the SPIG in the LIST mode as discussed earlier. However, when the LIST mode is not being used, the electrical polarity of the repeller electrode can be inverted for an ion transport mode. In this mode the SPIG replaces the traditional skimmer electrode, improving both the efficiency and the beam quality of non-laser experiments. The end electrode, which is directly attached to the mounting drum of the SPIG system, provides a low voltage ejection for ions before they enter the extractor chamber and are accelerated towards the mass separator. Moreover, it acts as a buffer for the differential vacuum system limiting the gas flow between the target and the extractor chambers.

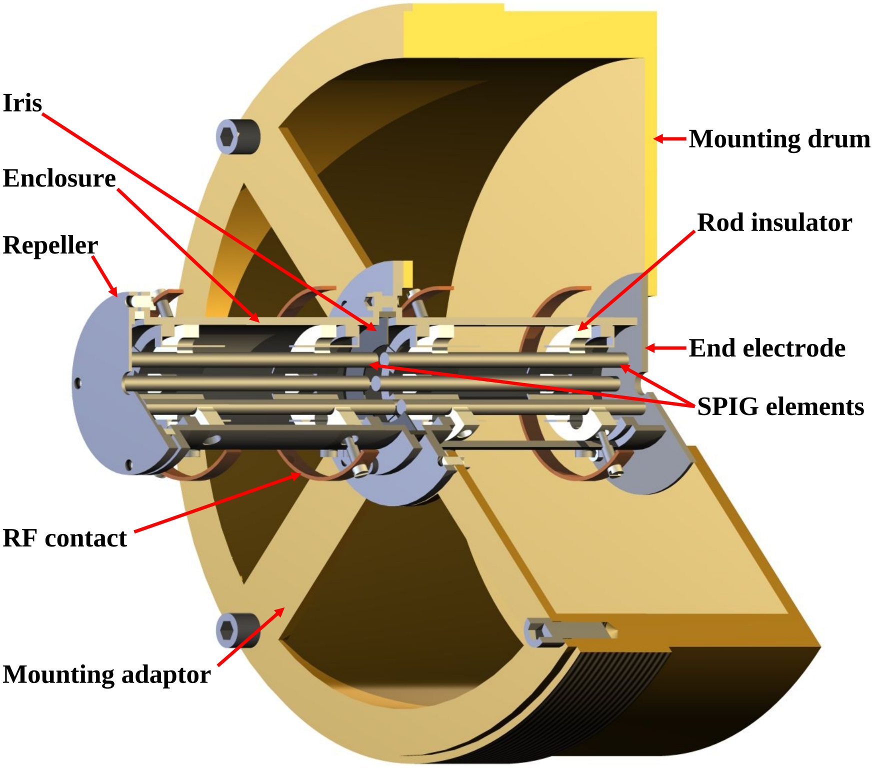

Figure 2.5.: A cut-off illustration of the IGISOL SPIG system. See text for more details.

2.4. SPIG simulations

2.4.1. Motivation for the simulations

It is generally known that the SPIG improves both the efficiency and the beam quality of IGISOL. It is also understood that the improved beam quality is mainly due to buffer gas cooling [32, 33] and low voltage acceleration introduced by SPIG. The buffer gas cooling effect is not, however, solely able to explain the experimentally observed improvement of the transmission efficiency as compared to the traditional skimmer system. Moreover, there is a clear discrepancy of beam qualities between two different SPIG systems tested at the IGISOL facility, even though their effects on the transmission efficiency are quite similar. With the SPIG system of this work, the MRP after the dipole magnet varies between 400 - 600, while values about twice higher than that were reached with the SPIG reported in [17]. In order to improve the understanding of the SPIG behavior under different environmental conditions and to better explain the functional differences between the skimmer and the SPIG, a set of ion optic simulations was made using the SIMION 3D ion trajectory simulation software [6, 34, 35].

Due to the presence of the buffer gas and a slow drifting velocity of ions, both the ion scattering from gas atoms and the charge repulsion effects need to be taken into account with sufficient accuracy. In principle, the cooling and scattering effects caused by a stationary background gas are relative easy to implement into the simulation code. There are many models available for the SIMION 3D software, including viscous drag models based on Stokes law [36], hard sphere collision models based on the kinetic gas theory [37, 38] and hybrids of the aforementioned models [39]. At IGISOL, the background gas pressure is not stationary but should be handled as a gas flow. In addition to the pressure needed for stationary models, a three dimensional gas velocity as well as the temperature distribution of the flowing gas need to be included. Although these parameters are supported by many of the models mentioned above, a complexity arises when a realistic gas flow as a function of the initial ion guide pressure and particle location needs to be described for the model. An additional complication is caused by the charge repulsion effects between simulated ions. The effective and proper simulation of this so-called space charge effect requires ions to be simulated in a grouped mode making the simulation process very slow and time consuming. The SIMION 3D software offers some built-in algorithms for the space charge estimation as discussed in [39], but for some reason, these algorithms were not fully functional with the selected buffer gas model.

The simulations shown in this work are based on those introduced in [40]. The space charge model has been completely revised and the accuracy of the buffer gas flow model has been improved. These simulations focus on the region between the ion guide and the extractor electrode. Because the ion paths through the rest of the IGISOL facility are not included, a direct comparison between the simulated and experimental data cannot be made. For example, the transportation efficiency of IGISOL is coupled to the quality of the ion beam after the skimmer or the SPIG. Especially in the skimmer case, the higher transport efficiency through it often leads to a reduced quality of the transported beam. At some point, the quality may become so poor that additional losses can occur during the ions path from the extractor to the measurement setup. Therefore, the settings of the skimmer or the SPIG, optimized via the simulations, do not necessarily represent the best values for the experimental situation, in which the detection of the ions does not usually happen until after the mass separator. On the other hand, the relative trends of the simulation and experimental results can be compared to each other. This comparison may give some kind of estimate of the validity of the simulation models.

2.4.2. Simulation geometry and ion source

The geometries used in the simulations of the devices are shown in Fig.2.6. Ion guides are illustrated as thin blocks located at the left in the figure. The distance between the ion guide and the skimmer electrode (bottom panel) is 10 mm, which is close to the typical experimental value. In the SPIG case (top panel), the repeller electrode is located at a distance of about 7 mm from the ion guide. Both simulated systems are followed by the extractor electrode located at the right side of the panels. The distance between the last component of the simulated device and the extractor electrode is slightly below 50 mm in the skimmer case and about 20 mm for that of the SPIG, both close to experimental values.

The simulated ions were created just in the front of the ion guide nozzle as shown in Fig.2.6. This “ion source” contained 500 singly charged ions randomly distributed inside a circle with a radius of 0.6 mm, which corresponds to the typical aperture of the exit nozzle of the fission ion guide. The axial kinetic energy of each ion was predefined in such a way that it matched the simulated velocity of the gas flow exiting from the ion guide ($\sim$1400 m/s for helium). The radial components of the kinetic energy of the ions were predefined as zero, because the gas flow is primarily in the optical axis direction at the ion source location. Two elements with clearly different masses, ^{20}Ne and ^{106}Cd, were selected as test ions representing different mass regions of IGISOL experiments.

The buffer gas model is very slow to simulate, especially when it is used together with the space charge model. Because of this, the simulations were not repeated for every simulated point to determine the uncertainty. Instead, the accuracy was

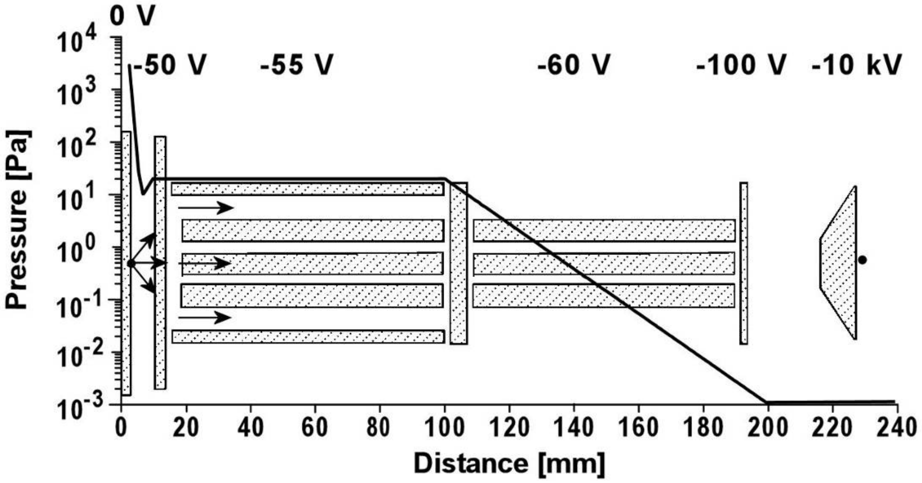

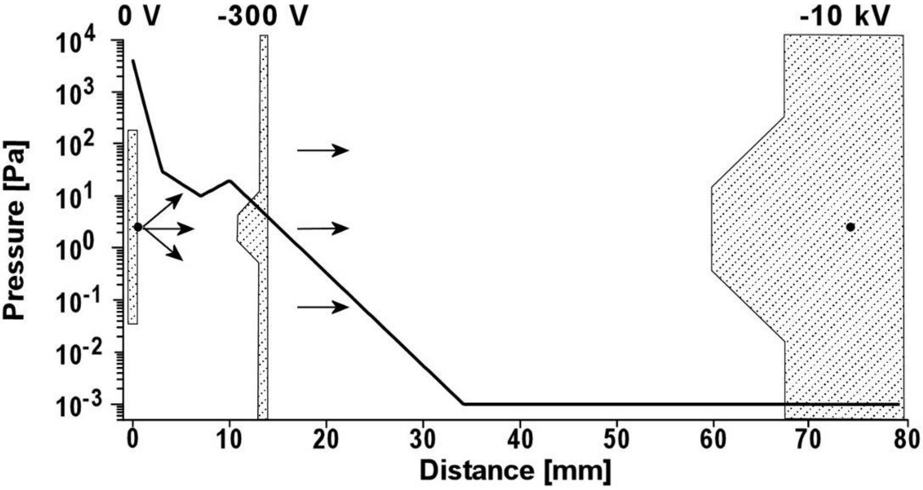

Figure 2.6.: The simulation models for both the SPIG (top) and the skimmer (bottom) devices. The solid lines indicate the simulated pressures at the optical axis of the simulated devices for 100 mbar ion guide pressure. The arrows illustrate the direction of the buffer gas velocity vectors. The ions are created in a circular source just in front of the ion guide on the left of both figures. The black dots located after the extractor nozzle illustrate the positions of the planes (vertically oriented with respect to the optical axis), in which the properties of the simulated ions are recorded. Typical potentials applied to the electrodes are also shown, although their values varied during the simulations. In the SPIG case, a frequency of 3 MHz was used in all simulations and the rf amplitude was 250 V unless otherwise stated.

tested by repeating the same low pressure simulation several times. In this test, the statistical deviation of the results was $\sim$5 %, while the absolute maximum difference was about 7 %.

2.4.3. Buffer gas model

A hard sphere collision model (hereafter called HSC model) for SIMION3D [41], developed by D. Manura, was selected to model ion - neutral atom interactions. The model provides a three dimensional treatment of every individual ion - gas atom collision. Colliding particles are treated as hard spheres and collisions are assumed to be elastic. A collision frequency between an ion and gas atom, expressed as a mean free path of the ion (MFP), is predicted by the kinetic theory of gases as a function of collision cross section, gas pressure and gas temperature. The gas atoms are assumed to be non-stationary and their velocities follow a Boltzmann velocity distribution for a given temperature. This allows modeling of both cooling and heating effects depending on the kinetic energy distribution of the colliding particles. In addition to thermal motion of the gas atoms, randomly generated collision impact parameters for each collision are weighted by predefined mean velocities (in three dimensions). As a result, collisions can be modeled also for gas flows. For simplification, the background gas is not assumed to be affected due to the collisions and no chemical effects are included.

Both the pressure and three dimensional velocity at the optical axis of the SPIG were evaluated via gas flow simulations by Dr. A. Popov using CosmoFloWorks [42] simulation software. The gas temperature, though it drastically changes in the ion guide nozzle region, was kept at a constant value of 293 K. Inside the SPIG the simulated temperature remained quite constant. The collision cross-section, as defined by the model, is an area of a circle having a diameter which is roughly a sum of the diameters of the colliding particles. In this work, the Van der Waals radius (VdW) of the atom was used to describe the particle radius [43]. The theoretical VdW radii of the test particles are 154 pm and 158 pm for ^{20}Ne and ^{106}Cd, respectively [44]. It is worth noting that the selected radii are valid for neutral atoms only, which was considered to be sufficient for the simulations of this work. A simulation time step is automatically calculated from the 'time steps per MFP' parameter. Here the default value of the model, 20, was used. This means that the mean free path of the ion is divided into 20 equal time steps. The time step is automatically updated at every simulation step if necessary. Sometimes, depending on the ions' velocity and mean free path, the time step may become so long that the rf field cannot be effectively simulated anymore. In such cases, the maximum time step was limited to a few tens of per mille of the rf cycle.

Gas flow simulations were performed for an ion guide pressure of 100 mbar for the pressure distributions shown as the solid lines in Fig.2.6. After the exit hole the pressure drops to ∼10 Pa until it slightly increases due to turbulent gas flow near the first elements of the simulated systems. The pressure smoothly decreases to its final value after the skimmer electrode, while inside the first SPIG element it remains constant. The pressure decreases again inside the second SPIG element due to the improved gas evacuation, finally reaching the base vacuum level of the IGISOL vacuum system. Modeling for other ion guide pressures was generated by a simple linear scaling. For the region between the ion guide and first elements of the simulated systems (the skimmer or the repeller) an isotropic symmetry of the pressure was assumed. In other words, the pressure remains constant at the given radius of the particle and it changes only as a function of the distance between the ion and the ion source location. After the first elements of the simulated systems the pressure was assumed to be a one-dimensional function of the optical axis distance without any radial dependence.

The gas velocity at the optical axis of the SPIG was reproduced with sufficient accuracy using a combination of three Gaussian shaped peaks. Moreover, it was also possible to find quite simple relations between the peak parameters so that the optical axis velocity of the gas particles could be easily estimated for any ion guide pressure. It should be noted that this method has nothing to do with the real physics behind the gas flow. It is only used as a tool that provides, in a realistic way, the gas atom velocity distribution for the simulation in a computationally effective manner. The gas velocities in the SPIG system provided by this model for several different ion guide pressures are shown in Fig.2.7. The general trend of the velocity curves as a function of the optical axis distances are quite similar for all pressures. The velocity remains almost the maximum until the repeller electrode whereby it starts to decrease. The local minimum of the velocity is reached inside the first SPIG element, where the gas pressure remains almost constant. An increased evacuation of the gas due to the open structure of the second SPIG temporarily increases the velocity of gas atoms between the SPIG elements. The velocity then rapidly drops in the second SPIG region.

The buffer gas velocity model for the skimmer behaves in a similar way as for the SPIG, now without the local maximum at 100 mm. However, the velocity of the gas is not such a critical parameter in the skimmer case as the ions axial movement is dominated by strong electric fields. Again for both cases, an isotropic symmetry was used in the ion guide region providing an “explosion”-like scenario for the gas flow. The symmetry point was selected behind the ion source position, inside the ion guide nozzle, in order to create a forward peaking effect of the gas flow. Therefore, the maximum angle of a gas particle ejected from the nozzle was set to ±60 degrees with respect to the optical axis. After the first element of the simulated system, radial vectors were ignored and the total velocity vector becomes one-dimensional along the optical axis of the simulated device. Gas velocity vectors are illustrated as the arrows in Fig.2.6.

2.4.4. Space charge model

A typical beam current from the ion guide is of order of a few μA mainly depending on the reaction and the ion guide type used in the experiment. Before $\sim$10 kV acceleration provided by the extractor electrode, the axial kinetic energy of the ions is only a few 100 eV at maximum. Therefore, the axial velocity of the ion beam is so low that a repulsive force caused by the ions themselves can not be ignored.

SIMION3D software offers some tools for the space charge effect estimation. Unfortunately, these tools seemed to be rather incompatible with the HSC model. It may be that these tools are not able to correctly simulate the ions, whose direction is continuously changing due to the collisions. Therefore, the space charge model was developed by using the user program interface provided by SIMION3D.

For simplification, only the radial component of the repulsion force was taken into account in the simulations. The effective calculation of axial repulsion requires an iterative simulation method, which cannot be realized in a reasonable timescale when using SIMION3D. It is obvious, however, that the axial velocities of the ions vary during a path through the simulated systems and hence the total charge of the ions is not uniformly distributed over the simulated region. This means that the repulsion also occurs in the axial direction, aspiring to equalize differences in the charge density. As discussed in [17] and [28], the effect of a static electric field is very limited in a high charge density region. In the ion guide with a charge density of about 10^9 ions/cm^3, the effective penetration depth of a static electric field is only a few tens of μm. If the average charge density inside the SPIG system is $\sim 6\cdot 10^6$ ions/cm^3 (calculated with an ion current of 100 nA, an ion time-of-flight of 100 μs and a SPIG volume of 11 cm^3), a penetration depth of about 0.5 mm for a static electric field can be calculated with the Debye length equation

$$D = \sqrt{\frac{\epsilon_0 kT}{ne^2}}, \tag{2.2}$$

where ϵ_0 is the vacuum permittivity, k is Boltzmanns constant, T is the temperature, n is the charge density and e is the elementary charge. This 0.5 mm not only describes the penetration length of a static field inside the SPIG, but it also reflects the interaction distance between two charged ions in such charge density conditions.

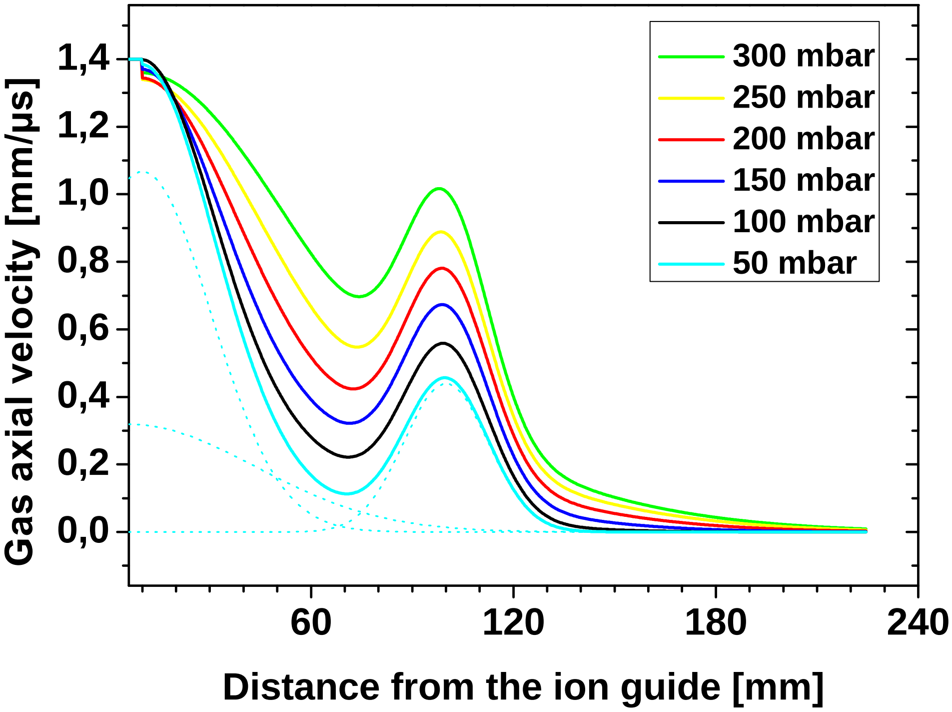

Figure 2.7.: Gas velocities in the SPIG as a function of the optical axis position for several ion guide pressures. The velocity profiles are superpositions of three Gaussian-shaped peaks. The profiles are functions of ion guide gas pressure only and they have been matched to the simulation results using the simulated profiles for 100, 200 and 300 mbar ion guide pressures. The dashed lines show the construction of the 50 mbar pressure model.

The ions are assumed to feel a homogeneous axial electric field generated by the surrounding charged particles. As the model contains only radial effects of the repulsion, an electric field generated by an infinitely long, uniformly filled cylinder of charge can be used as a basis already introduced in [40]. The general form of such an electric field is

$$E_{SC} = \frac{\lambda r}{2\pi\epsilon_0 r_0^2} \quad r < r_0 \tag{2.3}$$

$$E_{SC} = \frac{\lambda}{2\pi\epsilon_0 r} \quad r \geq r_0 \tag{2.4}$$

where λ is a "charge per unit length" factor, r is the ion distance from the center of the multipole and r_0 is the radius of the charge filled cylinder. The local changes in charge density can be introduced by varying λ as a function of the ions average propagation velocity. Moreover, if the charge density is introduced as beam current ejected from the ion guide, the equation for the repulsive electric field becomes

$$E_{SC}(r, r_0, v_z, I_B) = \frac{I_B}{2\pi\epsilon_0 v_z}\frac{r}{r_0^2}, \quad r < r_0 \tag{2.5}$$

$$E_{SC}(r, v_z, I_B) = \frac{I_B}{2\pi\epsilon_0 v_z}\frac{1}{r}, \quad r \geq r_0 \tag{2.6}$$

where v_z and r are now the Root Mean Squared (RMS) velocity and radius formed by a simulated ion group, respectively, and I_B is a dynamical beam current that is scaled according to the number of the ions which are still active in the simulation. Because this space charge model requires some "ion group" related parameters, ions must be simulated simultaneously in a grouped mode. The first ion of the group is used as a trigger for a new simulation round. Each ion group related parameter (r_0, v_z and I_B) is recalculated during the simulation of this ion. The dynamic calculation of the parameters becomes feasible only if all ions move together. This is not, however, a trivial task in SIMION3D, since it utilizes a time-based simulation method. This means that the TOF of simultaneously simulated ions remains equal during the simulation resulting in a dispersion effect of all ions. In order to advance the ions together, the simulation process of the fastest ions is halted until the slowest ions catch up. A simplified flow chart of the space charge simulation process is shown in Fig.2.8, in which the maximum dispersion of the axial positions is limited to 0.2 mm. This was considered to be sufficient for a space charge estimation within the limits of the simulation accuracy.

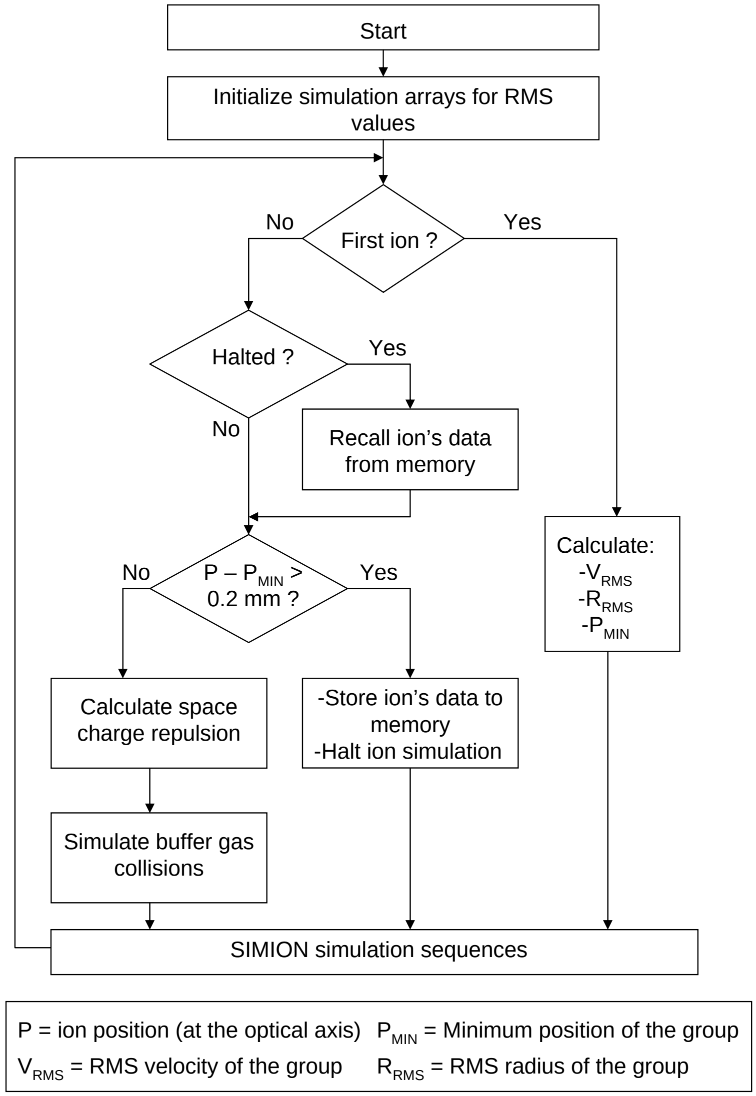

Figure 2.8.: A simplified flow chart presentation of the space charge simulation process.

2.4.5. Simulation results

Kinetic energy of the ions in the SPIG system

The buffer gas cooling effect plays a very important role in the SPIG system, especially when high gas pressures are used. It is thus of interest to simulate the cooling capability of the SPIG system for both the axial and the radial motions of ions. One way to do this is to observe possible changes in the kinetic energy distributions of the ions during the simulation. A simulated mean axial kinetic energy of 10 $A = 106$ ions as a function of distance from the ion guide for three ion guide pressures is shown in Fig.2.9.

At the beginning of the simulation the axial kinetic energy of the ions rapidly increases due to the acceleration provided by the repeller electrode. The full acceleration energy of the repeller is 100 eV although it is never reached due to the high pressure in the acceleration zone. After the ions pass the repeller electrode, they feel only a small axial electric field caused by a 5 V voltage difference between the repeller and the first SPIG element. This electric field cannot penetrate very deep inside the SPIG and therefore the cooling of the axial motion is almost immediately initiated.

For 100 mbar ion guide pressure, the minimum axial velocity of the buffer gas inside the first SPIG element is ~250 m/s (see Fig.2.7), which roughly corresponds to a kinetic energy of 0.03 eV for the simulated ions. The minimum simulated axial energy of the ions is about twice higher, indicating that the cooling effect is not yet strong enough to completely cool the ions before the next 5 V acceleration that takes place between the SPIG elements. The cooling efficiency, however, improves as the gas pressure is increased. The kinetic energy of the ions is then increased by the axial acceleration between the SPIG elements before the cooling effect of the second SPIG element. The cooling efficiency of the second SPIG element is not as strong as that of the first SPIG due to the decreased gas pressure. This can be observed for example in the 100 mbar curve of Fig.2.9, where the cooling effect is not sufficient to overcome the electrical acceleration provided by the second SPIG. The final rapid increment of the kinetic energy is provided by the extractor electrode as ions are accelerated close to 10 keV energy.

The radial kinetic energies recorded during the same simulations are shown in Fig.2.10. Although the initial radial kinetic energy of the ions was predefined to be zero, it immediately increases to a value close to the mean radial energy of the gas particles due to the numerous collisions in the ion guide nozzle region. After a small focus effect caused by the repeller electrode, the energy rapidly increases as the ions enter the rf section of the first SPIG element. The injection radius of the

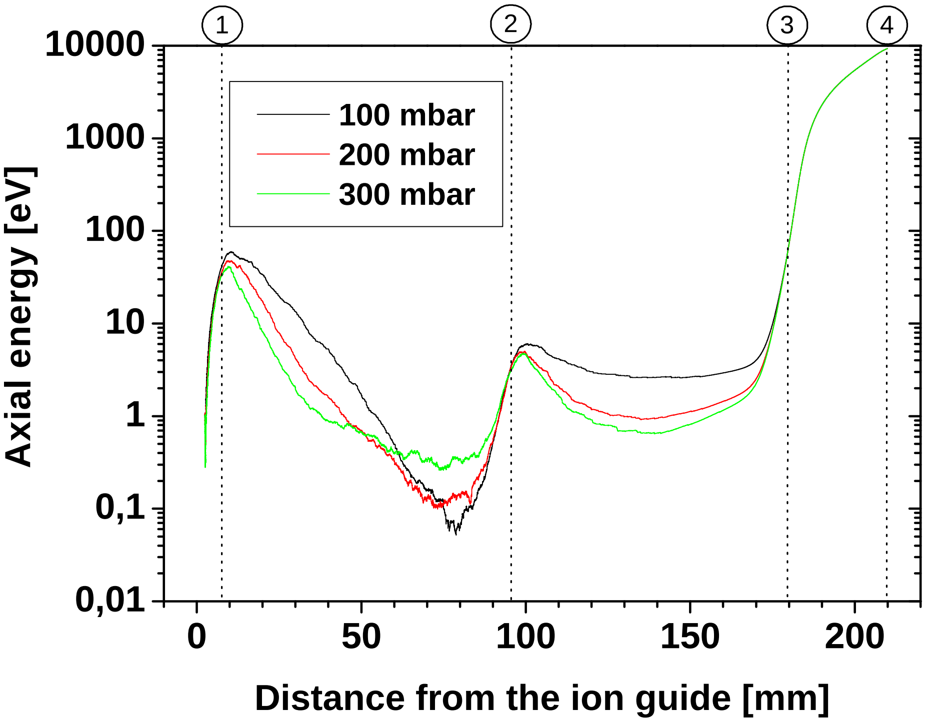

Figure 2.9.: Simulated axial kinetic energies as a function of the optical axis position with respect to the ion guide for several ion guide pressures. The solid lines are averages of ten A=106 ions randomly created within the original ion source area. The dashed lines indicate the positions of the electrodes (1 = repeller (-100 V), 2 = iris (-105 V), 3 = end electrode (-200 V) and 4 = extractor (-10 kV). All voltages are given with respect to the ion guide potential).

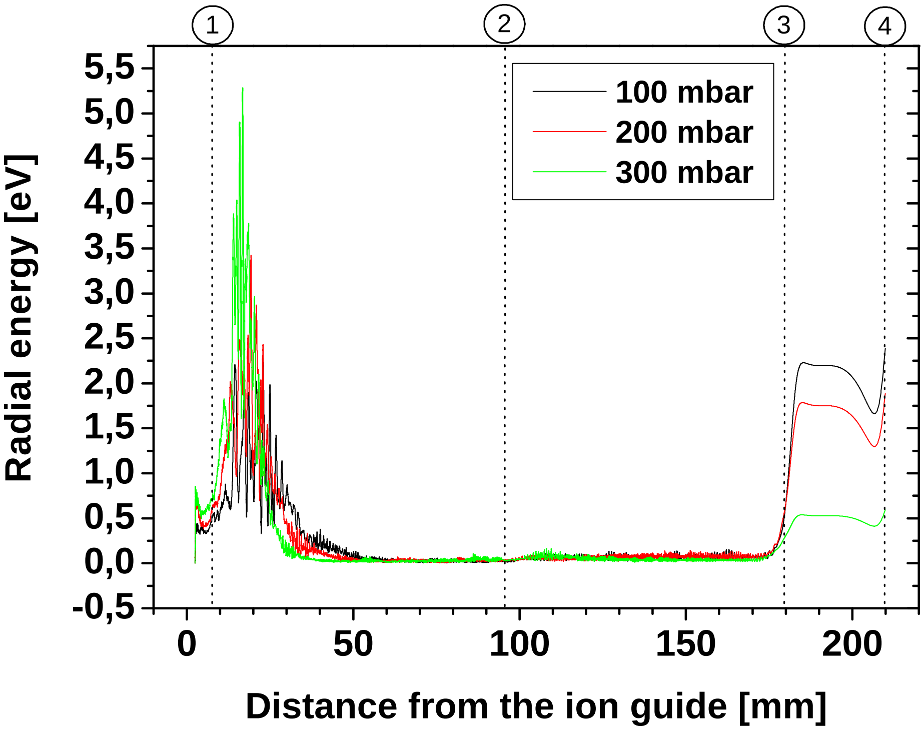

Figure 2.10.: Simulated radial kinetic energies as a function of the optical axis position with respect to the ion guide for several ion guide pressures. The graphs are averages of ten A=106 ions randomly created within the original ion source area. The dashed lines indicate the positions of the electrodes, whose potentials are given in the caption of Fig.2.9.

ion beam increases as a function of the gas pressure and therefore the ions influenced by the higher pressure also feel the higher rf field as they enter the SPIG. This in turn leads to a more energetic oscillation of those ions at the beginning of the SPIG element. Soon after this temporary heating of the ions, their radial kinetic energy is decreased by the buffer gas cooling effect. In a similar manner as in the axial case, the cooling occurs within a fast time scale and, once again, slightly faster at higher gas pressure. Once the ions are cooled near the center of the SPIG system, their interaction with the rf field reduces and their radial kinetic energies remain low through the rest of the SPIG. The ions are finally ejected from the rf field by the end electrode. According to the simulation results, the most significant changes in the radial energies are produced during this acceleration. The cooling effect in the second SPIG is stronger for the higher gas pressure, which results in a smaller beam size. After ejection, a small focusing effect occurs as the ions pass through the extractor electrode aperture. This effect is then followed by a defocussing effect. This may be due to the unrealistic modeling of the electric field after the extractor since the actual ground electrode was not included in the simulations.

It is worth noting that the space charge model was not applied in these simulations. The results thus reflect the effect of buffer gas cooling as a function of ion guide pressure. In any realistic situation, the space charge effect due to a high charge density greatly hinders the radial cooling of the ions. The ions are continuously pushed towards the higher rf field by the space charge and therefore the energy spread of the ion beam increases. This reduces the pressure dependency of the kinetic energy distribution inside the rf field and leads to a poorer quality ion beam.

Beam emittance with space charge model

One of the most interesting features of the rf multipoles is their ability to improve the quality of the ion beam when used with high background pressures. In this context, the beam quality is related to the mass resolving power (MRP $= M/\Delta M$) of the beam after the dipole magnet. The mass resolution of the separated beam depends on the divergence of both axial and radial kinetic energies of the ions in the beam: a coherent, mono-energetic ion beam can be separated with the highest MRP, which depends only on the properties of the dipole magnet.

After the aperture of the extractor electrode, the velocities and the positions of the simulated ions were recorded. The radial velocities of the ions were converted into angular velocities with respect to their axial velocities. These angular velocities were plotted as a function of the corresponding radial positions, resulting in an elliptical data group called the phase space ellipse as illustrated in Fig.2.11. The area of the ellipse, $\pi(A \times B)$, is generally called the geometrical emittance, which is proportional

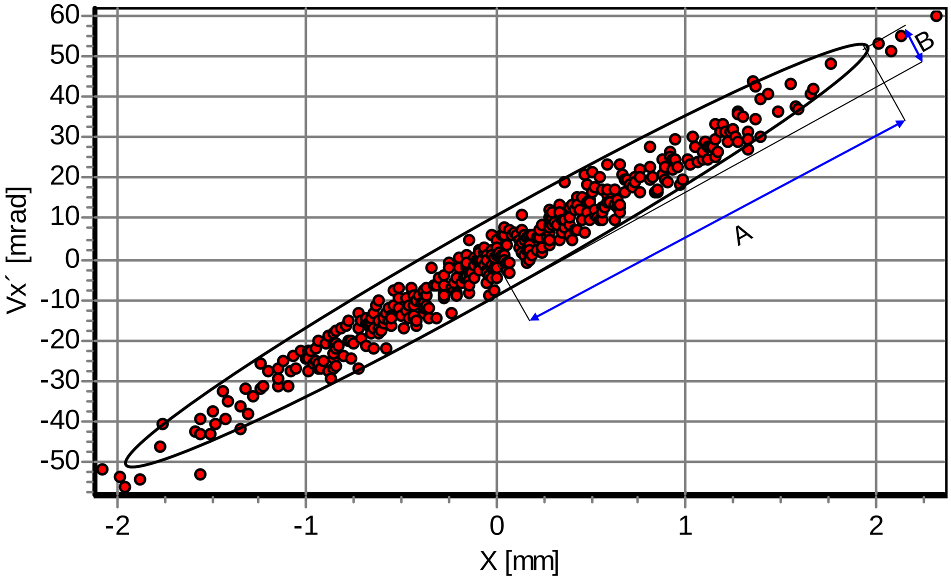

Figure 2.11.: An example of the simulated phase space ellipse for a beam of $A = 20$ ions. The emittance of the beam (in πmmmrad units) is the area of the ellipse, $\pi(A \times B)$.

to the size and divergence of the beam in a selected direction. A smaller emittance value indicates a better beam quality and provides a higher MRP for the beam after the dipole magnet. More informative discussion about the emittance can be found in [45], for example.

In this work, the RMS area of the geometrical emittance ellipse was determined from simulation data in a numerical way. Results as a function of the ion guide pressure for both devices are shown in [40], without the space charge estimation. The simulations indicate that the emittance after the skimmer electrode increases as a function of the ion guide pressure. The SPIG system in turn benefits from the buffer gas cooling effect and therefore the beam quality drastically improves at higher pressures. A comparison of simulated emittances between the skimmer and SPIG as a function of the ion guide beam current for 100 mbar ion guide pressure is shown in Fig.2.12.

In the skimmer case, relatively high electric fields combined with numerous ion - gas atom collisions effectively increases both the radial and axial kinetic energy spread of the beam. At high gas pressures the beam quality becomes so worse that

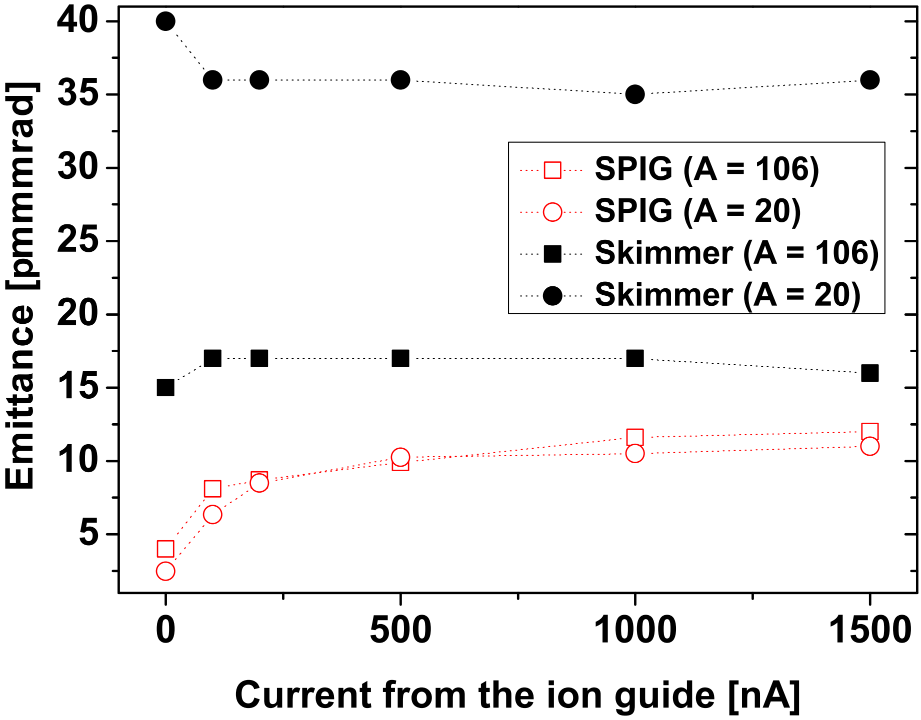

Figure 2.12.: The simulated emittances as a function of ion guide current for masses $A = 106$ and $A = 20$ and for 100 mbar ion guide pressure. The beam emittance after the skimmer is not very sensitive to the space charge but remains almost constant. The SPIG in turn suffers badly from space charge effects.

it is mainly determined by the geometrical acceptance of the skimmer. Therefore the beam emittance after the skimmer system is not significantly influenced by the space charge effect in such pressure conditions.

Unlike the skimmer, the SPIG suffers badly from the space charge effect. Due to the low drifting velocity of the ions, the charge density can increase greatly particularly inside the first SPIG element. Therefore, even a small amount of charge inside the SPIG is sufficient to spread the ion beam such that the flat region described by the effective potential V_r^* (see Eq.2.1) is filled. As a result, the emittance of the beam increases drastically. On the other hand, the spread of the ion beam outside the flat effective potential bottom is restricted by the steep slopes (see Fig.2.3) leading to a rapid saturation of the emittance.

As can be observed from Fig.2.12, the beam quality after the SPIG is clearly better than that of the skimmer if the space charge effect is not applied (beam current equals to zero). However, if the beam current is increased over 100 nA, the emittance difference reduces by a factor of 3 - 4 for both simulated masses. Experimentally observed MRP ratios between the devices (SPIG/skimmer) are about 1.5 at $A = 100$ and ~2.5 at $A = 40$.

The absolute values of the simulated emittances do not correspond to the actual experimental values, as the ground electrode was not included in the simulations. Therefore, the total acceleration potential used was 10 kV, which is only 33 % of the experimental acceleration. However, the radial velocities of the ions are much lower compared to their axial velocities, resulting in only small angles that are used in the emittance calculation. For such small angles, the emittance is almost linearly proportional to the axial velocity of the ions and, therefore, a more realistic emittance can be estimated from the simulation results by dividing by a factor of 3. However, the trends of the simulations show very good agreement with the experimental observations.

Transmission efficiency with space charge

In the original efficiency simulations performed without the space charge effect in [40] it was found that the skimmer efficiency decreases as a function of the background pressure because of the increased scattering of the ions primarily in the skimmer - ion guide zone. In the SPIG case, the transmission efficiency for both simulated masses remains high due to the buffer gas cooling effect and good geometrical acceptance of the repeller electrode. In reality, both devices suffer from the space charge effect and it is important to understand when the functionality of the devices is affected. The simulated transmission efficiencies and transmitted beam currents for both systems are shown in Fig.2.13. During the simulations, the ion guide pressure was fixed at

100 mbar in order to reduce the required simulation time.

In the skimmer case, the losses due to the space charge effect occur mainly in the skimmer - ion guide zone. The effect between the skimmer and the extractor is insignificant due to the high axial velocity of the ions in this zone. Skimmer voltages of -500 V and -200 V with respect to the ion guide were used for A = 106 and A = 20 ions, respectively. The voltages were selected corresponding to experimentally used values, even though they do not provide the maximum transmission efficiency through the skimmer system in simulations. In particular for light ions, a much higher efficiency can be reached by using higher skimmer voltages. However, a higher skimmer voltage reduces the beam quality. The simulated skimmer efficiencies for both masses were reduced due to scattering from the buffer gas prior to applying space charge.

The trends of efficiencies for both masses behave in very similar way, decreasing gradually as the charge repulsion spreads the beam in the skimmer - ion guide zone. The maximum charge density at the skimmer aperture is reached at about 500 nA beam current, leading to the saturation of the output current of the skimmer electrode as can be observed from the bottom panel of the figure. The maximum beam currents transmitted through the skimmer are $\sim$200 nA and $\sim$100 nA for the beams of $A = 106$ and $A = 20$ ions, respectively.

In the case of SPIG, the rf amplitude was set to 250 V_{0-p} for $A = 106$ ions. Due to the ion - gas atom scattering in the repeller - ion guide region, the radii of light ion beams are larger compared to those of the heavier beams when they enter the SPIG. Therefore, in order to avoid the injection losses, the rf amplitude was reduced to 150 V_{0-p} for the simulations of $A = 20$ ions. As shown in the top panel of Fig.2.13, the efficiency of the heavier ions remains high until a steady decrease after $\sim$200 nA beam current. Around 1 μA ion guide current, the SPIG seems to become full of charge. Since the acceptance of the repeller electrode still remains high, the losses occur mainly inside the SPIG, resulting in a rapid decrease of the efficiency and the saturation of the transmitted current. Due to a low acceleration voltage applied to the repeller electrode, some losses are already introduced at low beam currents for light ions. The current inside the SPIG increases now slower with respect to the beam current from the ion guide. Therefore the situation in which the SPIG becomes completely full of charge, is never reached with the simulated currents and the efficiency decrease is smoother as compared to the heavier ions. According to the simulations, the maximum beam current transmitted through the SPIG system is slightly below 800 nA for the heavier masses and slightly over 800 nA for the lighter masses.

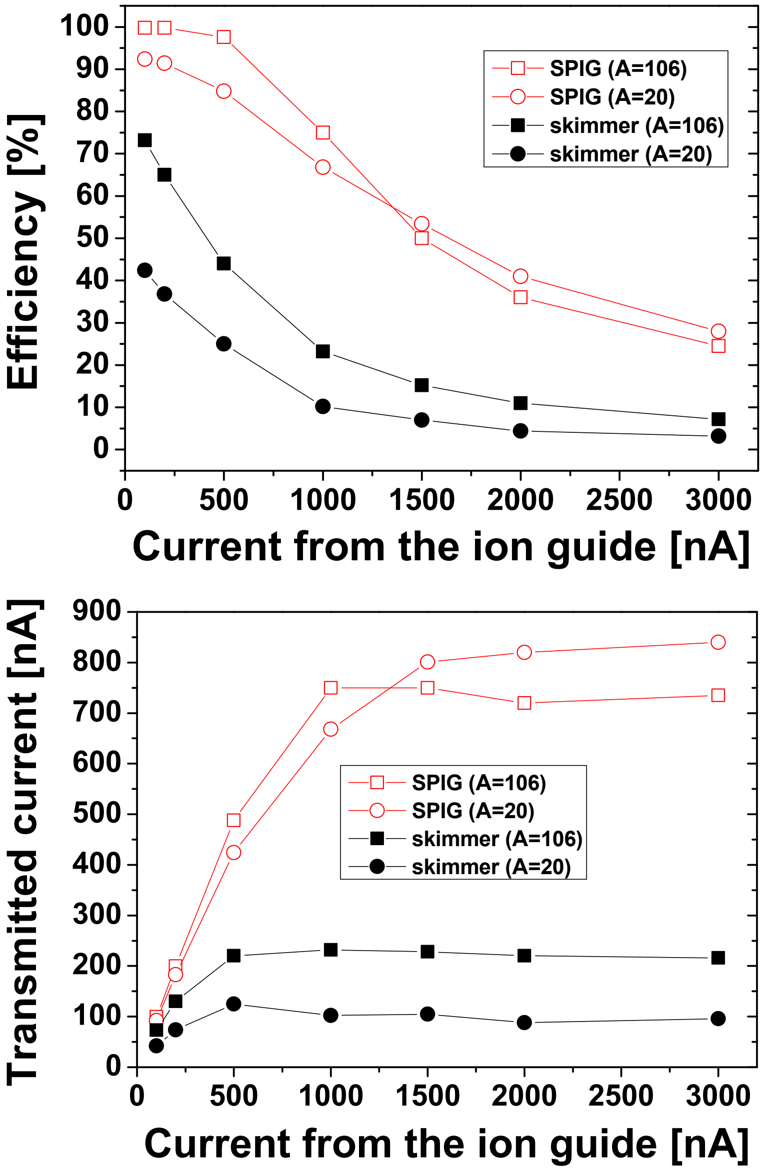

Figure 2.13.: The simulated transmission efficiencies (top panel) and transmitted currents (bottom panel) of $A = 20$ and $A = 106$ ions as a function of the ion guide current. The ion guide pressure was fixed to 100 mbar. RF amplitudes used in the SPIG simulations were 150 V_{0-p} and 250 V_{0-p} for $A = 20$ and $A = 106$, respectively. The skimmer voltage was -200 V for $A = 20$ ions and -500 V for $A = 106$ ions.

Time of flight

In the skimmer system, the ion time-of-flight (TOF) is dominated by strong electric fields, resulting in a very short, of order a few μs, transportation time. This time is negligible compared with the ion evacuation time from the ion guide, which is typically 0.1 - 100 ms depending on the ion guide type.

The situation is different for the SPIG system. As shown in Fig.2.9, the weak axial electric field inside the first SPIG element is not able to overcome the axial cooling effect provided by the buffer gas especially at higher pressures. With typical buffer gas pressures, the ions axial velocity decreases close to the mean axial velocity of the buffer gas, which varies between 100 - 700 m/s (see Fig.2.7) depending on the pressure of the ion guide. This increases the TOF of the ions through the SPIG system to several hundred microseconds. This time scale may be long enough for some chemical reactions to occur especially for very reactive elements such as yttrium in a high impurity environment [46].

The simulated TOF values for the ions of masses $A = 106$ and $A = 20$ as a function of the ion guide pressure are shown in Fig.2.14. TOF values at low pressures are mostly defined by the electrical acceleration. As the pressure increases, the axial cooling effect becomes stronger, increasing the TOF of the ions. The maximum TOF values ($\sim$ 200 μs for $A = 20$ and $\sim$ 130 μs for $A = 106$) are reached between 100 and 200 mbar ion guide pressures. If the pressure increases further, the TOF of ions saturates or starts to decrease due to the faster axial velocity of the gas. According to the experiences from earlier simulations, the radial space charge has no significant effect on the TOF. Instead, an axial space charge effect might play a large role, since it tends to balance the differences in charge density inside the SPIG. It was not, however, included in the simulation model and therefore the TOF simulations were carried out without the space charge model.

2.5. Experimental results

In the summer of 2005 the SPIG was installed in the IGISOL facility for the first time and tested in both off-line and on-line conditions. In this section, experimental results for different types of reactions and ion guides are discussed and the results with the SPIG system are compared to those of the skimmer whenever possible. More detailed information about the ion guides and associated reaction kinematics related to these tests can be found in [17, 19].

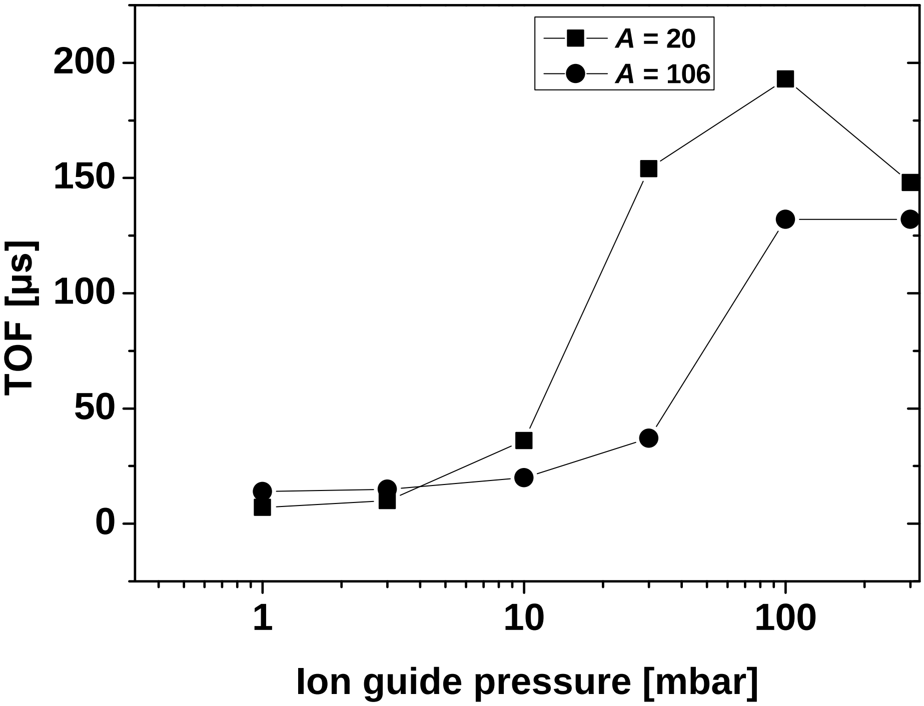

Figure 2.14.: Simulated TOF values for the ions of masses $A = 106$ and $A = 20$ as a function of the ion guide pressure for the SPIG system.

2.5.1. ^{223}Ra α-recoils

The first test of the SPIG system was an off-line experiment with ^{219}Rn^{+} ions. These ions were produced via the spontaneous α-decay of a ^{223}Ra source that was collected onto the tip of an aluminum stick as described in [17]. The source was mounted inside a discharge-type ion guide where the α-recoil products, including ^{219}Rn^{+} ions, were captured and ejected within the helium gas flow. Those ions were guided through the mass separator and implanted into a foil located in a front of a silicon detector with a 30 % detection efficiency. The rate of mass separated ^{219}Rn^{+} ions was compared to the total α-recoil yield emanating from the source. The short half-life of 3.96 s of ^{219}Rn makes it suitable for this test.

This test was repeated at various ion guide pressures and was compared to the skimmer system. The skimmer electrode was operated approximately at 120 V below the ion guide potential and was positioned at a distance of 10 mm from the guide. The rf amplitude applied to the SPIG rods was 180 V_{0-p} with -40 V dc on SPIG1 and -60 V dc on SPIG2 with respect to the ion guide. The gap between the repeller and the ion guide was about 3 mm. The result of the test is shown in Fig.2.15.

The overall behavior between the devices is quite similar. At low pressures, both devices produce almost equal yields. The recoil range of ^{219}Rn ions in this pressure region is about 10 mm, which is close to the volume dimension of the discharge ion guide. Therefore, some ions may be lost due to collisions with the ion guide walls. As the pressure increases the stopping efficiency of the ion guide improves. The improvement in the SPIG is slightly better although no striking difference compared to the skimmer can be observed. At higher pressures, the yields of both systems begin to saturate, the SPIG slightly earlier than the skimmer. At the highest pressure, the efficiency of the SPIG decreases while the skimmer efficiency saturates at the 10 % level.

The yield reduction using the SPIG is most likely related to the rf amplitude used. At the time of the tests the maximum amplitude was about half of the 300 V of the current SPIG system. It is worth noticing that the charge density produced by the α-recoil source is very low. The transport efficiency of the skimmer increases towards higher masses as can be deduced from the simulations (Fig.2.13). Therefore, the experimental conditions are more favorable for the skimmer, and thus the SPIG shows no improvement compared to the skimmer unlike the on-line reactions discussed below.

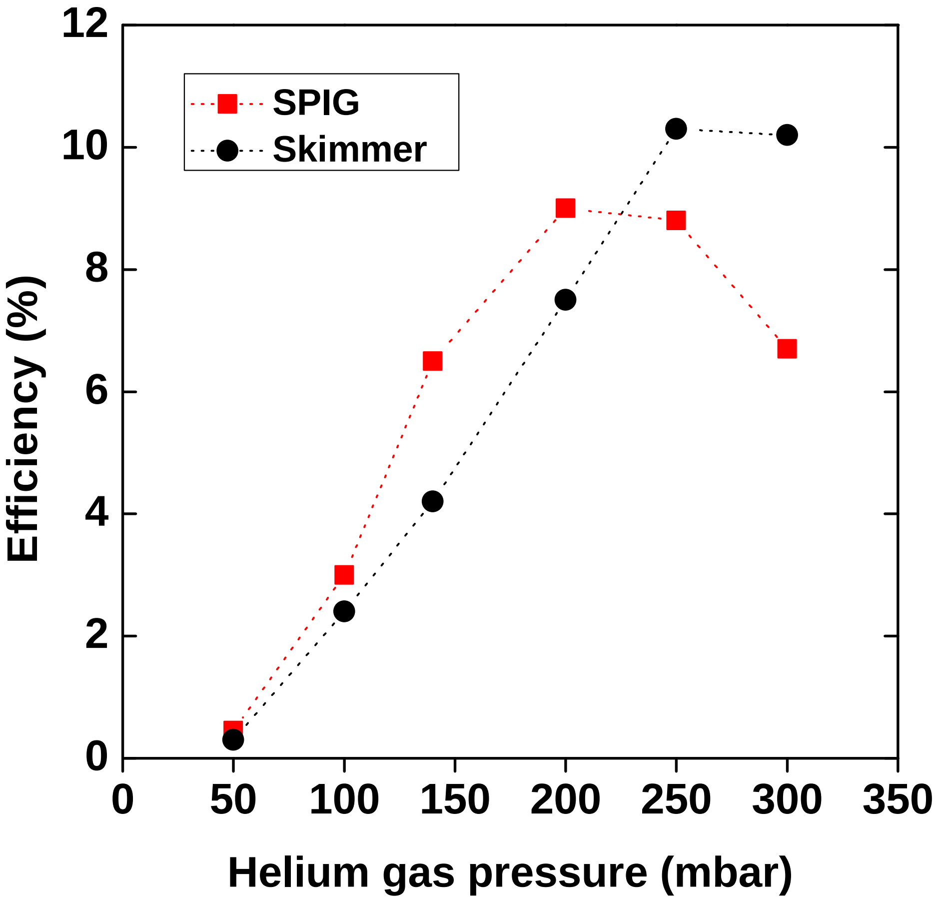

Figure 2.15.: The measured total efficiencies of $^{219}\mathrm{Rn}^{+}$ as a function of ion guide pressure using both the skimmer and the SPIG systems. See text for more information.

2.5.2. Light-ion fusion-evaporation reactions

There are two different measurements where both the SPIG and the skimmer has been used with the same reaction. The first of these two was ^{40}Sc ($T_{1/2}$ = 183 ms) produced from a ^{40}Ca target via the (p,n) reaction. The energy of the proton beam was 35 MeV and the thickness of the ^{40}Ca target was a few mg/cm^2. The effective target thickness was, however, determined by the reaction kinematics. Positrons from the β^+-decay of ^{40}Sc$^+$ were detected by a silicon detector with 30 % efficiency. The detector was located behind a set of slits in the switchyard chamber (see Fig.3.2), just after the focal plane of the mass separator. The observed yields as a function of the primary beam intensity for both devices are shown in Fig.2.16. Both measurements were performed with a helium gas pressure of 150 mbar. The linear fits to the data show that the yield of ^{40}Sc for the SPIG is a factor of ~8 higher than that of the skimmer system. The MRP for both devices was measured by using an A = 40 (argon) beam and a Faraday cup with a 1 mm slit located in the switchyard. The results show ~2.5 times difference between the devices.

In the beginning of 2009, the same ion guide equipped with a similar target was utilized in ^{40}Ca(^{3}He,n)^{42}Ti reactions for collinear laser spectroscopy. Earlier observations of high intensity impurity beams from the SPIG in the A = 40 - 50 mass region led to the choice of using the skimmer electrode. A yield of ~40 ions/s of ^{42}Ti with 1 μA primary beam was observed using the silicon detector setup described above. This yield was, however, too low for this particular experiment and thus the skimmer was replaced by the SPIG system. Under similar conditions, ~290 ions/s were detected with the same primary beam intensity. The improvement of a factor of 7 with the SPIG verifies that the performance is much better compared to the skimmer at low masses, in the presence of primary beam generated plasma.

2.5.3. Proton-induced fission reaction

The proton-induced fission of ^{nat}U, producing a large number of different fragments on the neutron rich side of the valley of stability, is the most widely used reaction at IGISOL. A mapping of isotopic fission yield distributions described later in this work was one of the first on-line experiments performed with the SPIG system. In this experiment, a 25 MeV proton beam provided a high, ~18 mb (deduced from the independent fission cross-section of ^{112}Pd given in [47] and known nuclear charge distribution of A = 112), cross section for the production of ^{112}Rh. As a similar measurement had already been performed with the skimmer system, a reasonable comparison between the devices is possible.

Nuclear fission produces many radioactive species with the same mass number

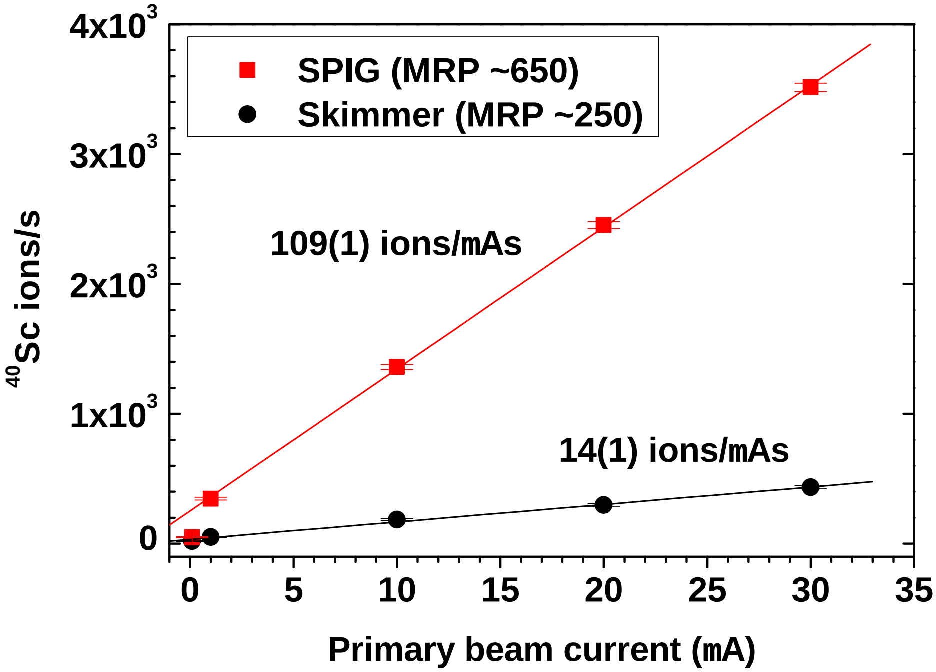

Figure 2.16.: ^{40}Sc yields from a light-ion fusion-evaporation reaction for both the SPIG and the skimmer as a function of the primary beam intensity. The solid lines are linear fits of the data points illustrating the yield per μA of primary beam current. Statistical errors, combined with the detector efficiency of 30 %, are also given.

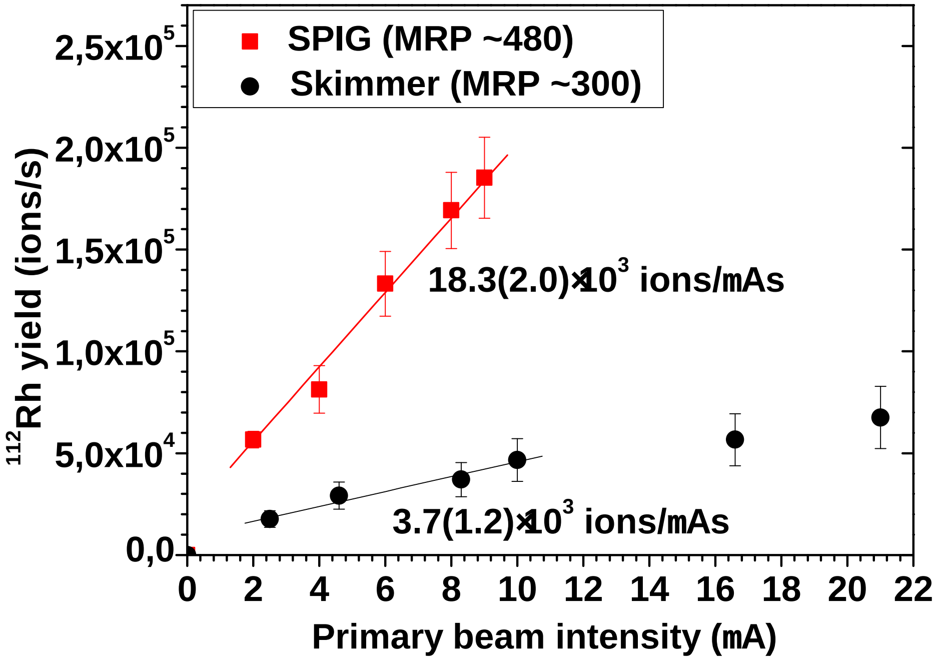

Figure 2.17.: ^{112}Rh yields from 30 MeV proton-induced fission of ^{238}U as a function of primary beam intensity for the SPIG and the skimmer. The solid lines represent the linear fits of the data giving the yield increase per 1 μA primary beam current. The statistical errors combined with the Ge detector efficiency are also shown.

and thus the yield of ^{112}Rh was determined using γ-spectroscopy. The nucleus ^{112}Rh contains two states of which both are produced in fission: a ground state with $T_{1/2}$ = 3.5 s and an isomeric state with $T_{1/2}$ = 6.7 s [48]. The ground state of ^{112}Rh is additionally fed by its mother nuclide, ^{112}Ru ($T_{1/2}$ = 1.75 s), which is also produced in fission. Both states of ^{112}Rh subsequently β-decay into excited states of ^{112}Pd which de-excite by emitting γ-rays.

The yields as a function of the primary beam current extracted from spectra of both the SPIG and the skimmer experiments are shown in Fig.2.17. The ion guide pressure in these experiments was fixed at 200 mbar. The data for the SPIG is limited to 9 μA primary beam current due to radiation safety limits of the IGISOL working area. The solid lines are linear fits to the data providing estimations for the yield per μA of primary beam current. The two last points of the skimmer data were excluded from the fit since the increase of yield is clearly non linear. The overall efficiency of the SPIG was a factor of ~5 higher than that of the skimmer in this experiment and a factor of 1.6 improvement of the MRP for the SPIG system was observed after the dipole magnet. These values agree rather well with the simulation results of $A = 106$ (efficiency factor ~3.5 and MRP factor ~ 1.5) discussed in section 2.4.5.

2.5.4. Heavy-ion induced fusion-evaporation reaction

In December 2005, the heavy-ion ion guide was installed at the IGISOL for the first time together with the SPIG system. The goal of the experiment was to measure the masses of neutron deficient nuclei close to the $N = Z$ line using the JYFLTRAP facility [49]. In addition, tests with the laser ion source using both the skimmer and the SPIG systems were performed [50]. The performance of the two devices can be compared using the yields of yttrium from a ^{nat}Ni(^{32}S^{7+},5p3n)^{82}Y reaction, which was also previously studied in decay spectroscopy measurements reported in [51]. In order to keep the present test comparable with the previous measurement, the same primary beam energy of 165 MeV was chosen. Also the thickness of the natural nickel target, 3.7 mg/cm^2, was consistent with that used previously. The mass separated $A = 82$ ion beam was implanted in a tape station located at the central beam line of IGISOL. The yield of ^{82}Y was monitored with a $\beta - \gamma$-detection setup, which contained a plastic 3π-scintillator and a germanium detector.

^{82}Y β-decays into excited states of ^{82}Sr with a half life of ~8.3 s. Although this decay is not very well known, the proposed decay scheme can be found in [51]. The γ-transition of 575 keV was used to extract a yield of 1.0±0.2 ions·s^{-1}pnA^{-1} for the skimmer with a primary beam intensity of 28.6 pnA and with an ion guide pressure of 200 mbar. Fig.2.18 shows the effect of changing to the SPIG system. The yields are practically the same. The deduced yield with the SPIG was 1.0±0.3 ions·s^{-1}pnA^{-1}, the larger uncertainty being due to the lower statistics. The production efficiency for ^{82}Y in this particular test was about a factor of 2 lower than observed in [51]. For a similar ion guide, only a slight improvement of the yields was observed with the previous SPIG system in [17].

In the HIGISOL method, the primary beam is stopped by a small beam dump located before the ion guide and hence the charge density inside the gas cell is smaller compared to the light-ion guide, for example. It could be thus reasonable to expect that the amount of charge ejected from the ion guide is also smaller, making the skimmer better suited for HIGISOL reactions.

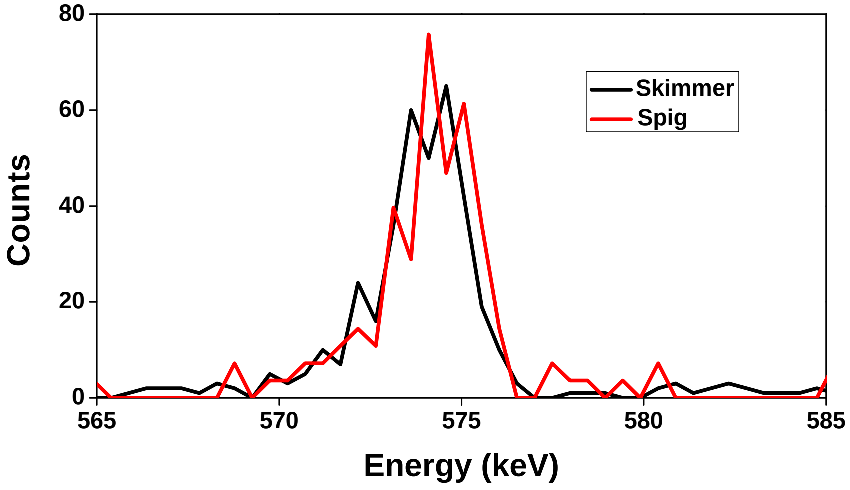

Figure 2.18.: β-gated 573 keV γ peaks belonging to the decay of ^{82}Y measured using both the SPIG and the skimmer. The data collection time of the SPIG was 19 min and it has been normalized to corresponding with the 70 min measurement period of the skimmer measurement.

2.5.5. Time of flight measurements

Molecular formation of the most reactive species may have significant effects on the produced yields. One such reactive element is yttrium which has been intensively used in connection with tests of the laser ion source. A deeper investigation of the molecular formation of yttrium isotopes can be found in [46]. In that work the formation time scale of yttrium oxide was found to be very short especially when the baseline pressure is at the level of $5{\cdot}10^{-3}$ - $1 \cdot 10^{-2}$ mbar, a typical pressure for the IGISOL target chamber under the on-line conditions. Motivated by this, the ions flight time through the SPIGsystem was experimentally measured.

An 18 MeV proton beam was directed on a natural nickel target installed in the light ion guide in order to recoil target material into the gas, forming a quasi on-line source of stable ions. For the measurement, the SPIG was equipped with two fast dc switches, one coupled to the repeller electrode and the other to the end electrode. DC levels were selected in such a way that one level corresponded to the normal potential of the electrode and a second was higher, preventing ions from passing through the electrodes. The ions were detected by a MCP detector located downstream from the focal plane of the separator. Only one electrode was pulsed at a time, while the other was set to the normal operational mode, thus enabling the time distribution to be studied.

Fig.2.19 shows the measured TOF profile of the nickel ions with 100 mbar ion guide pressure. The black solid line shows the time profile when the end electrode was pulsed. The "active" time is indicated by the vertical black lines. During that time period a normal potential was applied to the end electrode providing an optimized transmission through the SPIG system. The electrode was set to the active state 400 μs after the main trigger of the measurement cycle. About 36 μs later, the first ions were detected by the MCP. The estimated TOF of the ions through the separator is about 40 μs, which corresponds to the distance from the end electrode to the measurement station. Therefore, the first ions must have been trapped inside the second SPIG element near to the end electrode. As the potential was lowered, the trapped ions were rapidly extracted from the SPIG forming a small peak in the TOF spectrum. The main bulk of the ions arrive about 200 μs later producing a smoothly increasing profile. Since the repeller electrode was operating at a normal potential during this test, ions entered the SPIG, completely filling it with charge. The potential of the end electrode was raised again at 1850 μs and, about 36 μs later, a very rapid decrease of the signal can be observed indicating that ion beam was blocked.

The observed time profile produced by the repeller pulsing is shown as the red line in Fig.2.19. A delay of $\sim$100 μs occurs between the repeller electrode switching time

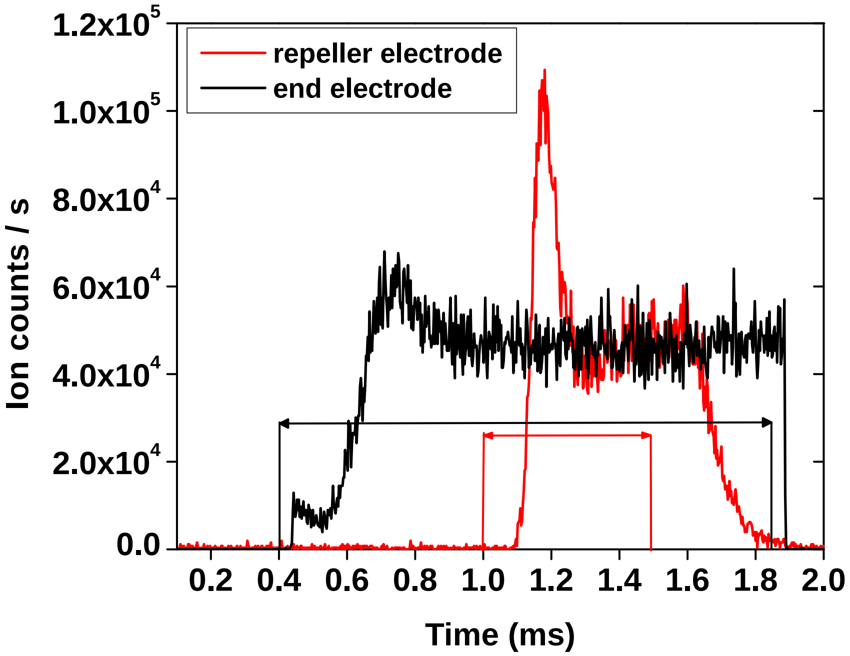

Figure 2.19.: Time-of-flight profiles of mass separated nickel ions. The black line shows the time profile of ions as a function of the end electrode potential switching and the red line shows the same for the repeller electrode. The time periods when the electrodes were active are indicated by the vertical lines.

at 1 ms and the arrival of the first ions. The ion rate rapidly increases, leading to a high peak in the time profile. This corresponds to the situation in which the SPIG is initially empty and begins rapidly filling up. After ~100 μs, the charge density inside the SPIG starts to stabilize and the yield is restored to a normal value about a few tens of μs later due to an increased space charge effect. The potential of the repeller electrode was raised again at 1.5 ms. About 130 μs later, the observed count rate starts to slowly decrease as the ions slowly drift out of the SPIG system. In equilibrium, the space charge acts as a shield against the full dc potentials within the SPIG system. As a result, the decay time of the count rate is far longer compared with the rising time.

The time profiles shown above can be used for estimating the flight time of ions through the SPIG system for both the normal and the LIST modes. The time profiles are differentiated and simple Gaussian shapes are then fitted to the peaks. The average TOF can be approximated from the center of the fitted peak by subtracting the trigger offsets and the flight time through the separator. The width of the fitted peak reflects the time distribution of the arriving ions. By this procedure, the flight time through the SPIG system has been estimated to be ~100 μs in the LIST mode and ~200 μs in the normal mode.

2.5.6. SPIG efficiency measurement

In January 2008, an on-line measurement with the light-ion ion guide was made in order to study the transmission efficiency of the SPIG system as a function of the output current of the ion guide. A proton beam of 40 MeV impinged onto a 4.3 mg/cm^2 magnesium target and the reaction products were stopped in a 3 cm^3 stopping volume containing 300 mbar of helium. The total output current of the ion guide was measured using a Faraday cup between the ion guide and the repeller electrode. The total current after the SPIG system was measured with a Faraday cup located just after the extractor and ground electrodes. For comparison, the case of $A = 20$ was simulated using similar parameters as in the experiment. The comparison between the simulation and the experimental efficiencies as a function of the output current of the ion guide is shown in Fig.2.20.

Care should be taken when interpreting the experimental data since the beam was accelerated up to 30 kV before it reached the second Faraday cup. It is, however, assumed that the effects of secondary electrons due to the beam impinging on the cup are negligible. Up to currents of ~100 nA the SPIG seems to transmit the incoming charge with 100 % efficiency. As the current increases the transmission efficiency steadily decreases before tending towards saturation after a few μA. A transmission efficiency of 50 % is reached at a beam current of ~600 nA. According to these results

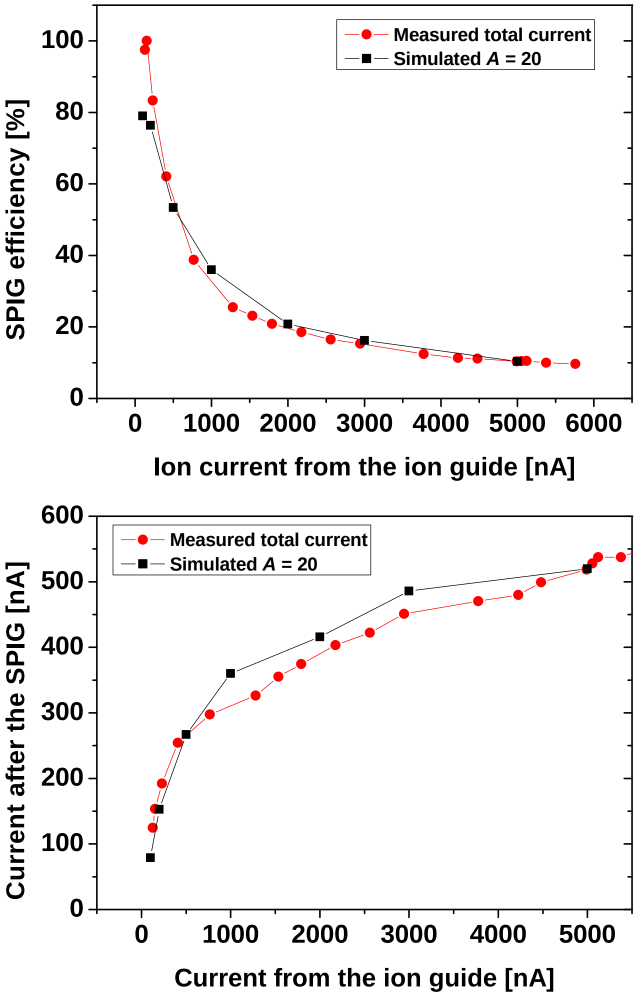

Figure 2.20.: Measured efficiency (top panel) and beam current (bottom panel) of the SPIG system as a function of the beam current from the ion guide in a realistic on-line condition. The pressure of the helium gas in this case was 300 mbar and the rf parameters were 3 MHz and 250 V. The simulated transmission efficiency and current for A=20 are shown for comparison.

Table 2.2.: Summary of the on-line yields.

Reaction	Ion guide	SPIG [ions/μC]	Skimmer [ions/μC]	SPIG gain
^{40}Ca(p,n)^{40}Sc	Light ion	109	14	7.8
^{40}Ca(^{3}He,n)^{42}Ti	Light ion	290	40	7.3
^{nat}Ni(^{32}S,5p3n)^{82}Y	HIGISOL	1000(300)	1000(200)	1
^{238}U(p,fission)^{112}Rh	Fission	18250	3656	5.0

the SPIG is able to effectively transport ion beams up to $\sim 10^{12}$ ions/s. The beam from the ion guide is dominated by light masses, of which helium, oxygen, nitrogen and water form a major fraction. Therefore, the simulation result for the light mass region should reproduce a similar behavior as compared to the experimental curve. In fact, as shown in Fig.2.20 especially at higher currents, the simulation curve follows the experimental data very closely. The agreement between simulation and experiment is impressive, particularly when taking into account that the two are not normalized to each other and the experimental results were not used to adjust the simulations.

2.6. Discussion about the SPIG system

2.6.1. SPIG performance

As compared to the traditional skimmer electrode, there are many benefits provided by the SPIG system, the most important being the improved efficiency and beam quality. Examples of efficiency gain with the SPIG as compared to the skimmer electrode are given in Table 2.2.

A general gain of the yield provided by the SPIG in light-particle induced fission reactions is about 5. The current output from the fission ion guide is typically a few μA and the SPIG gain may be mostly related to the better charge handling capacity as compared to the skimmer electrode. A more impressive improvement of $\sim$7 - 8 when using the SPIG has been seen using light-particle induced fusion reactions. Due to the ionization caused by a primary beam when passing through the gas volume of the light ion guide, higher output currents compared to those from the fission guide can be expected. In addition to this, the performance of the fission ion guide was studied with ^{112}Rh, which is three times heavier than the ions used in the aforementioned light-ion guide tests. A fraction of the difference between the two gain factors would thus also reflect the better performance of the skimmer for the heavier ions that are not scattering from the buffer gas as severely as the lighter ones. The most surprising result is, however, that the SPIG did not improve the yields of HIGISOL reactions. The reason for this is not yet fully understood.

In addition to the yield gain, an improvement of the beam quality was also expected for the present SPIG. The general improvement reported in [17] was about 4 - 5, while with the present system an improvement factor of ~2 is reached for similar reactions. However, as shown in the simulations, the beam quality of the SPIG suffers from the space charge effect. Physically bigger devices suffer more than the smaller ones and therefore some order of reduction of the beam quality can be expected.

Main differences between the SPIG and the skimmer have been explained using simple simulations. In spite of approximations for the gas flow and the space charge effect, the general agreement between the simulations and experimental results is very good. In particular, the experimentally observed differences in the beam qualities and efficiencies at higher masses can be reproduced remarkably well.

With a few small upgrades, the introduced simulation model may provide some additional support for the development work of new types of ion guide that are planned to be used together with the SPIG. The changes in operational conditions of the SPIG as well as in the properties of the gas flow in new designs and concepts may be surprisingly remarkable. Examples of such development works are cryogenic and liquid helium ion guides/catchers [52, 53], in which ambient conditions and gas flow are very different compared to the traditional ion guide. As long as the main transportation of ions inside the SPIG occurs via buffer gas flow, some differences in both the beam quality and efficiency can be expected in such cases. Even though detailed information about the operation of the SPIG is not required for the general use of these designs, the information is relevant when the efficiencies of different concepts need to be addressed and compared to each other during commissioning phases.

2.6.2. SPIG related problems

Endurance of electronics

The electrical part of the SPIG is far more complicated than compared with a single dc power supply required for the skimmer. Although high voltage supplies and a WAGO system, which is used as an interface between the control computer and the dc supply hardware (see Appendix A) are quite robust, the rf section formed by the amplifier and the function generator has turned out to be rather sensitive.

In addition to physical damage of the devices, problems are encountered with the communication between the rf hardware and the computer. In particular, the USB link used in the communication between the computer and the function generator, is quite unsuitable to the chosen task. The main problem of the USB bus link relates to the complexity of the communication protocol it uses. Unfortunately, the support of simpler and more robust protocols such as RS232 or CAN, for example, is very unusual nowadays.

Discharges

A possible problem when working with electric voltages in poor vacuum conditions is discharging. In this work, discharging of the SPIG system has been seen when argon buffer gas is used. High voltage discharging in gas can be approximated using the Paschen law [54], which states that the breakdown voltage U_{BD} in a gaseous media depends on the product of the gas pressure p and distance d between the electrodes ($p \times d$). In [55], this law is formalized as

$$U_{BD} = \frac{pd}{ln(Apd) - ln(ln(1 + 1/\gamma)}, \tag{2.7}$$

where A, B and γ are the Townsend discharge parameters.

The breakdown voltage in the SPIG system environment was determined experimentally. A perspex model of the SPIG, equipped with two adjustable copper plate electrodes aligned perpendicular with respect to the optical axis of the SPIG, was mounted in the IGISOL chamber. The electrodes were positioned as close to the repeller electrode as possible, since it was observed to be most sensitive to discharging. To deduce the Paschen curve, the pressure inside the SPIG was separately measured using the closed SPIG and a 0.4 mm Pitot-probe connected to a capacitive pressure sensor. Although there were some small geometry differences between the closed SPIG and the perspex model, the pressure distribution measured with the closed SPIG was considered to be sufficient for this purpose. Fig.2.21 shows the measured dc discharge ignition curve for argon gas as a function of the product of electrode gap and pressure between the electrodes. The Paschen curve defined by Eq.2.7 and the experimental result measured with a 2 mm electrode gap in [56] are also shown for comparison. As seen from the figure, the maximum potential difference before discharging between the 2 mm electrode gap is slightly below 300 V for typical ion guide pressures in the SPIG case.

There is a clear difference between the experimental and theoretical curves. The Paschen law takes into account only the properties of the gas. However, as discussed in [56, 57], the breakdown voltage is also a function of the electrode gap solely and should thus be formalized as $V_{BR} = f(pd, d)$. Moreover, according to [58], the breakdown voltage also depends on the cathode material. The differences can therefore be understood being due to simplifications in the theoretical approach.

There is also a noticeable difference between the results of this work and [56]. In both measurements, similar cathode materials and electrode gaps were used. On the other hand, in [56], relatively large electrodes shielded with insulating walls were used in order to avoid edge effects. Due to the small inner diameter of the SPIG, such an arrangement was not possible in this work. In general, the breakdown voltage should be measured using a static gas pressure between the electrodes. Due to the gas flow inside the SPIG, the gas atoms may not be homogeneously distributed between the electrodes. Instead, it is more likely that the atoms form a density distribution, whose shape may vary as a function of the ion guide pressure. In [56], the breakdown voltage was defined as a voltage where the insulation of the gas started to reduce and so-called Townsend discharge was initiated. In this work, the breakdown voltage was recorded after the Townsend discharge phase, just before it turned to a light-arc discharge and started to ionize gas atoms. In this phase, a current through the electrodes starts increasing dramatically, and the operation of the SPIG becomes disturbed by the discharge.

Due to a large aperture of the repeller electrode and a short distance to the ion guide nozzle, a longitudinal electric field generated by the repeller is not very efficient at blocking the ion beam. In LIST experiments with argon gas, the experimentally observed potential needed for repelling is above +100 V with respect to the ion guide [60]. Moreover, since the axial electric field inside the SPIG is rather low, the dc potential difference between the repeller electrode and the rods of the first SPIG is relatively high, a few 100 V. Thus, the required potential difference between the electrodes may exceed the $\sim$300 V limit leading to discharging of the system. The situation becomes worse if an rf signal is applied to the rods. It was also observed that the rf signal solely was able to initiate a discharge inside the SPIG system. The required rf amplitude for argon gas was surprisingly low, less than 100 V_{0-p}. In fact, an rf discharge can also be estimated using a modified Paschen law. One such modification is discussed in [61], stating that, in addition to a product of the pressure and the electrode gap, the breakdown amplitude is a function of a product of the electrode gap and the rf frequency. The rf amplitude breakdown curve has not been accurately measured in this work and it is not available for the realistic SPIG system conditions from [61] either.

A SPIG with a segmented enclosure was recently tested in order to improve the acceleration of the ions inside the first SPIG element. This test was performed with the discharge ion source. In order to maintain feasible discharge conditions inside

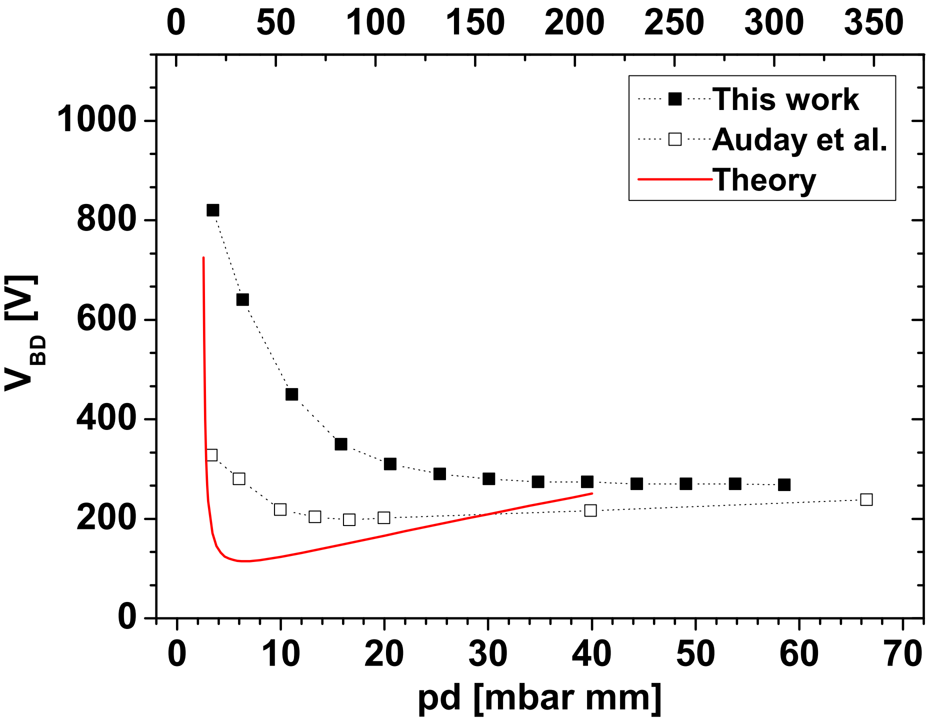

Figure 2.21.: Measured breakdown voltage as a function of argon pressure and a 2 mm gap between the electrodes. For comparison, the experimental result measured with a 2 mm electrode gap in [56] and the calculated curve based on Eq.2.7 are also shown. For the calculation, the Townsend discharge parameters for argon gas (A = 10.20 Pa/m, B = 176.27 V/Pa m and γ = 0.095) were adopted from [59]. The top axis indicates the corresponding pressure value in mbar units measured at the inlet of the ion guide when a 2 mm electrode gap is used.

the ion guide, only a low buffer gas pressure was permitted. For such pressures, however, no significant improvement was provided by the segmentation. The same SPIG was later used in connection with laser ion source tests, operating at high gas pressures. It was found that with the highest available dc and rf voltages applied to the electrodes, discharges could not be ignited. In addition to the segmented enclosure, the main difference between this and the normal SPIG was a thinner insulator between the repeller and the enclosure (see Fig.2.5). In normal operation conditions, the pressure in this region is around 10 mbar. According to Fig.2.21, this pressure together with a 2 mm electrode gap between the repeller and the SPIG rods ($pd = 20\ mbarmm$) matches to the end of the high curvature region of the breakdown voltage curve. Therefore, a slightly smaller gap will improve the tolerance to higher voltages.

2.6.3. Future developments of the SPIG system

The requirements for an optimal gas jet geometry for the LIST mode has been intensively studied, resulting in the proposal of utilizing a so-called “De Laval” nozzle, commonly used in rockets [62]. Although a control over the background pressure inside the SPIG may be required also with this nozzle, the need for two SPIG elements separated by an adjustable iris is no longer valid. The possibility of using only one SPIG element would greatly simplify the electronics and would also remove the discontinuity of the rf field between the elements as well as problems related to an axial alignment of the rods.

In addition to gas jet creation and discharges, one known problem is an insufficient axial electric field inside the SPIG segments. According to the simulations, the axial motion of ions is governed primarily by the gas flow rather than by the weak axial electric fields generated by the electrodes located at the ends of the SPIG elements. Since the charge density inside the SPIG system is defined mainly by the axial velocity of the ions, axial motion control plays a significant role in the possible reduction of space charge effects. It is worth noting that the problem of axial field generation applies mainly to the normal operation of the SPIG. In the LIST mode, a sufficiently long gas jet offers a good axial transport mechanism for the laser ions. Moreover, the charge density created by laser ions is not enough to disturb the operation of the SPIG system.

The transmission efficiency of the SPIG in both operational modes can be improved by introducing a stronger axial electric field inside the SPIG elements. One possibility is to install wedge-shaped dc electrodes between the rods as briefly discussed in [63]. However, the electric field generated by these wedges cannot be modified without changing the geometry. Moreover, electrodes located between the rods significantly hinder the gas evacuation inside the SPIG, making this solution unpractical. Another solution is the use of segmentation as was proposed for the original LIST concept. This allows the manipulation of the electric field by varying the voltages of different segments. Depending on the lengths of the segments the electric field may be quite discrete introducing sharp changes and flat regions. A more novel approach replaces the conducting rods of the SPIG elements with weakly conducting ones. One such device, developed at RIKEN, is introduced in [64]. The carbon OPIG (Octupole Ion Guide) uses eight carbon rods, each with an electrical resistance of order 1 Ω/cm. A similar approach may be suitable for a new SPIG design although due to the significantly shorter rod length of the SPIG as compared to the RIKEN OPIG, a less conductive material might be more appropriate.

3. Isotopic fission yield distribution measurements at IGISOL

3.1. Nuclear fission

In nuclear fission a heavy nucleus splits into two lighter nuclei and emits several neutrons. Since the nuclear binding energy per nucleon is significantly higher for the medium mass nuclei, the reaction as such is exothermal. To be able to fission, the nucleus has to first stretch to a very elongated shape. It requires energy to deform the nucleus to the so-called saddle point, after which energy is released. In more scholarly terms, there is a potential barrier against the fission. The height of the barrier can be estimated on the basis of the liquid drop model. Including shell effects gives a more accurate prediction [65]. For medium heavy nuclei, the fission barrier is of the order of 50 MeV, while for actinides, it is only of the order of 5 MeV.

Fission can take place via quantum mechanical tunneling through the barrier, leading to spontaneous fission (SF). Spontaneous fission is a rare process for naturally occurring isotopes. For ^{238}U, the partial SF half-life is 8×10^{15} years [66].

Fission can also be induced via introducing energy to the nucleus. The energy may be brought to the nucleus as electromagnetic radiation (photofission), or via a particle. Use of a neutron is a special case, since when a neutron is captured by a nucleus, the neutron binding energy is available as the excitation energy of the formed compound nucleus. Sometimes it is enough to overcome the fission barrier, meaning a neutron at zero kinetic energy can induce fission, as in the case of ^{235}U. It is worth noting that the fissioning system is in fact ^{236}U. In other cases such as the neutron-induced fission of ^{238}U (fissioning nucleus ^{239}U) the neutron binding energy is not sufficient to initiate fission, resulting in a threshold energy of about 1 MeV. In charged particle induced fission there is always a threshold due to the Coulomb barrier experienced by the incoming projectile.

After the threshold energy is reached, the total fission reaction cross section remains constant, until about 8 MeV from the threshold there is again a stepwise increase of cross section. This is related to one neutron evaporation from the compound nucleus, leading to another compound nucleus that can fission as well. This is generally called second change fission. If the energy is increased further, there will be additional particle evaporations and thus multiple chance fission. This has influence on fission yield distributions.

Fission is a slow process in the nuclear time scale, of the order of 10^{-14} s, since it is a collective process in which all the nucleons participate. As a consequence, the fissioning compound nucleus loses any possible memory of its formation. It has been shown in [67] that the yield distribution in the fission of ^{236}U does not depend on whether the nucleus is produced via n+^{235}U or α+^{232}Th as long as the excitation energy of the compound nucleus is the same. This is utilized in what is usually known as the surrogate method ([68] and references therein): for example, neutron-induced fission (n,f) can be studied using a (d,pf) reaction, since the compound nucleus is the same.

Proton-induced fission cannot in general be used to experimentally mimic neutron-induced fission because it is difficult to find a pair of actinide targets with which the same compound nucleus could be reached. On the other hand, differences of model parameters for proton- and neutron-induced fissions are assumed to be relatively small. Therefore, data from proton-induced fission has been used to develop and adjust theoretical models for neutron-induced fission in particular for high projectile energies energies ([10] pages 124 and 182).

3.2. Fission yields

Fission is characterized by a wide distribution of reaction products. In nuclear fission the compound nucleus splits into two complimentary neutron rich primary fission fragments. In symmetric fission the mass of the fragments is roughly the same. In asymmetric fission the mass of fragments is clearly different. These fragments are also usually highly excited, which leads to an emission of prompt neutrons, followed by the emission of prompt γ-rays. At this stage, the fragments are called primary fission products.

It is important to note that the yield distributions of the primary fission fragments before the prompt neutron evaporation are different from those of primary fission products after the neutron and γ-emission. In this work, the post-neutron emission yields of primary fission products are deduced.

It is important to distinguish between the independent and cumulative fission yields. The independent, or direct yield, of a fission product is simply the probability of its formation directly in fission. The cumulative yield is the probability of accumulation of a fission product directly from fission in addition to the decay of its precursors. The cumulative yield of a certain isotope is often a practical measure for monitoring the fission process. The cumulative yields can be determined experimentally, or deduced from the independent yields.

Fig.3.1 displays an example of the independent fission product yield distribution.

It is a two-dimensional distribution of nuclei in the proton-neutron space from which the one-dimensional distributions that are usually discussed can be seen as either projections or cuts. The mass yield distribution is the projection of the independent yields to mass number A. Other yield distributions are the elemental distribution, i.e., the distribution of nuclear charge, which is the projection of the independent yields to proton number Z, isotopic yield distribution that is a cut of the yield distribution along a fixed Z, and the isobaric yield distribution, a cut of the two-dimensional yield distribution along a fixed A.

A characteristic feature in the low energy fission of nuclei in major actinide region is the double-humped structure of the yield distribution. This is explained by the shell structure of the nuclei. The higher mass peak is stabilized by the Z = 50, N = 82 shell closure. Its position does not depend on the fissioning system. Therefore, the lower mass peak moves depending on the fissioning system. In the case of multiple change fission where nucleon evaporation from the compound nucleus produces several fissioning systems, a broadening of the lower mass peak occurs as compared with single change fission. At higher energies the shell effects have less importance, and the symmetric fission is more pronounced. The shell effects are, however, not totally washed away: in 200 MeV neutron-induced fission of ^{238}U the symmetric component in the mass yield distribution is two orders of magnitude more pronounced than in 20 MeV neutron-induced fission. The mass yield distribution is, however, still best fitted with one symmetric and four asymmetric Gaussian components ([10] pages 173 and 174). The symmetry of the fission products does not only depend on the excitation energy but also on the mass of the fissioning system. The asymmetric fission mode is a dominant factor in low energy fission of major actinides whereas the symmetric fission mode is more pronounced for lighter and heavier masses, being the only mode for so-called pre-actinides ($A \leq 227$) and high-actinides ($A \geq 257$) [10].

3.3. Fission yield applications

Accurate experimental fission yield information is needed in many fields of physics. In fundamental physics, the information is relevant for understanding the fission reaction and the probability of the fragment formation of a fissile material with various inducing particles and incident energies. Fission with low energy projectiles, particularly neutrons, is rather well known and experimentally studied. At higher projectile energies, however, the reaction becomes more complex due an increased number of particles emitted during a single fission reaction (second and multiple chance fissions). Theoretical modeling of such a reaction is difficult and inaccurate

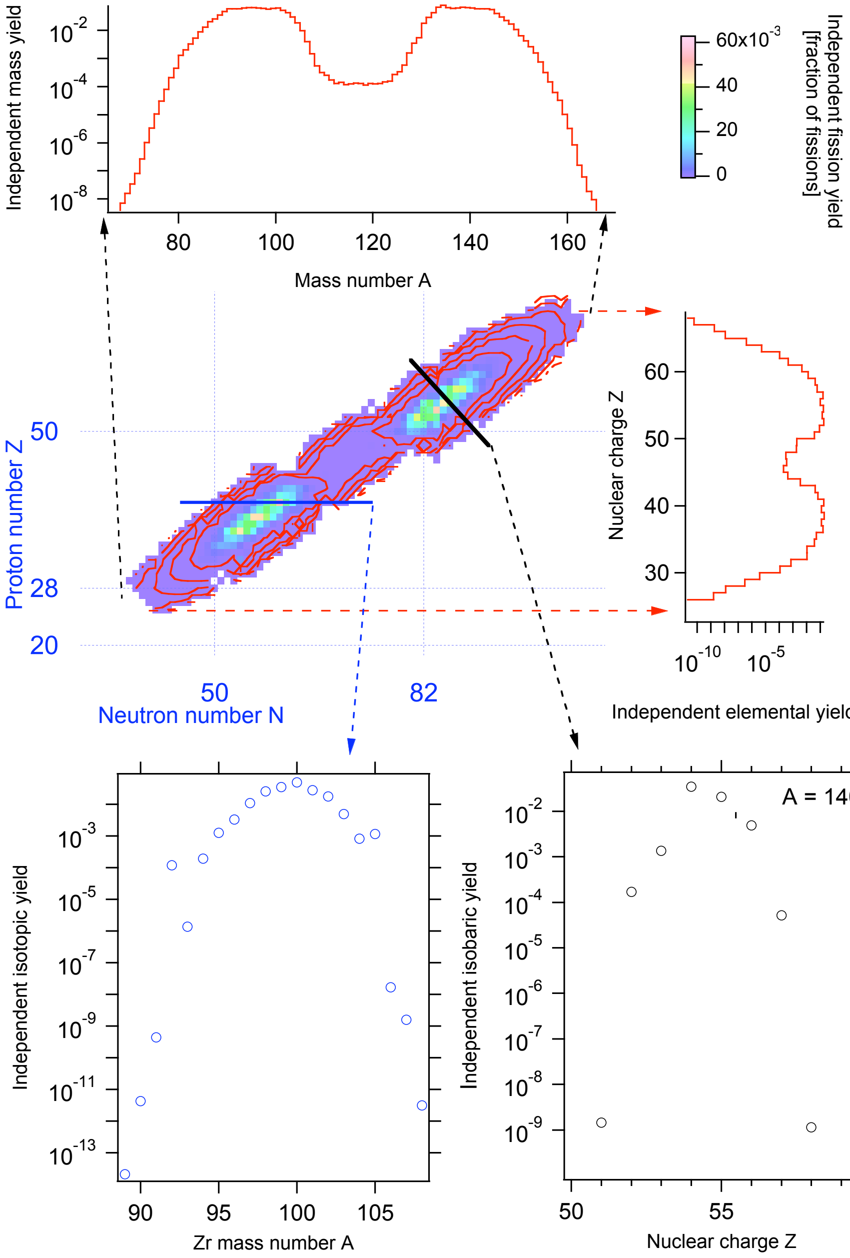

Figure 3.1.: Independent yields of thermal neutron-induced fission of ^{235}U. Data are from ENDF/B-VII.0 library [69] via the NuDat [66] service. The figure shows how the independent mass yields, elemental yields, isobaric yields and isotopic yields are projections and subsets of the complete independent yield distribution.

mainly because of a lack of accurate experimental data. The development of more accurate models of fission reactions benefits designs of new innovative fission reactor types and nuclear waste handling methods as well as the design of fission targets for next generation ISOL facilities.

In the field of fission energy, fission yield information plays a very important role in both reactor design and operation phases. This information is used in criticality and reactivity calculations in order to sustain the fission reaction and to avoid over-critical fuel designs. Fission yield information is also relevant for many reactor-related safety issues, such as the detection of possible fuel failures and the estimation of radioactive contamination in fission product gases and reactor components. Accurate fission yield information, also including isomeric production ratios, are needed for so-called decay heat calculations [70]. These calculations are important for the prediction of the heating effect caused by radiation emitted from fission products and actinides present in the fuel. This information in turn is relevant for the determination of the required cooling capacity and time needed after reactor shutdown. The information of fission products present in the fuel and the core of the reactor is also important for the reprocessing of spent fuel and the management of nuclear waste [9].

Nuclear waste removal through transmutation has been intensively studied during the last few decades, resulting in several proposals using classical thermal or fast reactors or accelerator driven systems. Although the coverage of present nuclear data and the accuracy of theoretical models is adequate for thermal and fast reactor incineration, additional fission information and more accurate models are required for the accelerator driven system especially from intermediate and high energy fission reactions. In traditional fission reactors, radioactivity caused by the fission products is not a problem as it decays to the level of the activity of natural uranium already after 300 years. However, the total activity of the fuel remains higher over 10^4 years. This is mainly due to production of ^{239}Pu and minor actinides via neutron capture and β-decay processes in the fuel. These products are α-emitters with very long half-lives and are thus responsible for most of the toxicity of the fuel and waste. [10, 11]

In the field of reactor physics, two different kinds of information is needed. Firstly, a complete yield distribution is required for accurate calculation of fission product inventories. These are required for most reactor and spent fuel applications and especially for decay heat and reactor shutdown calculations. Secondly, accurate fission yield information for specific fission products is needed to be used as reference yields for measurement standards or monitoring fission products for burnup determination and safety systems. The present validated fission yield data can be found in several data libraries, e.g. ENDF/B-VII.0 (2006) [69, 71], JEFF-3.1/NFY&SFY (2008) [72], CENDL-3.1 (2005) [73] and JENDL-4.0 (2010) [74].

In general, it is rather expensive to produce comprehensive experimental datasets of fission yield distributions for various actinides, projectiles and incident energies. Therefore, the more economical solution is to develop accurate fission models based on a few, accurate experimental measurements and to try to estimate missing yield information using these models. The present evaluated data covers the major fraction of fission mass distributions for thermal and low energy neutron-induced fission of major actinides. The information provided by models and simulations are mostly adequate for present reactors but insufficient in accuracy for new reactor designs and waste reprocessing methods that require accurate data from intermediate and high energy neutron- and charged particle-induced fission reactions and from fission reactions of ^{239}Pu, minor actinides and some non-actinides such as Bi and Pb, for example. In order to improve the present models, more high accuracy experimental data is required especially from the aforementioned cases. It is worth noting that most of the present experimental data related to thermal and low energy fission has been measured several decades ago. The accuracy of those yield distributions has been improved by combining and averaging the data of several separate measurements. In many cases, however, the accuracy of the present data is not fully sufficient for future needs and should also be improved. [9, 10, 75]

In addition to energy production, fission yield information can support the design of new fission targets for next generation ISOL-based radioactive beam facilities, such as EURISOL [8]. Although primary projectile energies in those facilities will be much higher than used in this work, intermediate projectile energies are present via secondary particles emitted during the primary fission reactions or produced directly via (p,xn) reactions. In a suitable target configuration, these secondary particles may also induce fission reactions leading to an enhancement of neutron rich fragments as interpreted in [76].

3.4. Fission yield measurement techniques

The large number of simultaneously produced fission fragments makes experiments observing the primary fission fragments complicated. Independent or relative fission product yields can be measured in several different ways, each with its own advantages and disadvantages. In this section, some classical and modern measurement techniques are briefly introduced.

The first method for yield determinations was radiochemical. In this method, a sample of the fissile material was irradiated and the fission products were rapidly radiochemically isolated. After the radiochemical isolation the absolute activity of the fission product was determined via radioactive β- or γ-spectroscopy. A discussion about radiochemical methods in yield determination can be found in [77]. Although the development of fast chemical isolation methods has established the studies of products with sub second half-lives, the method has mainly been overcome by modern, more physical approaches.

In the ISOL technique, a sample of fission products is first generated inside a thick target system, which is heated to $\sim$2000 °C. The fission products evaporated or diffused out from the target are introduced to an ion source, where they are ionized usually by means of surface ionization. Ions are mass separated and are counted using γ spectroscopy. Due to thick target systems, this method is relatively slow and chemically selective. Therefore, it cannot be easily applied to very exotic fragments and studies are usually limited to highly volatile elements that easily diffuse out from the target system. In some highly volatile cases such as Rb, Cs, Ga and In, the chemical selectivity of the ion source can be utilized in such a way that only products of a selected element are released from the target. In these cases, pure ion beams of single isotopes can be produced by means of a simple magnetic separation. It is thus possible to use ion counters for accurate determination of the intensities of these fission products [13, 14, 78, 79]. The elemental selective laser ionization can be utilized in the same way. Another possibility is to volatilize fission products of several different elements at once by using higher target temperatures. These products are usually selectively ionized by laser or surface ionization, mass separated by magnetic fields and studied via γ-spectroscopy as done in the study of neutron-induced fission of ^{238}U at PARRNe [80] and in the study of high energy proton-induced fission of ^{238}U at ISOLDE [81], for example.

A variant of the ISOL method, the IGISOL technique described in Chapter 2, uses thin targets, which makes it fast and chemically non-selective. It is thus possible to provide fission fragments of even very refractory elements, making it very suitable for fission yield distribution studies. In fact, a significant fraction of presently available independent yield data in proton-induced fission has been produced using the IGISOL technique [82–92]. The main problem of the IGISOL method has been related to a mass resolving power insufficient for isobaric separation. Therefore, the only way to resolve mass separated isobars had previously been via a study of radioactive decays. As a result, long measurement periods were required to reach a sufficient statistical accuracy. A more serious problem has been the lack of knowledge of the decay schemes of the most exotic nuclei. The selectivity of the traditional ion guide method can be improved with laser ionization. The yields for Co, Ni, Cu and Ga in proton-induced fission of ^{238}U have been measured at LISOL using resonant laser ionization [93]. The LIST method, discussed in Chapter 2, can be used in the same way.

It is also possible to measure the yield of fission products using γ-ray detectors located near to the irradiated fission sample. This method is suitable for measurements of fission mass chains for very exotic samples since it requires only a small amount of fissile material. The analysis of the data is, however, complicated and requires accurate information about the decay characteristics of the measured products. For independent yields, duration of the counting is limited by shorter half-lives of fission products. This increases measurement times and leads to reduced statistical accuracy. Even though the accuracy of this method is limited, it has been used for thermal neutron-induced fission yield studies in [94–96].

All techniques listed above are based on measurements of stopped fission fragments. It is also possible to deduce the mass number A of complementary fission fragments without stopping them. This technique is based on the conservation of momentum in fission, which allows calculation of the masses of complementary fission fragments from their kinetic energies and velocities. This method is applicable for low energy and light particle-induced fission reactions, in which the momentum of the inducing particle may be ignored. An additional requirement is a thin target system, in which the energy loss of the fission products is small. The energy of fission products can be measured using surface barrier detectors, for example, while the velocities can be calculated from time-of-flight information of the products.

Probably the most famous instruments utilizing this energy/velocity method are Cosi fan tutte [97, 98], Hiawatha [99] and Lohengrin [12]. These instruments are coupled to fission reactors providing high neutron fluxes and can be equipped with a detector that identifies the nuclear charge of the fission fragments. This allows the exploration of independent yields in low energy neutron-induced fissions. In Cosi fan tutte, the determination of velocity and energy occurs for all fission fragments regardless of their mass, energy or charge state, while the two latter instruments introduce separation before the detection of the fragments. In both instruments, the separation is performed according to the energy and charge state ratio (E/q) of the products and, in Lohengrin, the separation occurs in addition according to the mass and charge state ratio (A/q) of the products. Therefore, in order to produce the independent yield distributions using these two facilities, the measurements have to be repeated for various different kinetic energy values of the products. At Lohengrin, the measurements need to be repeated also for several different charge state values. Due to the relatively poor Z-resolution of the instruments, the measurements are limited to the light mass region (up to $Z = 47$). In this region, the energy/velocity method has been used to measure almost complete sets of fission products in low energy neutron-induced fission of various fissile nuclides.

Yet another way to measure yield distributions is to make use of so-called inverse kinematics. In this method, the studied nuclide is used as a high energetic projectile and is directed to a stationary target. When the studied nuclei pass through the target some excitation energy is transferred and the nuclei undergo fission. The fission fragments can then be mass separated by a fragment separator as is done with the FRS at GSI [100], for example. This method provides the possibility to study the fission of almost any nuclide in the region above lead. The accurate determination of excitation energy and compound nucleus composition may be, however, rather difficult due to the complexity of the excitation process of the nuclide.

In order to accelerate and simplify the measurement of the fission yield distributions, a novel method has been developed in the University of Jyväskylä. This method takes advantage of the chemical non-selectivity of the ion guide method and combines it with the superior mass resolving power of the JYFLTRAP facility [15, 101], which allows identification of ions based on their mass alone. This combination provides an accurate and rapid way to measure isotopic yield distributions for a wide range of fission produced isotopes. An MCP (Multi-Channel Plate) detector with a high detection efficiency ($\sim 60\%$) is used as an ion counter and hence, only the half-lives of short lived species are needed for the yield analysis. Due to the chemical reactions introduced by the ion guide and JYFLTRAP facility, this method cannot be solely used as a deduction of the independent fission yield distributions. Nevertheless, the isotopic fission yield distributions provided by this method can be seen as a step towards the independent values; if even one independent yield value of some isotope is known, the isotopic distribution can be directly converted to the fission cross-sections for the rest of the isotopes of this particular element.

3.5. Experimental setup

The study of proton-induced isotopic fission yield distributions has been realized in several separate experiments during the years 2005 - 2007. The first experiment was carried out using the skimmer electrode, while the subsequent two measurements were realized with the SPIG system introduced in Chapter 2. The primary beams from the JYFL K130 cyclotron used in this work are tabulated in Table 3.1, which also contains information about the timing of JYFLTRAP. A schematic view of the measurement apparatus used in these experiments is shown in Fig.3.2. A short description of the ion guide method and the IGISOL front-end operation can be found in Chapter 2.

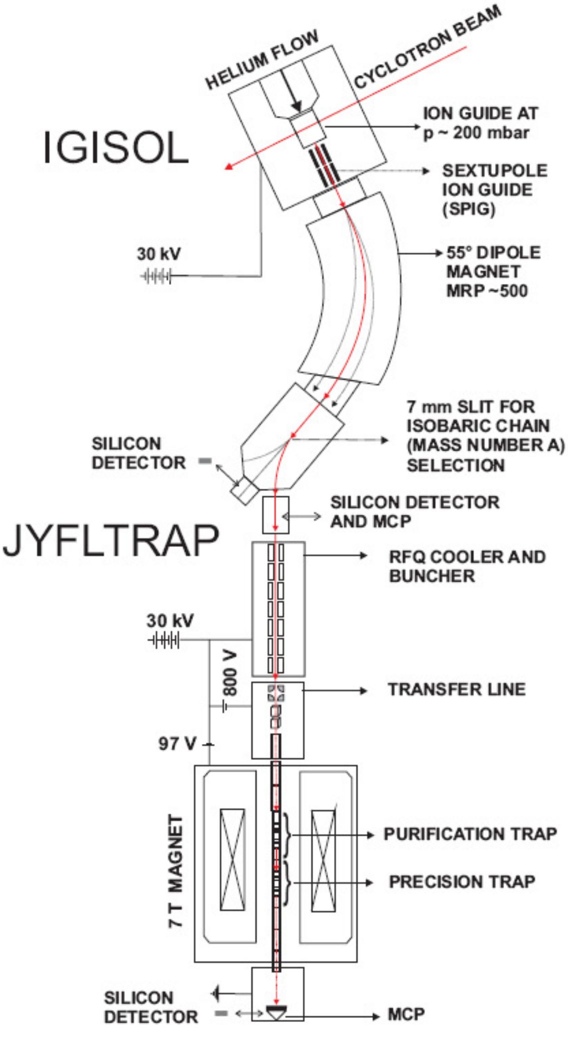

Figure 3.2.: A schematic presentation of the IGISOL and JYFLTRAP facility.

Table 3.1.: Summary of fission yield experiments.

Experiment	Ion guide coupling element	Proton energy [MeV]	Purification cycle t_p [ms]
August 2005	skimmer	25	341
January 2006	SPIG	25 , 50	660
October 2007	SPIG	50	450

3.5.1. IGISOL front-end and mass separator

The fission ion guide was used in this work and is shown in Fig.3.3. In order to prevent plasma effects caused by the primary beam, the small target volume and the $\sim$50 cm^3 stopping volume have been separated by a thin, $\sim$1 mg/cm^2 nickel window. The use of such a separation window is possible because the angular distribution of the fission fragments ejected from the target is almost isotropic and the window has a negligible stopping effect for the full energy fission fragments whose kinetic energy is of order 1 MeV/u. A thin metallic ^{nat}U foil, 15 mg/cm^2 thick, is tilted by 7 degrees with respect to the beam direction, increasing the effective thickness of the target to 120 mg/cm^2. In this work, the helium pressure in the stopping volume was varied between 200 and 300 mbar. The helium gas is evacuated through a 1.2 mm aperture of the exit nozzle, resulting in an evacuation time of a few tens of milliseconds. During that time, limited chemical reactions can occur in the gas volume as deduced in [17]. Therefore, this ion guide can be used for the production of almost any fission fragment with only minimal losses due to chemical selectivity and radioactive decays. An overall efficiency of 0.02 % has been measured for this ion guide with a 10 μA primary beam. This indicates that only a small fraction of the fission products in total are evacuated from the ion guide.

In the first of the three experiments, the ion guide was followed by a skimmer electrode. The distance between the skimmer and the guide was $\sim$10 mm providing an electric field of 300 - 400 V/cm in that region. In the subsequent experiments, the SPIG system was located about 4-5 mm after the ion guide as shown in Fig.3.3.

The fission fragments were mass separated according to their m/q ratio by using the 55° dipole magnet as discussed in Chapter 2.1. The MRP after the dipole magnet was measured to be $\sim$300 and $\sim$500 for the skimmer and the SPIG, respectively. A desired m/q value was selected by a fixed 7 mm slit, aligned vertically with respect to the focal plane of the magnet. Trajectories of mass separated ion beams were manipulated by two electrostatic beam benders. The first bender unit is a parallel

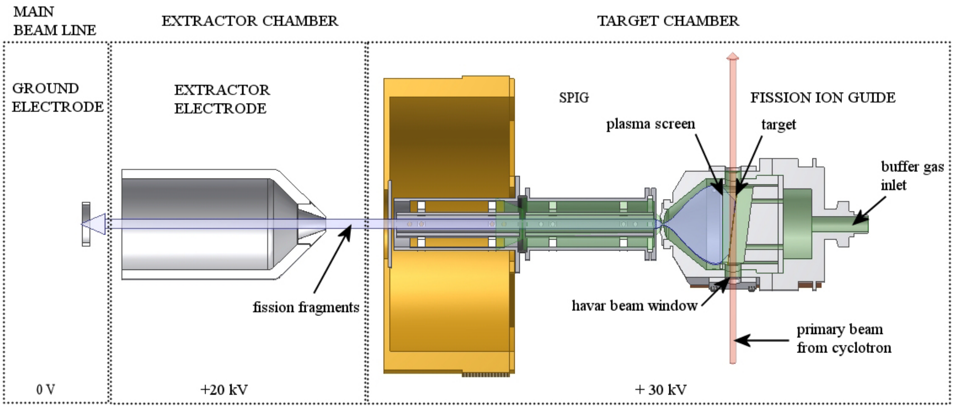

Figure 3.3.: IGISOL front-end setup used in the fission experiments of this work. The red arrow represents the primary beam from the K130 cyclotron, blue illustrates fission fragments and green shows the buffer gas flow. The high voltage platform is also shown. The gap between the ion guide and the SPIG is ~4 mm and between the SPIG and the extractor 20-40 mm.

plate beam kicker that is used to completely block the mass separated ion beam before the slit. The purpose of this kicker is to control the cooling cycle of the RFQ, t_c, as will be discussed later. Following this is an electrostatic 30° beam bender that is used to deflect the ions to the RFQ beam line.

3.5.2. Isobaric purification with JYFLTRAP

Operational principle of a Penning trap

The JYFLTRAP system [15, 102] consists of two cylindrical Penning traps [103], which utilize both electrostatic and magnetic fields to confine ions to a small volume of ~ 1 cm^3. The magnetic field (7 T in JYFLTRAP case) parallel to the symmetry axis of the trap ($\vec{B} = B\hat{e}_z$) provides radial binding for the ions, while the axial confinement is achieved by the static quadrupole potential using three or more cylindrical electrodes as illustrated in panel (a) of Fig.3.4.

Solving the equation of motion described by the Lorenz force

$$m\ddot{r} = q(\vec{E} + \vec{v} \times \vec{B}). \tag{3.1}$$

for an ion having mass m and charge q leads to two radial oscillations at the angular

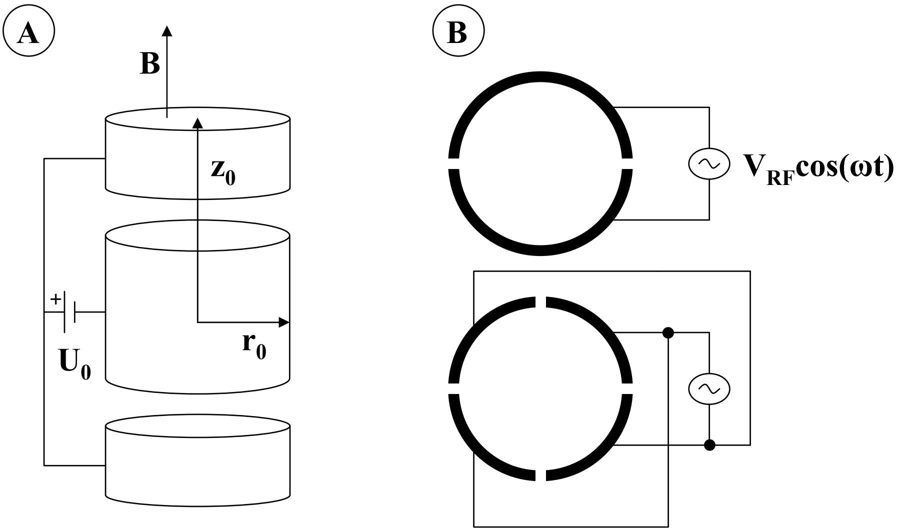

Figure 3.4.: A simplified electrode configuration for a cylindrical Penning trap (a) and radial segmentations of the middle electrode for dipole (top) and quadrupole (bottom) excitations (b).

velocities ω_+ and ω_- and an axial motion at the angular velocity ω_z:

$$\omega_\pm = \frac{1}{2}(\omega_c \pm \sqrt{\omega_c^2 - 2\omega_z^2}) \tag{3.2}$$

$$\omega_z = \sqrt{\frac{qU_0}{md^2}}, \tag{3.3}$$

$$\tag{3.4}$$

where the term

$$d = \sqrt{\frac{1}{2}(z_0^2 - \frac{r_0^2}{2})} \tag{3.5}$$

is the so-called characteristic trap dimension and the angular velocity

$$\omega_c = \frac{q}{m}B \tag{3.6}$$

is the rotational frequency of the charged particle in absence of the electric field. The three eigenmotions corresponding to these angular velocities are illustrated in Fig.3.5. The slow radial oscillation with the frequency $\nu_- = \omega_-/2\pi$ is called the magnetron motion and the motion with the frequency ν_+ the reduced cyclotron motion. The axial motion with the frequency ν_z is a harmonic oscillation in the axial direction of the trap.

Ions can be cooled by introducing buffer gas into the trap [104]. Collisions between the ions and gas atoms decrease the amplitudes of the fast (axial and the reduced cyclotron) motions. The amplitude of the magnetron motion, however, slowly increases due to the repulsive effect caused by the electrostatic quadrupole field.

The eigenmotions can be manipulated using azimuthal dipole or quadrupole rf fields. For this purpose, the middle ring electrode of the trap has been split into two (top) or four (bottom) segments (see panel (b) in Fig.3.4). The dipole excitation with a frequency of ν_- increases the magnetron oscillation amplitude whereas the dipole excitation with a frequency of ν_+ increases the reduced cyclotron oscillation amplitude. If the rf-excitation is performed using the quadrupole configuration with sum frequency $\nu_+ + \nu_-$, for example, the two radial eigenmotions can be coupled, leading to conversion between these two motions.

Cooling and purification of ions

The energy spread of the mass separated ion beam after the dipole magnet of IGISOL is too large for effective injection directly into the Penning trap. Therefore, ions to be delivered to the Penning trap are cooled and bunched by an rf cooler/buncher

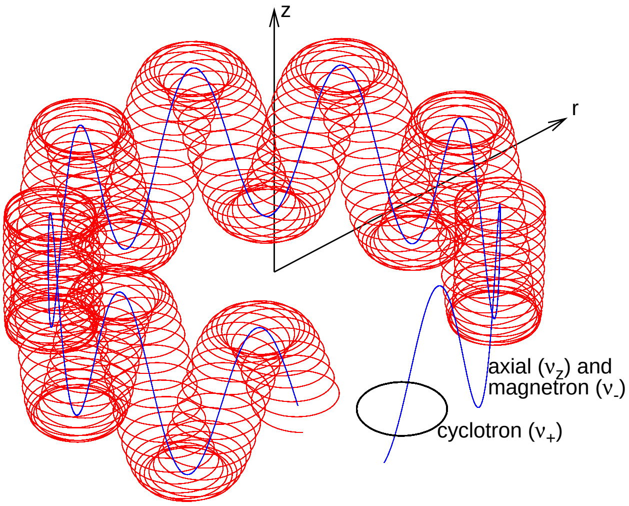

Figure 3.5.: Motion of an ion in a Penning trap. The motion is actually a sum of three eigenmotions: the reduced cyclotron motion with a frequency of ν_+, the magnetron motion with a frequency of ν_- and the axial motion with a frequency of ν_z.

apparatus, hereafter called an RFQ [105]. Capturing an ion bunch is a much more straightforward procedure than capturing a continuous beam.

The RFQ is a segmented linear rf quadrupole, in which helium gas is used to reduce the kinetic energy of the incoming ions via buffer gas cooling. The mass separated ions are accumulated inside the quadrupole field containing $\sim 10^{-2}$ mbar of high purity (99.99990 %) helium gas. The ions' axial confinement occurs via a dc potential applied to the segmentation. The effective potential in the radial direction created by the quadrupole rf field pushes ions towards the symmetry axis of the RFQ. Due to collisions with buffer gas atoms, ion oscillation in the rf field damps out and its kinetic energy decreases down to the level of the buffer gas energy. More detailed information about the buffer gas cooling especially in rf quadrupoles can be found in [33] and references therein. After a cooling period, ions are released as a short, $\sim$15 μs, bunch to be injected into the first Penning trap for further manipulation. The typical time required for cooling the ion beam energy down to eV level is about few milliseconds. In this work, however, the cooling and accumulating time t_c was matched to the isobaric purification cycle length t_p due to practical reasons described in Section 3.6.3.

Isobaric purification of the ion beam takes place inside the first Penning trap called the purification trap, which is filled with about 10^{-5} mbar of helium gas. The ion bunch is captured inside the trap by lowering the axial potential wall at the injection side below the kinetic energy level of the ions. Once the bunch has arrived into the trap the wall is restored creating a potential minimum (in the axial direction) at the center of the trap. The purification cycle is initiated with a cooling period. As described above, this cooling procedure reduces the radii of the axial and reduced cyclotron motions. After the cooling period, only the magnetron motion is left and all ions rotate around the center of the trap with slowly increasing magnetron radii. The amplitude of the magnetron motion is increased by a dipole excitation at the magnetron frequency ($\sim$1700 Hz), which applies to all ions independent of their m/q ratio. This excitation rapidly moves all ions to a larger radius of order several mm. The magnetron motion is then converted to the reduced cyclotron motion (which gets cooled away by the buffer gas) using quadrupole excitation at the frequency of ν_c. This excitation re-centers the ions whose mass and charge satisfy equation Eq.3.6. Re-centering is followed by lowering of extraction side axial potential wall. This accelerates the centered ions through a 2 mm collimating aperture to the precision trap whereas the rest of the ions that are at a radius larger than the collimator aperture, are lost. The precision trap was not used in this work. Instead, the isobarically purified ion bunch was sent directly through it to an MCP detector located downstream as shown in Fig.3.2.

The time needed to cool the ions to the center of the trap, expand them to a larger radius, re-center with the desired m/q ratio and finally extract from the trap (the purification cycle t_p), is typically a few hundreds of milliseconds. To some extent, t_p is directly proportional to the obtained mass resolution; a higher resolution can be reached with a longer purification cycle, although in some cases a successful purification can be obtained with cooling cycles as short as 70 ms [106, 107]. In order to avoid decay losses of short-lived nuclei, a short purification cycle is essential. Fortunately, the mass difference between adjacent members of an isobaric chain increases when moving further from stability and, therefore, the isobaric separation of those elements can be done sufficiently within a shorter cycle time. Closer to the line of stability, the mass difference between adjacent members of an isobar becomes smaller requiring an increased purification cycle time. This can be safely applied because the half-lives of such nuclei are also significantly longer.

An ion bunch injected to the trap is a sample of the mass separated ion beam. It was thus reasonable to measure the entire mass chain at once, resulting in the mass spectrum of a selected isobar. Due to chemical reactions that possibly occur in the ion guide and the RFQ, the measurement of a studied isotope (or isobar) was preceded and followed by the measurement of a so-called reference isotope (or isobar). A comparison between the reference and studied isotopes cancels the corrections due to chemical reactions and also provides a tool for tracing and treating possible beam fluctuations. The measurement procedures as well as effects of chemical reactions and beam fluctuations are discussed in more detail in later sections.

3.6. Measurement procedures

The method described in this work utilizes the JYFLTRAP facility to purify the isobaric beam of fission fragments, followed by ion counting. In order to measure the isotopic yield distribution, several sources of uncertainties have to be taken into account. Some of these uncertainties can be avoided in the measurement phase. For example, the significance of the chemical effects can be reduced by a correct timing procedure. A careful measurement protocol is also required to keep the intensities of mass peaks comparable with each other.

3.6.1. Effects of the trap settings

The isobaric purification method described in the previous section is capable of producing beams of single elements with a very high, of order $1 \cdot 10^5$, mass resolution. Unlike magnetic separators, however, the MRP of a Penning trap is coupled to the actual masses of the purified elements in the case, where the purification settings are constant. In other words, the width of the mass peak is a function of the trap settings and does not depend on the masses of the purified ions. Fig.3.6 shows an example of the effect of mass and trap settings on the width of the mass peaks. The experimental mass peaks of ^{89}Rb (red solid circles) and ^{141}Cs (open blue squares) were measured with the same trap settings (Settings B) resulting in peak widths (as FWHM) of 9.7 Hz and 9.0 Hz for Rb and Cs, respectively. The measurement of the same Rb isotope was also repeated with different purification settings (Settings A). The result of this measurement is indicated with the open red data points, from which the effect caused by different settings can be easily observed. The peak measured with settings A is not only much wider than that of settings B but has a different shape. In this work, the comparison between the yields of isotopes is made via mass peak intensities. In order to make this comparison easier and more reliable, it is important to keep the shapes of the compared mass peaks similar.

In addition to the peak shapes, the settings may also affect the transmission efficiency of the trap. The mass resolution of the trap is coupled to the purification cycle length as described in the previous section. A typical variable in the trap purification cycle is the cooling period. A longer cooling period provides a better centering efficiency for the ions of the desired element, improving not only the mass resolution but also the transmission efficiency of the trap. Because the effects of the timing parameters on the transmission of the trap have not been accurately studied at JYFLTRAP, any prediction is uncertain. Due to the nature of the fission reaction, the intensities of the mass separated beams are similar. In such a case, the transmission efficiency of the trap is invariant with given trap settings.

3.6.2. Chemical effects and their significance

Although the IGISOL method is stated to be chemically non-selective, this does not mean that it is fully free of reaction chemistry. Chemical effects and their significance heavily depend on the time spent in the presence of impurity atoms as well as the number of impurity atoms and their reaction coefficients. Inside the ion guide, the evacuation time of fragments is similar for each isotope of an element and changes in the impurity concentration of the buffer gas are usually very slow. Hence, with regards to chemical reactions, an equal treatment between isotopes of an element can be expected.

In addition to the ion guide, obvious places for chemical reactions to occur are the gas-filled sections of JYFLTRAP. The time that ions spend in those sections is at least 10 times longer than in the ion guide. Even though the gas pressure and number of impurities in those sections is significantly lower as compared to

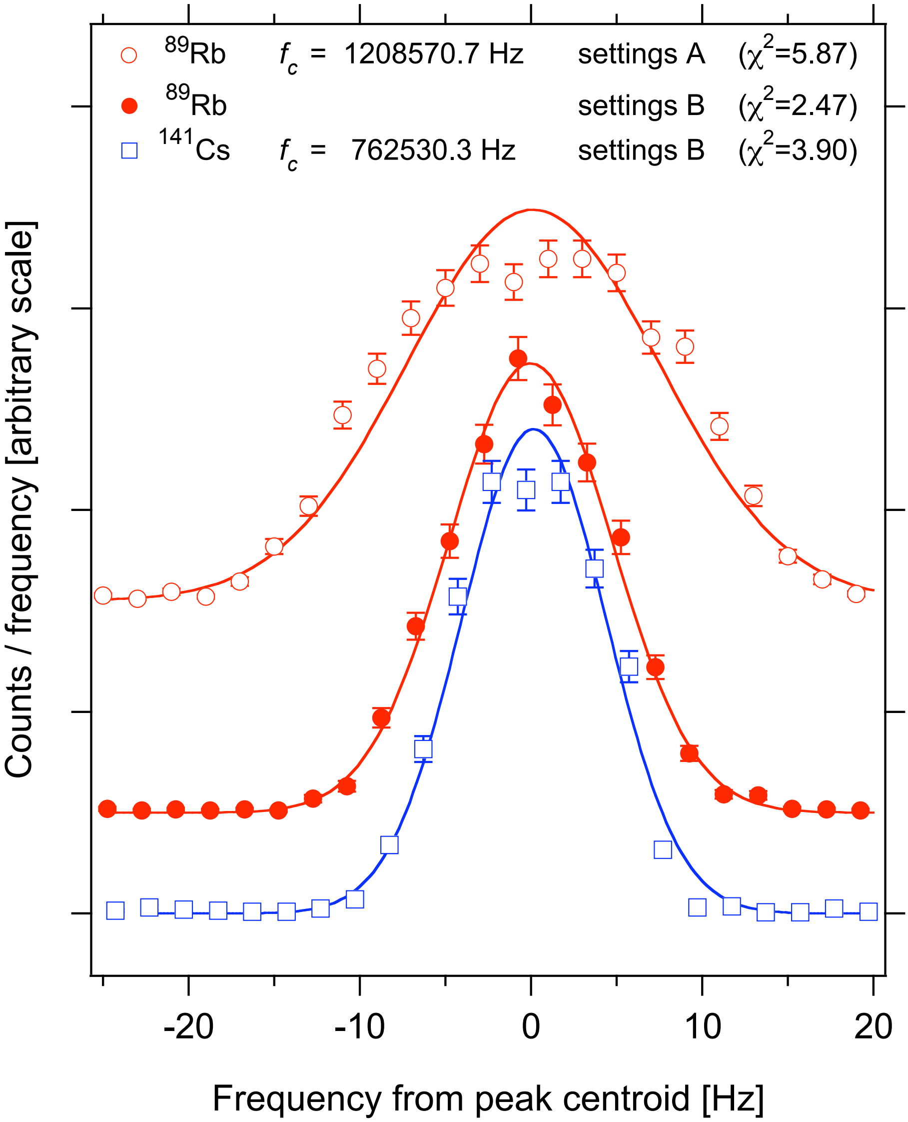

Figure 3.6.: The FWHM of ^{89}Rb and ^{141}Cs mass peaks with the same trap settings are 9.7 ± 0.3 Hz and 9.0 ± 0.3 Hz, respectively, deduced from Gaussian fits (solid lines). The mass peak of ^{89}Rb measured with different trap settings is also shown in order to indicate the effect of the settings. The resulting peak is not only wider, 16.9 ± 0.5 Hz, but also the shape is different. The error bars on the data points include the statistical uncertainties.

the ion guide, reactive elements such as Zr and Y, have time to produce molecules during the purification process. An example of molecular formation in the RFQ occurred during the first atomic mass measurements of neutron rich Zr isotopes performed with JYFLTRAP [108]. As the ZrO^+ yield was so much higher than that of pure Zr ions, the atomic mass of Zr was deduced from the masses of the molecular ions. Depending on the amount of free radicals and on the exposure time, chemical reactions can occur with almost all known elements. From the point of view of this work, the most problematic chemical issues were mainly related to the elements in chemical groups IIIA and IVA which, when combined with free oxygen radicals, are able to form very stable monoxide ions within very fast time scales.

A second considerable chemical reaction type is a charge exchange reaction between the ion and the impurity atom of the buffer gas. This reaction type typically affects elements that have a high first ionization potential such as Kr and Xe. Weakly bound electrons of the impurity atoms can be easily captured by the ions of these elements, leading to a rapid neutralization of the capturing ions. In this work, the abundance of purified ^{87}Kr ions was unexpectedly small compared to those of the adjacent isotopes (see Fig.3.8). The problem was traced to an air leak in the RFQ after the same $A = 87$ beam had been studied via β-delayed γ-spectroscopy at the central line of the IGISOL and ^{87}Kr turned out to be as abundant as the adjacent isotopes ^{87}Rb and ^{87}Br.

The IGISOL front-end has been designed to meet the requirements of a high vacuum (HV) system and the residual gas pressure in this section is typically about 10^{-6} mbar. The only exception is the target chamber, in which the ion guide is located. Due to a relatively high gas load used in on-line conditions, the volume of this chamber is pumped with mechanical booster pumps, having an ability to reach a residual pressure of order of 10^{-4} mbar without any gas load. Even though the pressure is much worse than in other parts of the IGISOL, it is still sufficient to avoid most chemical reactions.

The vacuum system of JYFLTRAP meets the requirements of the ultra-high vacuum (UHV) standard. Without any gas load, a pressure level of 10^{-8} mbar can be easily reached. Therefore, a major source of impurities present in the vacuum system is formed by impurities of the buffer gas (99.99990 % He). The buffer gas used in the RFQ and the TRAP is fed to the vacuum system without any additional purification. Air leaks, such as mentioned above, are very rare in the JYFLTRAP vacuum system. These leaks are usually related to the connections between gas feeding lines and bottles, which do not necessarily fulfill the HV or UHV standards.

Since the presence of the buffer gas is essential for the operations of both the RFQ and JYFLTRAP and as the accumulation times of the ions in these devices have to be relatively long, chemical effects cannot be fully avoided. The chemical reaction rates depend on the element and hence, many elements have different transport efficiencies. This is a clear drawback for the proposed yield method, since it prevents the determination of an absolute independent yield distribution of fission products. Nevertheless, the chemical properties of the isotopes belonging to the same element are similar. Hence, if the studies are limited to the isotopic fission yield distributions the correction factors (see Eq.3.12) due to the chemical reactions possibly occurring in the ion guide or in other gas-filled sections of the facility cancel out. Of course, the cancellation is valid only if the exposure of the measured isotopes to the impurities is the same and therefore equal cycle lengths must be used in isotopic yield measurements.

3.6.3. The timing of purification and collection of the data

A schematic of the timing used in all experiments of this work is shown in Fig.3.7. The preparation cycle time (t_c) was matched to the purification cycle time t_p in such a way that a new bunch was prepared in the RFQ while the preceding bunch was being purified in the trap. These simultaneously executed cycles typically cuts in half the time required for the experiments as compared to sequential cooling and purification. The previously mentioned beam kicker cycle t_b was applied, if needed, at the beginning of a cooling cycle to block the ions from entering the RFQ. This "effective" reduction of the cooling cycle was done in order to adjust the charge density in the RFQ and to prevent space charge effects. The t_b cycle was also used to minimize decay losses of short-lived isotopes. In order to keep the counting rate of these isotopes at a reasonable level, the yield loss due to the shorter cooling cycle was compensated by increasing the intensity of the primary beam from the cyclotron.

For each isobaric chain, the cyclotron frequency f_c was scanned over the mass region of interest. This scan is hereafter called a frequency scan, which contains one ion bunch per scanned frequency. The events detected by the MCP detector were stored to a data file together with the corresponding frequency value. Time-of-flight (TOF) information, starting from the moment when the ion bunch was released from the purification trap and ending at the moment when the ions were detected, was also recorded and stored to the data file. The frequency scan was then repeated as many times as required for adequate statistics. The number of frequency scans varied between 11 and 401, 50 scans being the most typical value.

Fig.3.8 is an example of a scanned mass spectrum. The typical measurement time for an isobar is 30 minutes and hence the time gap between the first and the last isotope of the element of interest may well be several hours. This time gap is so long that possible yield fluctuations and changes in the buffer gas impurity

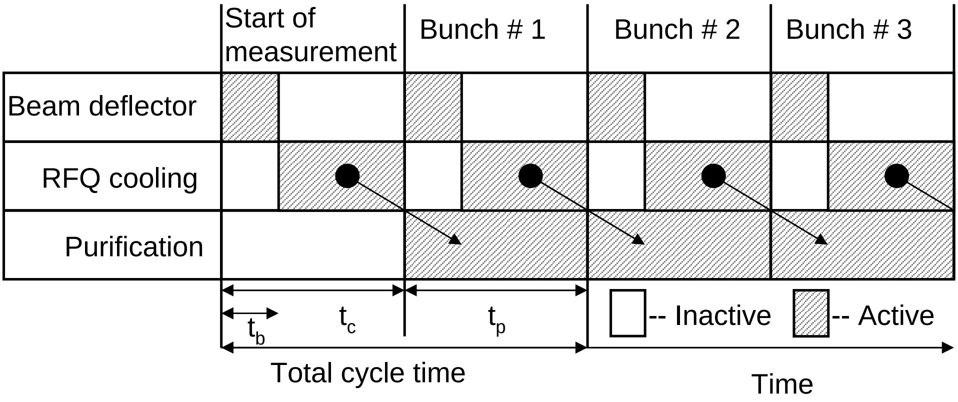

Figure 3.7.: JYFLTRAP timing diagram used in the experiments of this work. At the beginning of the measurement the trap is empty and ions are prepared for purification by the RFQ. After the preparation cycle (t_c), the ion bunch is sent to the trap for the purification cycle (t_p) and a new preparation cycle for the next bunch is initialized. The beam kicker cycle (t_b) was used to block the ion beam in order to reduce the ion count in such cases in which a possible space charge effect may occur.

concentration cannot be ignored. Therefore, each measured isobar was preceded and followed by a measurement of a so-called reference isobar. By comparing the yield of the measured isotope to that of the reference isotope of the same element, possible errors due to long term yield and impurity fluctuations can be traced and, in most cases, eliminated.

3.7. Data analysis

The analysis of the mass purified data contains many steps, for example spectra generation, data rejection, mass peak analysis and possible radioactive decay corrections. Before the yield distributions can be reliably extracted from the measured data, many checks need to be done. These are mainly related to the mass dependence of the transmission efficiency through the facility, possible yield fluctuations during the measurements and pile-up and ion bunch intensity limitations, among others. All these issues are handled in more detail in separate subsections.

3.7.1. Generating spectra from the data

Each recorded event contains information about the scanning frequency, TOF and the number of detected ions. It is thus possible to extract TOF and mass spectra directly from the recorded data. Because the frequency scan order is also known, a time history spectra of the detected ions can be generated by sorting the recorded data.

The mass difference of the measured isotopes within any given isobar A is less than a few tens of MeV/c^2, whereas their mass is of order 100 GeV/c^2. Since the mass difference is always less than a per mille, the ions TOF from the trap to the MCP is similar and forms a peak that is clearly distinguishable in the TOF spectrum as can be observed from panel (a) of Fig.3.8. The TOF peak of purified ions typically appears at values between 300 and 500 bins, which corresponds to a time scale of 200 - 300 μs. In addition to this TOF peak, some other peaks as well as randomly distributed single events may appear in the TOF spectrum as can be observed from panel (a). The random single events mostly stem from the noise and false triggering of the MCP detector but the peaks are probably due to real ions generated by discharge sparks of JYFLTRAP. Such peaks do not, however, carry any significant information about the measured elements and thus they can be counted as a background noise.

The detected events, when plotted as a function of the scanning frequency, form a mass spectrum. The raw mass spectrum of the $A = 87$ elements is shown in panel

(b) of Fig.3.8. Due to a relatively high background noise level the raw spectrum resolution usually looks rather poor. Although the mass peaks of Se, Br, and Rb isotopes are already visible in the example case, the peak of Kr is totally buried in the background. By gating the mass spectrum with the expected TOF window of the purified ions (shaded area in panel (a)), the level of background reduces almost to zero. As can be observed from panel (c), the peak of ^{87}Kr clearly appears in the gated mass spectrum. The mass spectrum gated outside the expected TOF window is shown in panel (d). All that is left in the spectrum is a constant background without any signs of the mass peaks. This indicates the validity of the TOF gate selection.

Since the frequency scan protocol is precisely known, the recorded data can be sorted according to the recording time. The result of this operation is the time history spectrum of the measurement, which provides information about the yield evolution. The time histories can be generated for a single mass peak or for the entire mass spectrum. As will be discussed later, the time histories are very important for later analyses.

An example of the time history of $A = 87$ measurement is shown in Fig.3.9. The recorded ion count as a function of the time for the entire mass spectrum is shown in the top panel while the separately generated time histories for the mass peaks of Se, Br and Rb are shown in the lower panels. Within an hour, the overall yield has increased from about 200 counts/scan to over 300 counts/scan. The blue solid line in the top panel is an interpolation through the data points illustrating the trend of the time evolution. The blue lines in the lower panels in turn represent the trend of the top panel, now scaled with the sizes of the corresponding mass peaks. A good agreement between the latter blue lines and the recorded single element spectra clearly indicates that the yield fluctuations observed in this case are similar for each element.

3.7.2. Rejection of the bunches

The TOF gate is a very powerful tool for background reduction. Unfortunately, only those background events that appear outside the TOF window can be eliminated. For this reason, some background may still appear in the gated mass spectrum as can be observed from panel (c) of Fig.3.8. This background is mainly formed from random noise which, due to its low intensity, is quite harmless. Some fraction of the background events may however stem from the high voltage discharges of the trap facility. The corresponding noise bursts may be very harmful, especially when they exist near to frequencies that correspond to mass peaks of ions far from stability. The expected intensities of those mass peaks are naturally low, containing just a few

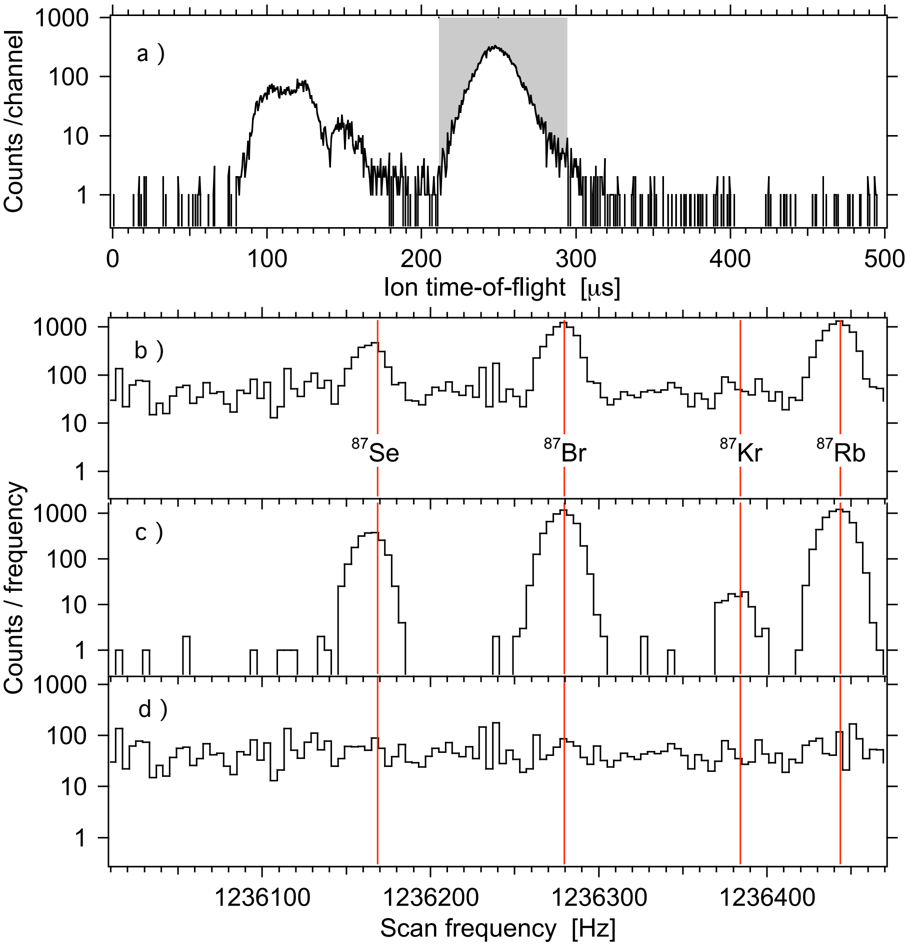

Figure 3.8.: The raw mass spectrum of $A = 87$ ions and the background reduction by TOF gating. The cyclotron frequencies corresponding to the mass of each isobar are indicated by labeled vertical lines. See text for more details.

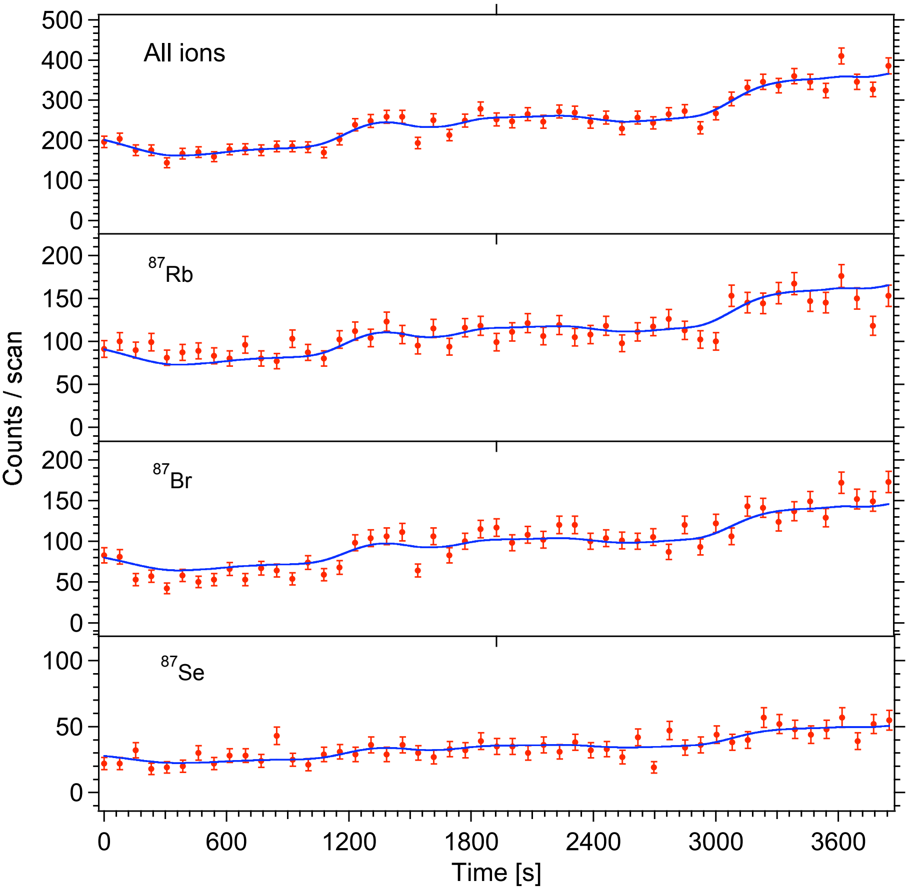

Figure 3.9.: Time history spectra of $A = 87$ measurement. See text for more details.

ions at maximum and, in addition, frequencies of those masses may differ several hundreds of keV/c^2 from the values given in literature [109, 110]. One example of such a situation in this work was the "mass peak" which was preliminary associated to ^{106}Zr. This peak was, however, later eliminated by the statistical analysis of time history spectra.

The time history spectrum of the single frequency (1120412 Hz) of mass $A = 96$ is shown in the inset of Fig.3.10. The detected count per bunch varies from 0 to 6 ions within statistical limits until the 49^{th} scan, which contains 24 ions. In stable conditions, only the statistical variation of the count rate is expected. Therefore, the observed ion count, N, of a scan is assumed to follow a Poissonian distribution [111]. According to this distribution, the expectation value for the number of scans that have at least n ions, weighted by the size of the dataset, can be estimated as

$$E(N \geq n) = k \cdot \sum_{i=n}^{\infty} \frac{e^{-\theta}\theta^{i}}{i!} \tag{3.7}$$

where k is the size of the dataset, which in this case is the number of scans. The Poisson distribution parameter θ is the mean of N over the entire dataset, $\theta = \bar{N}$. The time history spectrum of a single frequency can be used for a statistical analysis, however, it is more useful to convert these histories to histograms, from which the structure of the distribution can be easily observed. The calculated histogram of N for the single frequency time history given in the inset of Fig.3.10 is shown in the main panel of the same figure. The Poisson distribution parameter θ, calculated with the anomalous scan with $N = 24$, is 2.69 and the total number of scans k is 51 for this case. With these parameters, the expectation value of $E(N \geq 24) \approx 1.3 \cdot 10^{-13}$ for $N = 24$, strongly supports the elimination of scan 49 from further analysis.

The calculated Poisson distributions for the data given in the inset of Fig.3.10 with and without the anomalous scan are illustrated as solid and dashed curves, respectively. The dashed curve provides better agreement with the data, which indicates that the rejection of the bunch was justified in this case. Traditionally, Chauvenet's criterion for data rejection states that any data point having at least n counts should be rejected if $E(N \geq n) < 0.5$ [111]. This criterion can be used as a rule for the automatic detection of anomalous bunches.

On the other hand, the data point rejection based on the Poisson distribution and Chauvenet's criterion is valid only for the data measured with good statistics and in stable conditions. The yield fluctuations, such as shown in Fig.3.9, modify the structure of the measured bunch size distribution and therefore the basic assumption of a Poisson-like distribution is not valid anymore. In addition, for the measurements in which the number of scans k is small the statistical uncertainty of the Poisson

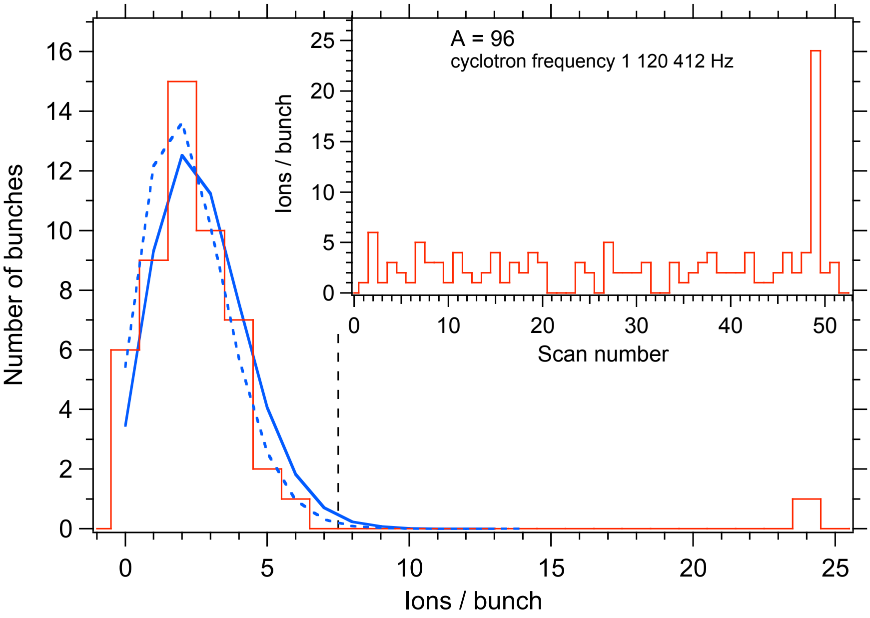

Figure 3.10.: A histogram of the bunch size distribution generated from the time history of a single frequency. The inset shows the time history of the detected ion bunches at this frequency. Poisson distributions with and without the anomalous scan #49 are illustrated as solid and dashed curves, respectively. The bunch size, in which the traditional Chauvenet's limit for data rejection is located, is indicated as the vertical dashed line.

distribution parameter θ becomes large:

$$\Delta\theta = \sqrt{\frac{\bar{N}}{k-1}}. \tag{3.8}$$

Since the expectation value $E(N \geq n)$ depends on this parameter, the uncertainty of the expectation value may become so large that Chauvenet's limit cannot be fixed to a certain bunch size. For example, a dataset contains 11 samples whose mean, θ, equals 10. By taking into account the uncertainty introduced by Eq.3.8, the actual θ can have a value between 9 and 11 ($\Delta\theta = \pm 1$). According to Eq.3.7, the expectation value for the case of $N \geq 15$ is ~0.44 when $\theta = 9$ is used, indicating that the bunch should be rejected. On the other hand, if the same case was calculated with $\theta = 11$, the result of $N \geq 15$ would be ~1.65, now indicating that the bunch should not be rejected. For this particular example, the similar incongruity of the bunch rejection continues up to the expectation value of case $N \geq 17$. Starting from the case of $E(N \geq 18)$, the rejection decision always results within the error margins of θ.

Nevertheless, a computerized algorithm based on the Poisson distribution and Chauvenet's criterion proved to be sufficient to find the most anomalous cases from the data. In general, less than 10 bunches per measurement were typically identified as a noise burst and rejected. By taking into account that the count of bunches per measurement varied from 500 to 40000, problems associated with noise bursts were not very common.

3.7.3. Determination of mass peak intensity

The goal of this work was to deduce the yields of isotopes produced in fission in such a way that the intensities of the isotopes of the same element can be reliably compared to each other. The peaks in the mass spectrum can be used to indicate such intensities. The maximum transmission through the purification trap is reached when the cyclotron frequency of the studied element given by Eq.?? is satisfied.

Counts-in-peak method

Since the maximum of the transmission efficiency is reached at the cyclotron frequency, the height of the mass peak is a direct measure of the beam intensity. One way to determine the height of the peak is to fit an appropriate mathematical function as is commonly done in a decay spectroscopy experiment. It is worth recalling, however, that the shape of the mass peak is not a uniform quantity in the case of Penning trap spectrometers but it is mainly defined by the centering efficiency of the quadrupole excitation as discussed in Section 3.6.1. In addition, a fitting quality parameter, the reduced χ^2, reveals that none of the peak shapes shown in Fig.3.6 fully coincide with the true Gaussian shape. If more complicated functions would be used to provide better compatibility with the experimental data, they should be determined separately for every trap settings used. Therefore, the peak height is not the best solution for the determination of the beam intensity in this work.

As can be observed in Fig.3.11, the shape of the mass peak is similar for all measurements that have been realized with the same settings. Since both the shape and the width of the mass peak are invariant for a given settings, the peak area and height have to be equivalent measures of the beam intensity. It is therefore appropriate to determine the number of counts in the peak. In general, use of this method is often hindered by the background of the studied spectrum. In this work, however, the background can be significantly reduced by the TOF gating and usually no separate background estimations are needed. A more serious limitation for this method is caused by peak multiplets. Without detailed knowledge of the peak shape, only the intensities of clearly separated mass peaks can be approximated correctly. Peak multiplets are typically caused by close-lying isomeric states of isotopes or adjacent members of isobars located close to stability. In the fission yield distributions, the yields of isomeric and ground states are often summed together. If the half-lives of close-lying isomeric states are similar such that there is no need for separate decay corrections, the peak multiplets can be usually treated as one peak. Excluding isomeric states, only about 30 of 294 mass peaks measured in this work overlapped with another peak. The intensities of these multiplets cannot be deduced by the "counts-in-peak" method.

It is clear that the uncertainty of the "counts-in-peak" estimation depends on the number of data points within the peak area as well as their location with respect to the actual centroid of the peak. Sometimes the center of the mass peak coincides with a certain data point but usually it falls between two measured points as illustrated in the left panel of Fig.3.12. The influence of the sample points location on the accuracy of the "counts-in-peak" method is illustrated in the right panel of Fig.3.12, in which the relative peak area variation as a function of the sampling interval (given as the FWHM of each peak) has been studied by using several experimentally observed peak shapes. In addition to the experimental shapes, the variation of the symmetric Gaussian shape is also shown as a reference.

The experimental peak shape is determined from a smooth interpolation through the data points, as shown by the solid line in the left panel of Fig.3.12. The number of counts that would be obtained at a certain frequency can then be deduced from this peak shape. The peak intensity obtained by the "counts-in-peak" method with a certain sampling frequency can be deduced by summing over the frequencies of the

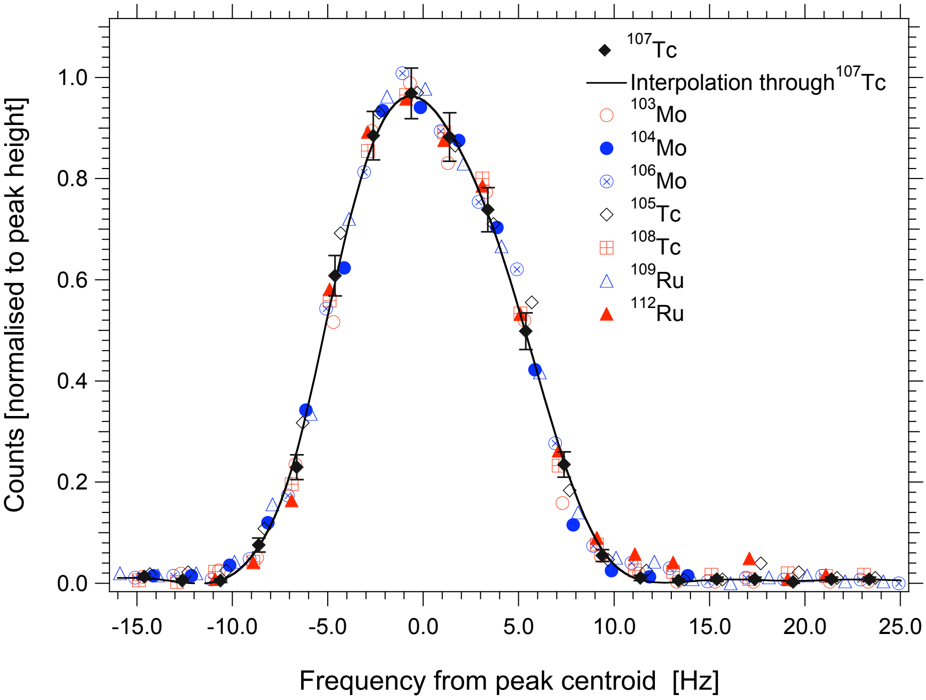

Figure 3.11.: The normalized mass peak shapes of Mo, Tc and Ru isotopes produced with the same Penning trap settings. The solid line shows a linear interpolation through the data points of ^{107}Tc, of whose error bars are representative for all data points.

mass peak. The dependency of this peak intensity on the location of the sampling frequencies (the red solid points) was studied by changing the sampling frequency in small steps over the mass peak. The uncertainty of the peak intensity for a given frequency step is obtained from the difference of the largest and smallest ion count in the peak. In the right panel of Fig.3.12, this uncertainty analysis is repeated for different frequency steps.

Due to the symmetry of the Gaussian shape, the relative peak area variation decreases rapidly and smoothly as the sampling interval is made smaller. In the other cases, the variations of the peak areas are reduced more gradually and surprisingly large fluctuations are observed. However, a variation below 1 % is reached with a sampling interval smaller than 0.4×FWHM in each case. Since the actual width of the peak is usually about 2×FWHM, at least 6 data points are required to suppress the uncertainty to an insignificant level. This requirement was always fulfilled in the experiments of this work.

Resolving peak multiplets

In order to resolve multiple peaks from each other, an accurate peak shape is required. Though a Gaussian shape does not fully reproduce the mass peaks, it was considered to be sufficient for the determination of overlapping peak areas in this work.

The reliability of the Gaussian fit for multiple peak determination was studied with a virtual spectrum. This spectrum was formed from two experimentally measured and well separated single mass peaks that were almost reproducible with a Gaussian shape of FWHM 10 Hz. It was also possible to determine the positions and heights of the selected mass peaks very precisely. The frequency axis of the virtual spectrum was modified in such a way that these peaks started to overlap. This multiplet was then resolved with a multiple peak analyzing algorithm. It was determined that when two mass peaks of equal size are located closer than 4 Hz, a 10 % deviation between the fitted and known peak parameters is exceeded. This discrepancy starts to be significant and therefore at least 0.4×FWHM separation between the peaks is required for equal sized overlapping mass peaks. Indeed, this separation seems to be sufficient as long as the height of the smaller peak is at least 40 % of that of the larger peak. If the intensity difference is larger, more separation between the peaks is needed in order to maintain a reasonable accuracy.

In Fig.3.13, mass peaks of ^{120}Cd and ^{120}In have been resolved from each other by an unweighted Gaussian fit. The separation between the two peaks is about 15 Hz, which should be sufficient to produce accurate fits. The only requirement for the fitting process was an equal width for all peaks. The resulting common width

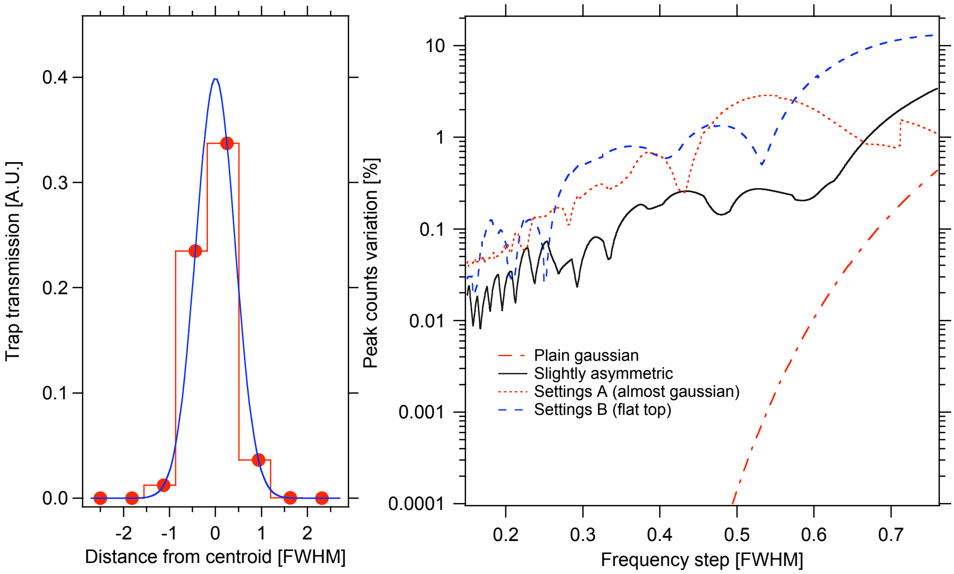

Figure 3.12.: The variation of peak areas corresponding to different experimental peak shapes. An example of a dataset (histogram) that matches a Gaussian-shaped peak (blue line) is shown in the left panel. The maximum relative variations of peak areas as a function of the peak sampling interval for various experimental peak shapes are shown in the right panel. Settings A and B refer to the peaks shown in Fig.3.6, slightly asymmetric corresponds to the peak shape shown in Fig.3.11 and plain Gaussian has been illustrated in the left panel. In order to keep the results comparable, the sampling interval is presented as a FWHM for each peak shape.

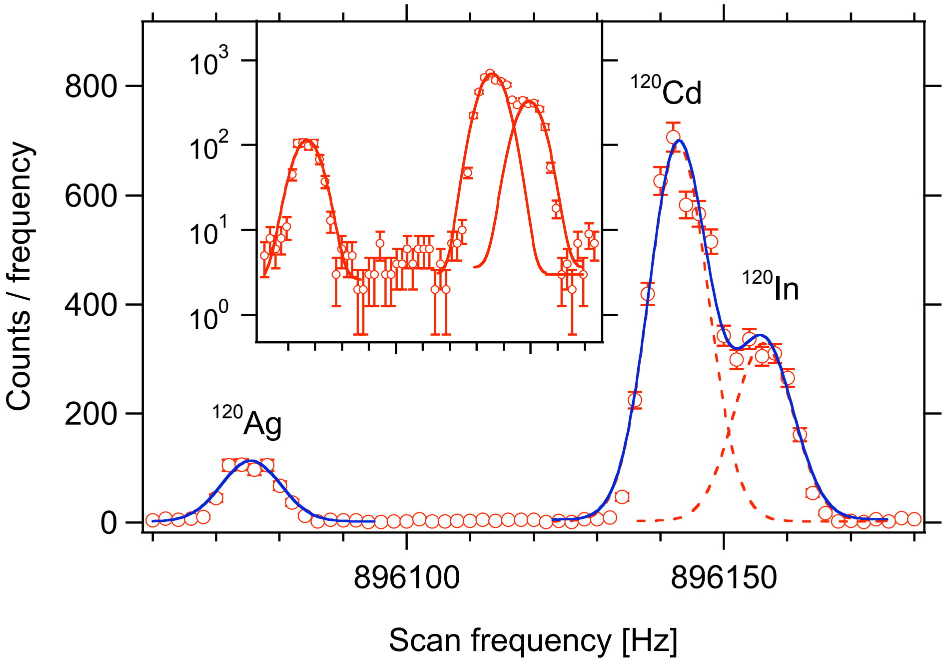

Figure 3.13.: Mass peaks of ^{120}Cd and ^{120}In resolved from each other by unweighted Gaussian fits. The FWHM of the fitted peaks is 11.0 ± 0.3 Hz and the separation between the peaks is about 15 Hz. The inset shows the separately fitted peaks in a logarithmic scale.

(FWHM) of the peaks is 11.0 ± 0.3 Hz, similar to the widths of well separated single mass peaks observed in an $A = 119$ spectrum. In general, overlapping peaks mainly occur between two adjacent elements located close to stability due to their small mass difference. The masses of such elements are often precisely known and hence the fits of those peaks can be improved, if necessary, by constraining the peak positions. The uncertainties of the fitting results were used as uncertainties of the deduced peak intensities.

3.7.4. Irresolvable mass peaks

The yield data contains some overlapping mass peaks located so close to each other that they cannot be resolved by a fit. Those peaks either belong to adjacent elements close to stability or to close-lying isomers of the same element with clearly different half-lives. Adjacent isotopes located close to β-stability tend to form multiplets due to their small mass differences. Those isotopes are so long-lived that the radioactive decay correction (see the next section) is not significant and therefore the sum of the yields is known from the total intensity of the multiplet. The yields of the isotopes in the multiplet can be estimated using interpolation and extrapolation from the yields of other isotopes of the same element.

For such isomers whose decay losses are significant and for isomers whose half-lives clearly differ from each other, the "counts-in-peak" method cannot be applied. According to the NuDat2 database [66], there are 64 known irresolvable isomeric multiplets among the 294 isotopes measured in this work. The half-lives of 23 isomers are sufficiently different to result in a decay correction higher than 5 % between the isomeric states.

Fig.3.14 shows an example of such a problematic isotope. ^{120}Ag, whose isomeric state is located 203 keV above the ground state [112], decays to excited states of ^{120}Cd via β^- decays of both the ground and the isomeric states. The half-lives of the ground and the isomeric states are 1.23 ± 0.03 s and 0.32 ± 0.04 s, respectively. The decay correction needed for ^{120m}Ag is about three times higher than for ^{120}Ag and hence the isomeric production ratio is required before the total yield can be properly deduced. Some isomeric production ratios have been experimentally studied and the results can be used in the estimation of the overall yield of those isotopes. For example, isomeric production ratios for 30 isotopes in 24 MeV proton-induced fission are reported in [113]. Unfortunately, these results do not include the ratios for ^{120m}Ag and ^{120}Ag. Since experimental information is unavailable for this case, the only option is to use theoretical models. One possible candidate is the statistical model of Madland and England [114], which is commonly used in many fission yield-related isomeric state population calculations. According to the model, the populations of the isomeric and ground states are spin dependent and, in this particular case, the population of the 6^- isomeric state and the 3^+ ground state are expected to be roughly equal. This model was, however, claimed to be inaccurate for 24 MeV proton-induced fission of ^{238}U in [113]. If the spins and parities of the isomers are not known, the only option is to assume an equal production for each isomer. The uncertainty is then calculated from the upper and lower limits of the decay correction, which in turn is calculated from the extreme case in which only one isomer is assumed to be produced.

In addition to the radioactive β-decay of the isomer, it can also decay directly to the ground state. In the example case of ^{120m}Ag, the branching ratio of this internal transition is 37 % as shown in Fig.3.14. When this internal transition occurs via γ-emission, the isomeric state has a certain chance to be observed as the ground state of ^{120}Ag. In addition to the γ-emission, internal decay may also occur via electron emission. For the 203 keV isomeric state of ^{120}Ag, the internal conversion coefficient is 0.60, which means that about 37 % of the internal transition occurs via electron emission, resulting in a $^{120}\mathrm{Ag}^{2+}$ ion. Since the trap is tuned for singly charged ions only, these ions will be lost in the purification phase. For the other 63 % of the internal transition, however, the charge state of the resultant ions remains as 1^+ and these ions contribute to the observed mass peak of ^{120}Ag. The total fraction of the contributing ions is as high as 23 %, which is too significant to be ignored. At this development phase of the method, these effects are only described yet have been left uncorrected.

3.7.5. Corrections due to radioactivity

The time from the moment of ion creation to the moment of detection is typically several 100 ms. This time is long enough for radioactive decays to occur especially for short-lived elements. Since over 90 % of this time is spent in the RFQ or the trap, these apparatuses are the most favorable locations for decay losses. There are three methods in which the radioactive decay can affect the measurements: the release of β-decay daughters from the surfaces of the IGISOL front-end, a β-decay recoil captured by the trap and the decay losses due to the radioactive decays of short-lived isotopes.

The release of β-decay products

The efficiency of the JYFL fission reaction is deduced to be ~0.01%, which means that only one out of 10^4 fission fragments can be extracted from the ion guide as a 1^+ ion. In other words, 99.99 % of fission products are lost somewhere inside the ion

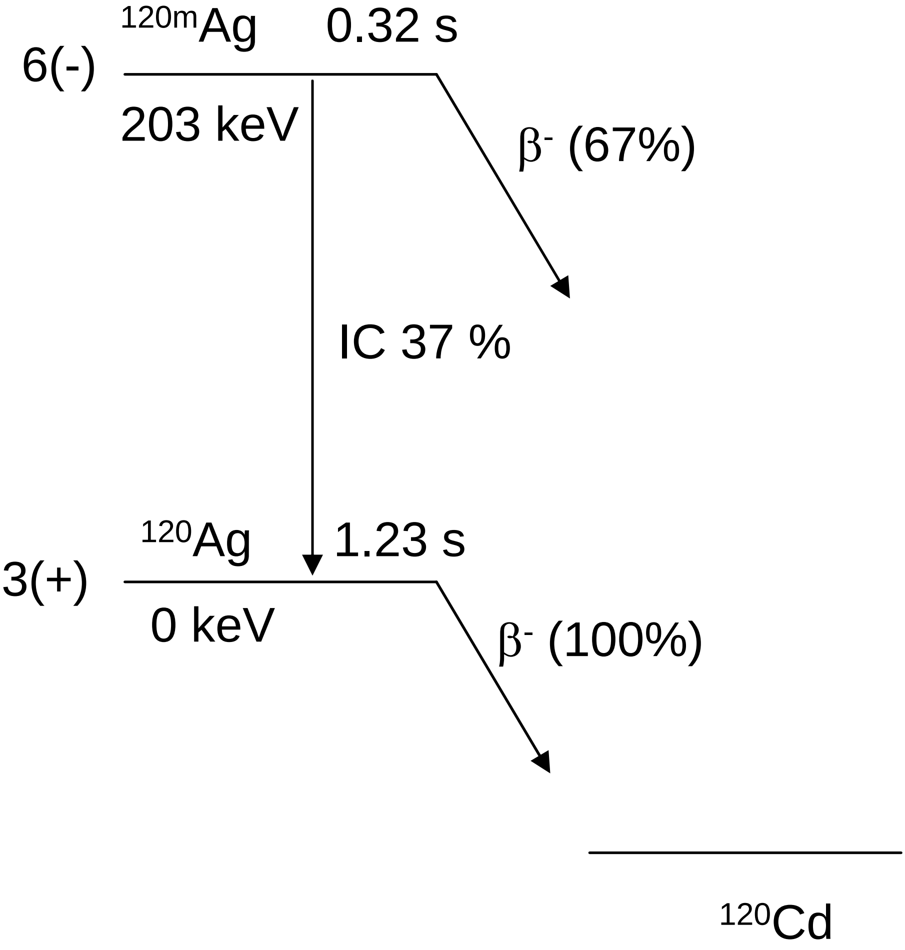

Figure 3.14.: A simplified decay scheme of ^{120}Ag to excited states of ^{120}Cd. ^{120}Ag has two β^--decaying states: A 3^+ ground state and a 6^- isomeric state. In addition to β-decay, the isomeric state can also de-excite to the ground state via an internal transition, which in turn occurs either by a γ-transition (63 %) or by an electron emission (37 %).

guide or are extracted as neutral or multiple charged ions. Due to the kinematics of β-decay, most of the energy released from the reaction is shared between the light particles (electron and neutrino in β^--decay) emitted from the mother nucleus. A small amount of energy is, however, converted into kinetic energy for the daughter nucleus. This is often called as the recoil energy of the decay and it provides the daughter nucleus with a small "kick". For some energetic β-decays, this recoil kick may be strong enough to release the daughter back into the gas phase of the ion guide. This may cause skewing of the yield distributions, since the recoil energies differ even for isotopes of the same element. The maximum recoil energies due to β-decays are usually very small, a few tens of eV. In practice this means that only those fission products that have been thermalized by the buffer gas and have stuck to the wall of the ion guide are able to participate in this process. The energies of the non-thermalized products are usually so high that the recoil kick is not sufficient to release the daughter from the wall material.

In addition to the walls of the ion guide, the daughter nucleus may be released by the recoil kick from the surfaces of the SPIG electrodes. Indeed, this phenomenon has been observed in connection with the LIST test performed in [29], in which relatively weak selectivity of the laser ionization for some fission produced isotopes was observed. After further study, it was observed that the neutral radioactive isotopes weakly stuck to the rods of the SPIG system. The β^- decay recoil energies of some daughter nuclei are sufficiently high that they are able to return to the gas phase of the SPIG. Due to relatively high, $\sim$1 mbar, buffer gas pressure inside the SPIG, some of those daughters were then stopped and captured by the rf field. Because these decays took place after the repulsive electric field used in the LIST mode, the daughters were able to pass the SPIG system, greatly hindering the selectivity of the laser ionization process.

A short test to study this phenomenon was performed in connection with recent yield measurements of isotopes produced in 25 MeV proton-induced fission of ^{232}Th. The test was realized by monitoring the yields of ^{96}Sr and ^{96}Y isotopes while tuning the cyclotron beam on and off in $\sim$10 s periods. During the 'beam-on' period, the saturation of ^{96}Rb ($T_{1/2}$ = 203±3 ms) and ^{96}Sr ($T_{1/2}$ = 1.07±0.01 s) production was reached. The decay products of ^{96}Rb and ^{96}Sr were then monitored by scanning a certain frequency, located at the centroid of the mass peak of the corresponding isotope, during the 'beam-off' period. The mass scan over ^{96}Sr and ^{96}Y is shown in Fig.3.16. ^{96}Y ($T_{1/2}$ = 5.34±0.05 s) has an 8^+ isomeric state ($T_{1/2}$ = 9.6±0.2 s) produced only in fission. A 0^- ground state, also produced in fission, is additionally fed by the decays of ^{96}Sr nuclei.

The possible release of daughter nuclei should be seen as a tail in the time history spectrum after the cyclotron beam is turned off. This tail is clearly visible for the ground state of ^{96}Y as can be observed from Fig.3.15. The absence of a tail of the isomeric state hints that the observed ground state tail must have been caused by the decay products of ^{96}Sr nuclei stuck somewhere in the gas cell or SPIG. A tail was not observed for ^{96}Sr either. The mother of ^{96}Sr, ^{96}Rb, is rather exotic and thus significantly less produced in fission. Moreover, the half-life of ^{96}Rb is too short for its daughters to be clearly observed with the selected purification cycle of 431 ms.

The inset of Fig.3.15 shows the tail of the ^{96}Y ground state after turning off the cyclotron beam, now with improved statistics. A first order exponential fit to the data (the red curve) results in a half-life of 1.18 ± 0.14 s, which agrees with that of ^{96}Sr. The two first data points are excluded from the fit since they contain ions that were produced in fission. The first data point after the vertical dashed line of the main figure panel contains ions that were in the RFQ at the moment when the cyclotron beam was turned off. A fit to the tail, such as that shown in the inset of Fig.3.15, also returns an estimation for the number of recoil daughter nuclei that would have been observed without the pulsing of the cyclotron. For the case shown in the main panel of the figure, this number represents about 1% of those nuclei that were observed with the cyclotron beam, which is not very significant. Moreover, it is also worth noting, that the estimation calculated above is not absolute. It is likely that the SPIG transmission efficiency is notably better when the cyclotron beam is turned off and the space charge effect is less or even completely insignificant. Therefore, this test provides only a maximum magnitude for the effect. In order to minimize this effect, the location of the release of the daughter needs to be identified. This will be studied in the future using pulsing of both the repeller and end electrode voltage of the SPIG.

β-recoil capture by the trap

As discussed in [115], it is possible that the decay products of the β-decays inside the trap may also become trapped and purified. This means that observed abundances of less exotic isotopes may be distorted by the decays of more exotic isotopes. Due to the nature and distribution of the isotopes produced in fission reactions, this cannot, however, be a very significant problem. Within a short, of order sub second purification cycle, only the most exotic elements can affect the abundances of the less exotic neighbors. Fission cross sections decrease rapidly towards the more exotic isotopes; about a factor of ten per mass unit. Therefore, the produced yield of an exotic element is already much smaller than that of its daughter and even if all decay products were trapped, this would mean an enhancement of only $\sim$10 % in the observed yield of the daughter element. Another possibility is the decay of

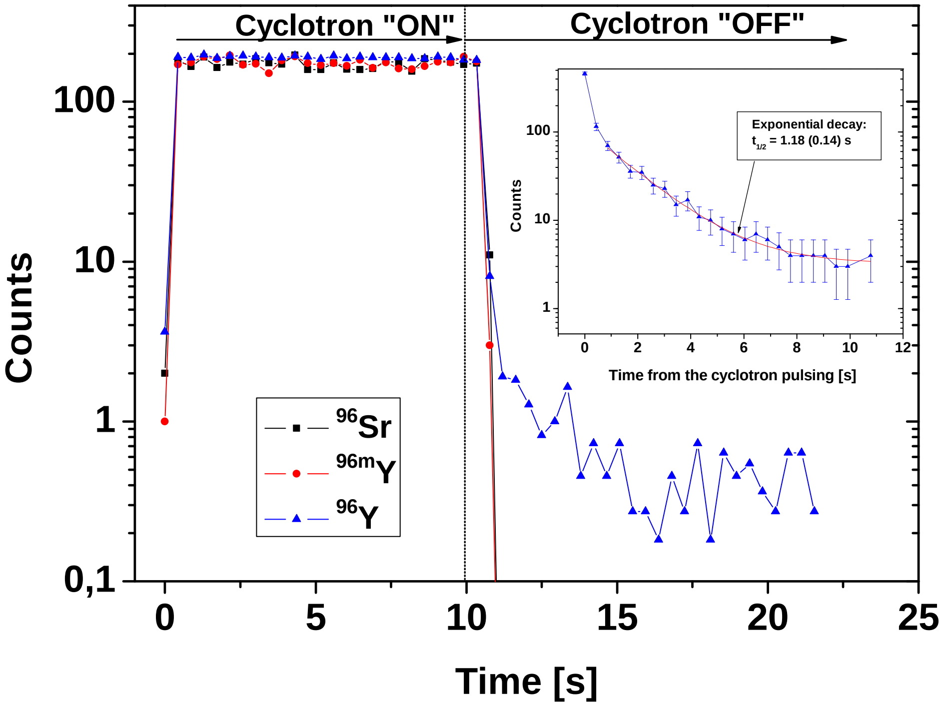

Figure 3.15.: The main panel shows the observed time histories for ^{96}Sr and ^{96}Y isotopes when the cyclotron beam was pulsed. The time when the cyclotron beam was turned off is indicated by the dashed vertical line. The inset shows the observed tail (with improved statistics) of the ^{96}Y ground state. A first order exponential decay fit to the tail reveals that the decay constant is equivalent to that of the ^{96}Sr isotope.

the most abundantly produced isotope to the less abundant, more stable isotope. However, the life times of those isotopes are so long, typically a few seconds or more, that the fractions of their decay products possibly contributing to the abundances of daughter nuclides are mostly insignificant.

Due to the nature of the fission reaction, only neutron rich isotopes are produced. Therefore, even if a daughter nuclide would become trapped following decay, it would be probably lost in the purification phase due to the different charge state. After β^--decay, a singly-charged parent nuclide always becomes at least the doubly-charged daughter nuclide. In addition to this, some fraction of β-decays are often followed by an additional shake off of electrons. As shown, for example, in the studies of charge state distributions of ^{85}Kr and ^{133}Xe - ^{133}Cs, about 20 % of β^--decays was followed by the additional loss of one or more electrons [116, 117]. If the purification trap is tuned to pass only singly-charged ions, purification of the decay products depends on how rapidly multiply-charged daughter nuclides can reset themselves as singly-charged ions. On the other hand, even if the multiply-charged ions could pass through the purification process, the TOF would be significantly shorter compared to that of singly-charged ions and hence they would be eliminated by the TOF gate at the latest in the analysis phase.

In light of the details discussed above, it seems very improbable to detect any daughter nuclei from β^--decays. However, an attempt was made to study this phenomenon using JYFLTRAP. Since a short-lived β^- decaying isotope was required, the fission reaction was the only reasonable option as a production method. The case in which a short-lived, abundantly produced nuclide decays to the long-lived, less produced daughter nuclide was found at mass $A = 96$. In this mass chain, ^{96}Sr ($T_{1/2} = 1.07 \pm 0.01$ s) decays to ^{96}Y, which is less produced due to the chemical dependences of the ion guide and RFQ. As mentioned earlier, ^{96}Y has an 8^+ isomeric state ($T_{1/2} = 9.6 \pm 0.2$ s) and 0^- ground state ($T_{1/2} = 5.34 \pm 0.05$ s). The mass difference between these two states, 1.5 MeV/c^2, is sufficient for separation as can be observed from Fig.3.16.

The β^--decay of ^{96}Sr feeds only the ground state of ^{96}Y and thus the isomeric state of ^{96}Y is produced by fission reaction only. The intensity ratio of the states of ^{96}Y as a function of trapping time can be used as a probe for the β-recoil accumulation. If a significant number of decay products of ^{96}Sr were purified and detected, the ratio between observed ground state and the isomeric state would change as a function of the purification time. However, no significant change in the ratio was observed during the test. The upper 1σ limit for the fraction of trapped decay products is about 10 %.

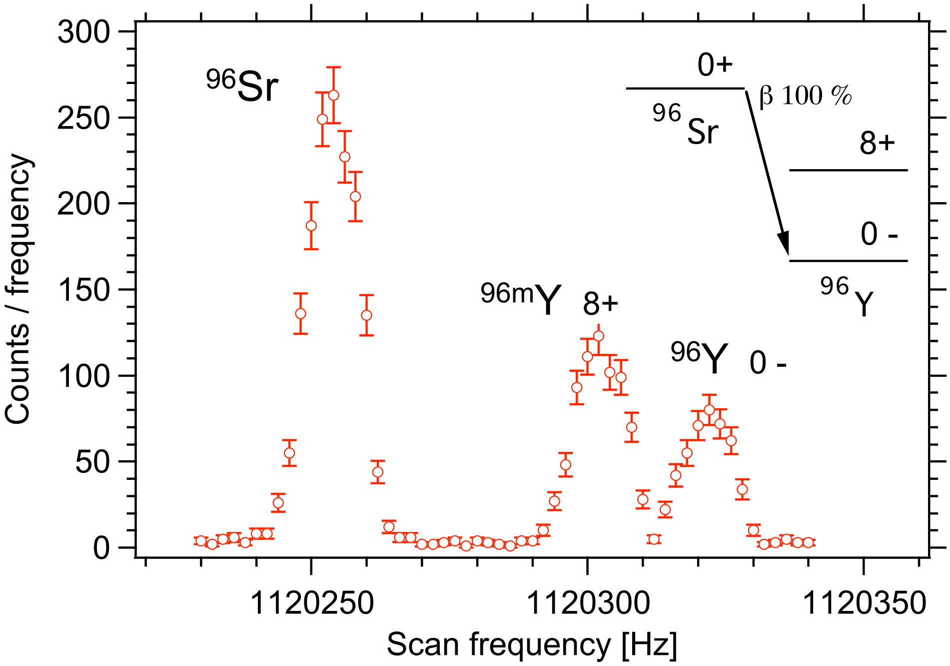

Figure 3.16.: A mass spectrum for the study of beta decay recoil accumulation in the trap. ^{96}Sr decays to the ground state of ^{96}Y. Since ^{96m}Y is produced only in fission reactions, a change in the intensity ratio of the two states of ^{96}Y as a function of trapping time indicates possible trapping of the daughter activity.

Radioactive decays

When transmission and detection efficiencies are excluded, the observed number of ions of a certain isotope, N, is proportional to the initial ion count N_0 of the same isotope extracted from the ion guide. Due to a short evacuation time from the guide, possible decay losses can be considered insignificant. Therefore, decay losses inside the RFQ and Penning trap are the only factors that need to be taken into account in the analysis. These losses can be described by two main terms of which the first defines the decay during the RFQ cooling cycle t_c. Ions are assumed to enter the RFQ at a constant rate N_0/t_c, which corresponds to a typical radioactive growth-in period. The decay losses during the purification cycle t_p are then defined by the second term. The relation between N and N_0 can be written as:

$$N = \frac{N_0}{t_c \lambda} \cdot \left(1 - e^{-\lambda t_c}\right) \cdot e^{-\lambda t_p} \tag{3.9}$$

where λ is the decay constant for the isotope of interest. The correction factor for timing parameters t_c and t_p can now be expressed as

$$\frac{N_0}{N} = \psi(\lambda) \tag{3.10}$$

with the correction function ψ:

$$\psi(\lambda) = t_c \lambda \cdot \frac{e^{\lambda t_p}}{1 - e^{-\lambda t_c}}. \tag{3.11}$$

Assuming that an equal cooling and purification timing is used for all measured isotopes of an element, the correction function described above can be used. If the timing between the measurements is different, the corrections due to chemical effects that possibly take place in the RFQ and trap do not cancel out in the yield comparison. In such cases, the correction function must be multiplied with a term that describes the losses due to chemical effects:

$$\psi_{chem}(\lambda) = \psi(\lambda) \cdot e^{-(A_c t_c + A_p t_p)} \tag{3.12}$$

where A_c and A_p are constants that describe the loss rate of ions due to the chemical reactions during the cooling and purifications cycles in stable operation conditions, respectively. Here, $A = 1/\kappa M$, where κ is the reaction rate constant of the element and M is the impurity concentration. These constants are not precisely known, but in principle, they could be approximated by using stable or long-lived isotopes of the studied element. Since the radioactive decay losses of such isotopes are negligible, the estimation could be done by varying the timing of the RFQ and the trap separately. The problem is, however, that the experimental conditions vary during the experiments and this estimation should be repeated not only for each element but also for each experiment. For all measurements that were done in this work, the purification cycle time was kept the same. In a few cases, the cooling cycle t_c was varied in order to adjust the MCP count rate. Though the uncertainty due to this contributes to the final uncertainty of the results, no correction to the peak intensity was applied in those cases.

The total uncertainty of the decay correction contains the statistical uncertainty of the peak intensity and the uncertainty of the correction function ψ, which is a function of the half-life of the studied isotope and the timing parameters of the measurement. The timing parameters, however, are so accurate that their contribution to the final uncertainty is negligible. Therefore, the relative uncertainty for the decay correction can be calculated from

$$\frac{\Delta N_0}{N_0} = \sqrt{\left(\frac{\Delta N}{N}\right)^2 + \left(\frac{\Delta\psi(\lambda)}{\psi(\lambda)}\right)^2}. \tag{3.13}$$

The statistical uncertainty ΔN can be directly calculated from the experimental data. The uncertainty of the decay correction $\Delta\psi$ can be estimated from the uncertainty of the decay constant λ and the derivative of ψ:

$$\Delta\psi(\lambda) = \Delta\lambda \cdot \psi'(\lambda) \tag{3.14}$$

and furthermore, the derivative of ψ' can be calculated from

$$\psi'(\lambda) = \frac{t_c}{\lambda} e^{-(t_c+t_p)\lambda} - \left(t_p + \frac{1}{\lambda}\right)\psi(\lambda). \tag{3.15}$$

The correction function ψ, plotted as a function of the half-life given in t_p units, is shown in Fig.3.17. In general, the decay correction is needed for all isotopes with half-lives less than 10 times the purification cycle length t_p. This correction function is simple and it can be applied to the results quite easily. On the other hand, the uncertainty associated with the correction function turns out to be rather complicated (see equations Eq.3.13 - Eq.3.15). Although it is not an insurmountable difficulty to compute this function with algorithms, the error analysis can be facilitated for non-computerized methods. As shown in the inset of Fig.3.17, $\psi(\lambda)$ is a monotonic function, in which the upper limit for the half-life is always matched to the smallest correction and the lower limit to the largest. In practice, it is easiest to calculate the upper and lower limits of the correction function from Eq.3.11 and hence to deduce the uncertainty. The uncertainty of the correction is asymmetric in nature due

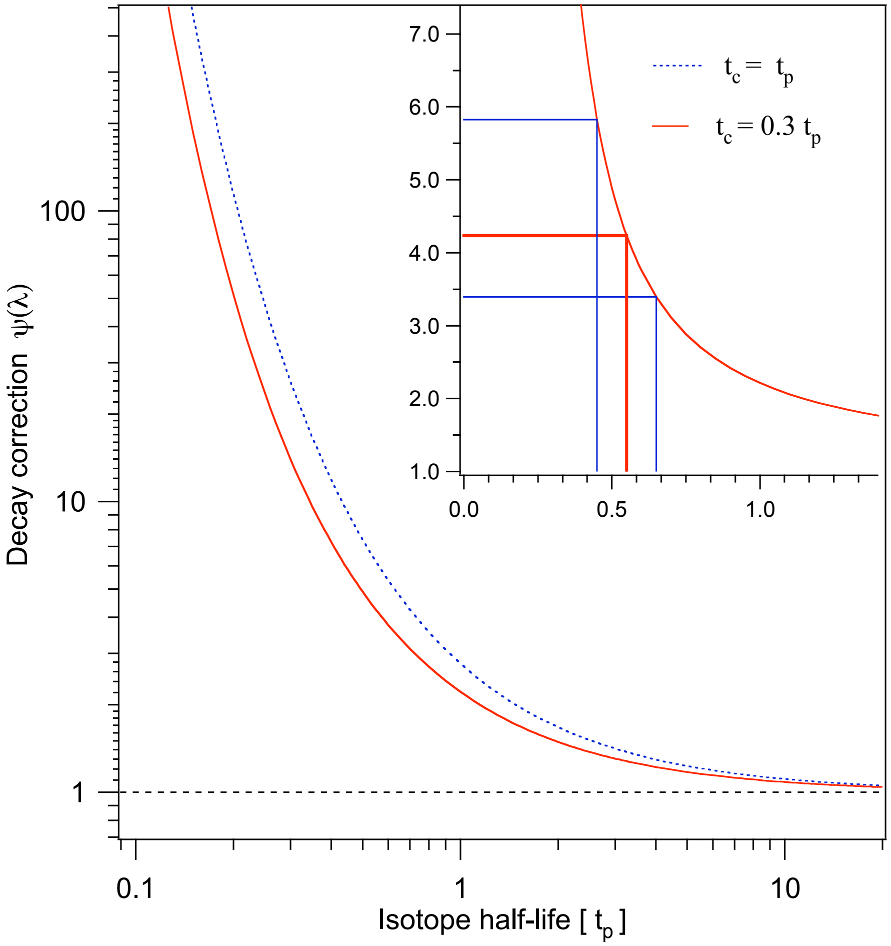

Figure 3.17.: The shape of the correction function $\Psi(\lambda)$ as a function of the half-life of the decaying isotope expressed in t_p units. The dashed (blue) line shows the correction that is needed when equal cooling and purification cycles ($t_c = t_p$) are used, while the solid (red) line introduces the correction for $t_c = 0.3 \cdot t_p$. The asymmetric nature of the uncertainty of the correction is illustrated in the inset.

to the non-linearity of the correction function $\psi(\lambda)$. This asymmetry is more pronounced for shorter half-lives that often are also the more poorly known. Therefore, the decay correction becomes the dominant uncertainty for the most exotic isotopes. Even though the actual uncertainty is asymmetric, the symmetric approximation, that is to say, the average of the asymmetric values, was considered to be sufficient throughout the analysis of this work. The half-life values of the isotopes used in this work were adopted from the NuDat2 database [66]. The total uncertainty of N always contains the statistical uncertainty and, if needed, the uncertainties due to irresolvable mass peak determination (Section 3.7.4) and the beam fluctuations (Section 3.7.8).

3.7.6. Effects of the ion bunch intensity

The charge handling capacity of the RFQ is known to be tolerant for ion count rates up to 10^4 ions/s [118]. According to the results introduced later in this section the same applies to JYFLTRAP. The intensities of mass separated ion beams used in this work were at least one order of magnitude less than this limit and thus no additional peak intensity corrections related to the transmission efficiencies of the RFQ and the trap is required from this point of view.

The MCP detectors [119] can usually handle constant ion rates as large as 10^7 ions/s without any significant errors of detection efficiency. As compared to the maximum beam intensity of the JYFLTRAP system, this may sound quite a large value. It is worth recalling however, that the ions are delivered from the trap as ion bunches, and all ions in the bunch reach the detector within a very short time interval. The MCP detectors are able to trigger single events with a certain time resolution. If more than one event occurs within this time resolution, only the first event is counted and the others are disregarded.

It can be deduced from the experimental data (see Fig.3.8) that the maximum width of the TOF peak is typically $\sim$100 μs. This reflects the maximum time deviation of the ions in the bunch although the actual time width of a single bunch may well be a few tens of μs. This means that a bunch of a few hundred ions already corresponds to a constant ion rate of 10^7 ions/s. If the bunch intensity is further increased, the MCP detector is not able to separate single ions from each other and some fraction of incoming ions cannot be detected. At some point the detection count rate saturates. This is the so-called ”pile-up” effect, which is analogous with the ”dead-time” effect of many other data counting systems.

The ”pile-up” effect can be studied by investigating the probability of the coincidence of two random events. With an average event rate R, the probability p for two random events to occur within a time interval τ is

$$p = 1 - e^{-R\tau}. \tag{3.16}$$

If the time interval τ is set to correspond to the shortest resolving time of the detector and R is matched to the average ion count rate hitting the detector, then p is also the probability to miss an ion due to this "pile-up" effect. In this work, the experimental count rate was not constant during the measurements. Indeed, most of the time it was almost zero, while the maximum count rate was reached at the top of peak in the TOF spectrum. For each individual 640 ns time channel however, a constant local count rate can be assumed. This local count rate R_i for each individual TOF channel can be estimated from the experimentally measured TOF spectrum, such as shown in Fig.3.8. It is thus possible to deduce the partial probabilities for each TOF channel separately. The total "pile-up" losses L for an ion bunch of N ions can then be calculated from the sum of these partial probabilities over the selected TOF gate:

$$L = N \left\{ 1 - \sum \left[\frac{R_i}{\sum R_i} e^{-R_i \tau} \right] \right) . \tag{3.17}$$

All parameters of the equation shown above can be deduced from the experimental data.

In addition to this theoretical approach, the saturation effect of the MCP detector was also experimentally studied with ^{120}Sn ions. The ion bunch intensity was controlled by varying the RFQ cycle time t_c from 1 ms to 580 ms. ^{120}Sn is a stable isotope which is also known to be rather insensitive to chemical reactions. Therefore, the number of ions in the bunch is a linear function of the RFQ cycle time. The result of this measurement is shown as open data points in the inset of Fig.3.18. The pile-up effect is noticeable as soon as an ion bunch of 100 ions is exceeded. In principle, this saturation could also be related to space charge effects in the RFQ, the trap or both. The ^{120}Sn resonance was scanned using a narrow frequency band only and therefore possible molecular beams, whose resonance frequencies often clearly differ from those of pure atomic elements, could be left unseen in the preparation phase of the purification process. For comparison with the simple model described by Eq.3.17, the required ion bunch size parameter N of the model was converted to the RFQ cycle time using the linear part of the experimental data of the ^{120}Sn measurement. From experience with the MCP detectors used in JYFLTRAP, the maximum observed ion count for a single 640 ns time channel was known to be ~6 to 7 ions. By using Eq.3.16 for a single channel, a time resolution of $\tau = 35$ ns can be deduced for the detector. With this time resolution, the saturation effect resulting

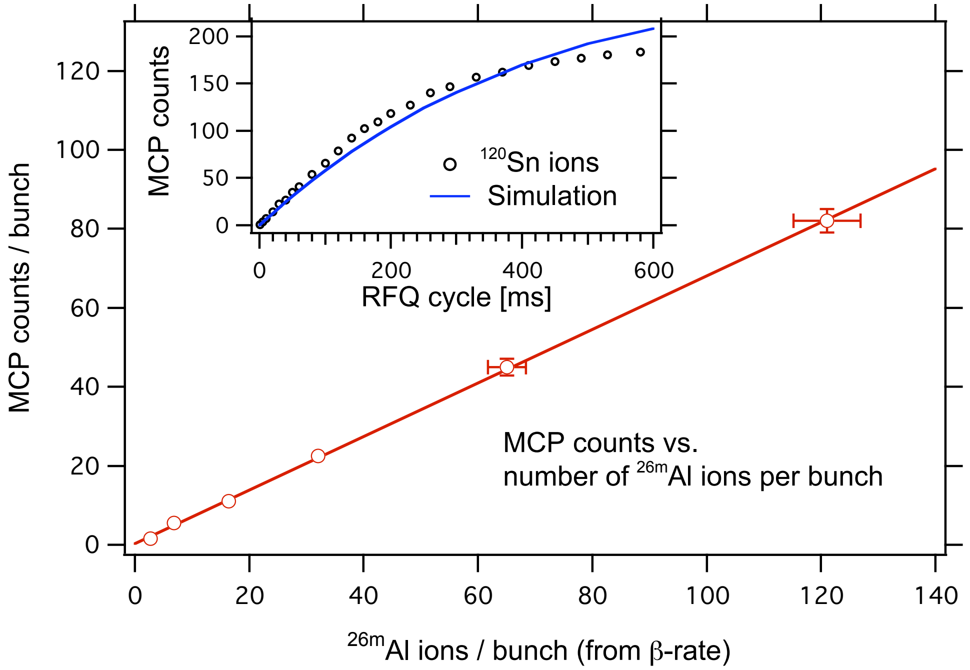

Figure 3.18.: The count rate saturation of the MCP detector. The main panel shows the count rate of the MCP detector as a function of the ion bunch intensity determined from the β-decays of ^{26m}Al ions. The inset shows the observed MCP count rate (open circles) as a function of the RFQ cycle time for stable ^{120}Sn ions. The predicted pile-up effect calculated from Eq.3.17 is shown as a blue solid line. See text for more details.

from Eq.3.17 is indicated as a solid line in the inset of Fig.3.18. The agreement between the experimental data and this simple model is generally good, especially since the experimental data was not used to adjust the calculation. This agreement also indicates that the saturation of the experimental data is most likely due to the pile-up effect of the MCP detector instead of any space charge related issues.

In addition to stable ions, the pile-up effect was also tested with radioactive ions of ^{26m}Al ($T_{1/2} = 6.345 \pm 0.002$ s) produced via a (p,n) reaction from a natural Mg target. The light-ion ion guide was used in the production of the isomeric state of this slightly neutron deficient isotope. According to the extended mass scan of the purification trap, other mass separated isotopes that resulted from this reaction were ^{26}Al ($T_{1/2} = 7.17 \pm 0.24\ 10^5$a) and stable ^{26}Mg knocked out from the target material by the primary beam. Therefore, the only considerable source of radioactivity was formed by the β-decays of ^{26m}Al. The relative abundance of ^{26m}Al was 12 % as compared to the other masses of the mass scan. The yield of ^{26m}Al was measured by using the MCP detector and two β-counting stations located before and after the trap facility (see Fig.3.2). Both stations used in this test are identical and they consist of a thin nickel foil located in a front of 300 μm thick silicon detector. For these counting stations, a total efficiency of 33 ± 1 % has been measured by using β-γ coincidences as discussed in [120].

In this case, the RFQ cycle time was varied from 5 ms to 270 ms, short enough for eliminating the need for the radioactive decay corrections due to the relatively short half-life of ^{26m}Al. The rate of purified ^{26m}Al ions was first measured with the MCP detector after the trap. The MCP detector was then removed from the beam axis and the measurement was repeated with the beta counting station located a few centimeters behind the MCP. All trap settings and parameters were kept the same during these two measurements and therefore the observed data of both measurements can be directly compared. This comparison is shown in the main panel of the Fig.3.18. The relation between the measurements is linear at least up to 120 detected ions per bunch with β-counting or up to 80 detected ions per bunch measured with the MCP. This in turn confirms that pile-up effects can safely be ignored in those cases where an observed bunch intensity of 80 ions is not exceeded. This was taken into account in the actual mass measurements by keeping the bunch intensity in most cases below 50 detected ions.

In addition, an efficiency of 68 % for the MCP detector can be deduced from the slope of Fig.3.18. A transmission efficiency of 1 % for the RFQ and the trap can be determined from the ratio of the β-counts detected before and after the RFQ-trap combination. It can also be deduced from Fig.3.18 that the operation of the trap system is linear at least for an ion count rate up to 120 ions/bunch, which corresponds to an ion number of $\sim 10^4$ injected into the RFQ. The measured abundance of ^{26m}Al was about 12 % of the total yield and therefore the RFQ must be tolerant at least for 10^5 singly-charged ions. This is an order of magnitude higher than the value estimated in [118]. Although the transmission efficiency of the RFQ was not separately determined in this work, a typical value for light ions is around 30 %. According to this, the largest intensity of an ion bunch that could be tolerated by the purification trap was $\sim$30000 ions.

3.7.7. Mass dependent variation of transmission efficiency

In this work, a typical mass range of each measured element, including the reference and the isotopes of interest, was about ten mass units. For the $A = 100$ mass region this means about 10 % relative variation between the extremes. Although the relative mass variation is rather small for heavier masses, it becomes more significant for the lighter masses. Therefore, the mass dependencies of the transmission efficiency of the entire ion production chain, beginning from the ion guide and ending at the MCP detector, are worth careful study.

The mass dependence of the ion guide

The first part of the ion production chain, in which a mass dependence may be introduced, is the ion guide. The fragments evaporated out from the uranium target have to pass through the nickel separation foil before they are stopped and thermalized by helium gas. Due to a relatively small stopping volume, the stopping efficiency of the ion guide is, however, very limited. Therefore, only a small sample (∼0.01%) of fission products can be evacuated from the ion guide as singly-charged ions.

The mass dependence of the ion guide is thus related to how well the distribution of fission fragments produced in the target is represented by the sample evacuated from the ion guide. In the ideal case, the fragment distribution in the sample is the same as that produced in the target. Since the full ensemble is not stopped in the gas and fragments initially have different kinetic energies, the assumption of an equal distribution is not obvious. The energy released from a fission reaction is divided by the fission products (two fission fragments and one or more neutrons). Some fraction of this energy is consumed by the binding energies of the fragments and the rest of the energy is converted to kinetic energy of the decay products. Within an isotope chain, the binding energy of the fragment increases towards more exotic isotopes and therefore the energy available after the reaction should be smaller for more exotic isotopes. There is, however, another fragment produced in the same reaction, and it becomes closer to stability the more exotic the first fragment. This balances the energy loss due to the different binding energies of the fragments and the total kinetic energy is more or less the same for all isotopes of a certain element.

In addition to the different kinetic energy of the fragments, the stopping power of helium gas is different for different masses. Nevertheless, it has been shown by the success of previous works performed with the ion guide technique [82–92] that the difference between neighboring isotopes cannot be very significant. This assumption is also supported by a good agreement between the results of this work and the results of other non-ion guide works as will be discussed later. Although the uncertainties due to the limited stopping and evacuation efficiencies of the ion guide contribute to the deduced fission yield results, their exact magnitudes have not been studied.

The mass dependence of the trap and the rf multipoles

Another probable source of mass dependency is the transmission efficiency of rf multipoles, the SPIG and the RFQ. These devices were used with constant parameters during the measurements of the element chains and therefore the transmission efficiencies may vary slightly over the measured masses. As shown in [105] however, if the RFQ has been correctly tuned, a constant transmission efficiency can be expected over a significantly longer mass chain than used in this work. Therefore, there is no reason to assume any significant enhancement of the uncertainty due to mass dependence of the RFQ transmission efficiency. A possible mass dependence of the Penning trap may be related to the effect of the buffer gas cooling during the purification process. For a mass range of about ten mass units, the cooling efficiency can, however, be considered almost equal for all isotopes and hence, the mass dependence of the Penning trap can be ignored.

The fact that higher order multipoles are better suited for broad mass range applications is confirmed by the studies of several rf-only multipoles performed in [121]. From this aspect, the mass range provided by the SPIG should be even larger than that of the RFQ. It is worth noting however, that the operational conditions of the SPIG and the RFQ are rather different. A typical ion current measured just after the SPIG system is of order several 100 nA when the fission-type ion guide is used. This corresponds to an ion rate of $\sim 10^{12}$ ions/s. If the TOF of ions passing through the SPIG is assumed to be at the level of 100 μs, the total number of ions accommodated by the SPIG at any moment of time is $\sim 10^{8}$ ions. The ion number inside the SPIG system is thus at least a thousandfold as compared to that inside the RFQ. At such high beam currents, the SPIG transmission is already perturbed by the space charge effect as discussed in Sections 2.4.5 and 2.5.6. The transmission efficiency of the SPIG was briefly studied by means of the simulations described in section 2.4. The simulation parameters were set to correspond to those in a typical fission experiment, except for the ion guide pressure, which was reduced to 100 mbar in order to reduce the simulation time. With an input current of 1 μA from the ion guide, the resultant transmission efficiency difference was about 2 % over the mass range of $A = 50$ - 80. For the heavier ions the efficiency seems to drop about 0.3 % per amu in a linear manner leading to a difference of $\sim$3% over the studied isotope chains. As compared to the magnitudes of other systematic uncertainties observed in this work, the mass dependency caused by the SPIG transmission efficiency is not a big factor.

The mass dependence of the magnetic mass separation

Probably the most obvious source of mass dependency is related to the operation of the dipole magnet of the mass separator. A systematic uncertainty arises due to the limited MRP of the beam after the separation. The magnetic dipole operates in a constant MRP mode and hence the width of an ion beam is inversely proportional to the mass. A typical FWHM of the $A = 100$ beam at the focal plane of the magnet is about 5 mm with a MRP of 300. In this work, the mass selection was made by using a fixed 7 mm slit. The fixed slit is due to the mechanical construction of the bender unit. It turned out only in the analysis that the slit width could be an issue for the beam transmission. In many cases, the total widths of the measured mass beams ($\sim 2\cdot$ FWHM = 10 mm) were wider than the slit and therefore some fraction of mass separated ions was lost due to collimation. The collimation effect of the slit for two beams with different masses is demonstrated in Fig.3.19. The FWHM are about 4 mm and 6 mm for beams A and C, respectively, the mass of the C beam being clearly lighter than that of the A beam. The collimation effect for beam A is almost insignificant, while the transmission efficiency of beam C is clearly reduced. The mass difference between the beams selected for this example is large, about 50 mass units if A corresponds with $A = 100$. In the vicinity of $A = 100$ with MRP $\approx$ 300, a difference of 10 mass units corresponds roughly to a difference of 1 - 2 % in the slit transmission.

The situation becomes significantly worse if the beam is not properly centered on the slit as illustrated by case B of the figure. The profile of B is similar to the profile of A, however shifted off from the correct value. The transmission efficiency for beam B is therefore significantly worse. It has been deduced that the transmission efficiency through the slit remains constant within ± 0.15 mass units around the correct mass value. This raises the importance of the mass calibration of the magnetic field, which is needed for both precise centering of different masses and the estimation of a possible uncertainty.

3.7.8. Yield fluctuations

In an ideal case, the ion guide efficiency and the transmission through the mass separator and JYFLTRAP should be stable over a long time period. Unfortunately, this situation is not very realistic at IGISOL. The yield of mass separated ions may vary due to many reasons. However, as long as the yield variations are both slow and smooth enough, they can be corrected for using linear approximations.

The main sources of yield fluctuations are related to changes in both the primary beam intensity and the number of impurity atoms in the helium gas. As long as

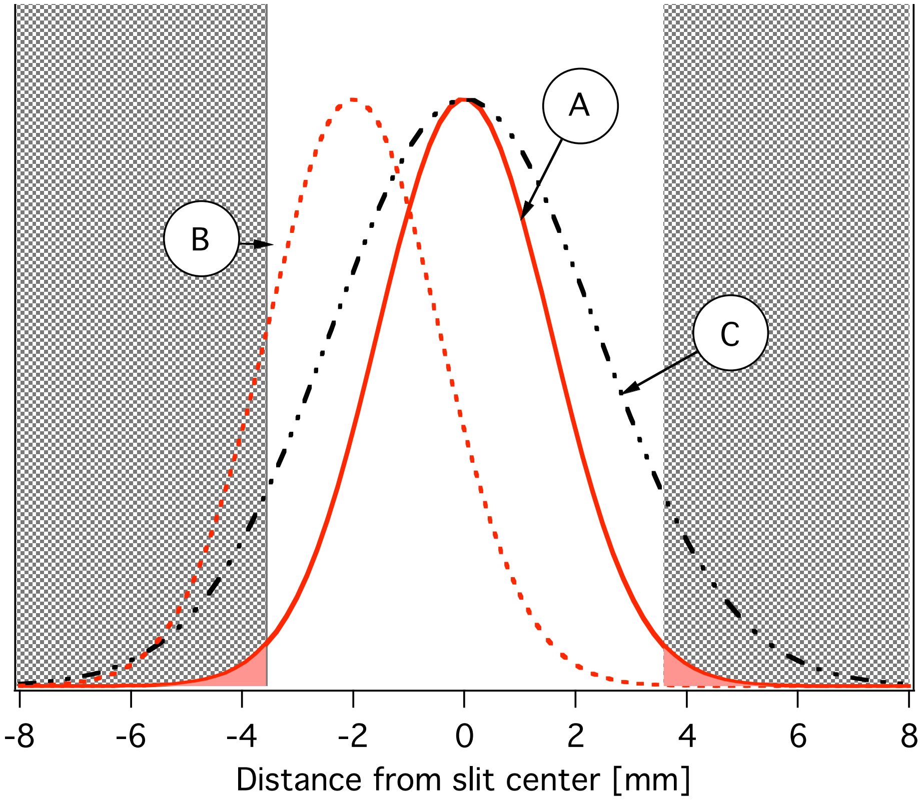

Figure 3.19.: An example of the collimation effects caused by a narrow slit (gray regions) for two different widths of beam. Case A illustrates the beam profile having a FWHM of ∼4 mm. The FWHM of case C is about 6 mm, representing the profile of a lighter mass beam. The profile shown in case B equals that of case A, now clearly shifted off from the correct value.

the cyclotron is working properly, the effects from the fluctuations of the primary beam are very small and they can be safely ignored. Changes in the impurity concentration directly reflect the yields of the products extracted from the ion guide. One significant source of impurities is caused by molecules released from the walls of the ion guide and the gas feeding lines. The amount of gas impurities can be reduced by pumping and heating the lines before an experiment. The ion guide is effectively cleaned by internal heating due to the primary beam and therefore its efficiency slowly increases during the first days of on-line experiments. The helium gas is additionally purified by passing it through a LN_2 (liquid nitrogen) cooled cold trap before feeding it to the helium line. Over time the impurities accumulate inside the cold trap reducing the purification efficiency and increasing the level of impurities in the helium gas. In order to keep the gas purification system continuously running, two parallel cold traps are used, of which one is always functioning, while the other is being regenerated by heating and pumping.

The yield fluctuations related to the impurity concentration in helium gas are generally very slow and smooth and they can be taken into account by a careful preparation of the measurement. Over a time period of several hours or days, changes in the ratios of yields of isobars were observed. These ratios could be followed via repeated measurements of reference isotopes over a long time period. Since these fluctuations directly affect the elemental distribution of fission products, they are most likely caused by some chemical process and thus are related to the impurity changes in the buffer gas. These changes appear to be continuous and very slow in time; typically less than 0.5 % per hour. As one measurement of studied mass and two references typically took less than 90 minutes, such a long-term fluctuation is not to be considered a serious problem.

The fluctuations observed in this work proved to be so rapid, they could not be explained by chemical reactions. In many cases, the fluctuation patterns were also rather complicated as can be observed from Fig.3.9 and particularly from Fig.3.21, for example. The changes seem to occur within a few steps rather than as a result of a steady evolution. Moreover, as can be seen from Fig.3.9 and particularly from Fig.3.20, the observed fluctuation patterns for each measured element are very similar, which strongly supports the supposition that the source of fluctuations is related to changes in electric or magnetic fields.

3.7.9. Virtual reference method

The arithmetic mean of the yield over a fluctuation is often used as a correction tool for time-varying data. In this work, the mass selection as well as data and spectra saving were all performed manually, which means that the time gaps between

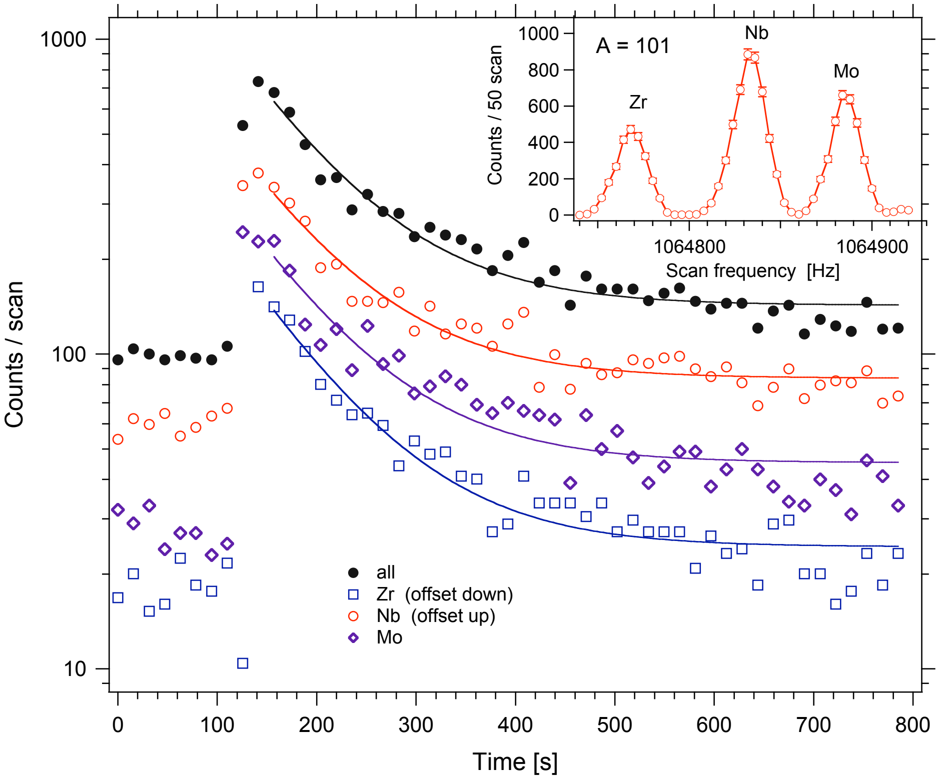

Figure 3.20.: Yield fluctuation observed in the measurement of $A = 101$. The observed time histories of ^{101}Zr (blue squares), ^{101}Nb (red open circles) and ^{101}Mo (blue diamonds) are shown in the main panel. The solid black circles indicate the history of the total yield and the actual mass spectrum is shown in the inset. In order to improve the clarity, the yields of Zr and Nb have been shifted down and up, respectively. The lines associated with the measured data are simple exponential decay curves, each calculated with the same time constant. A good agreement between these curves and the data indicates that the observed fluctuation is very similar for each isotope.

the sequential mass scans extended up to several minutes. In addition to this, the duration of the time gaps preceding and following a measurement of a studied isotope were often different. In such a case, even though the observed fluctuation could be linear, the arithmetic mean of the reference yields does not necessarily provide a proper correction. Instead, the time corrected average of the reference yields may provide a better result.

In general, a comparison between the yields of reference and measured isotopes should be done with the data captured at exactly the same time. Since this was not possible in this work, the yield of the reference isotope was deduced by interpolating between the reference history spectra collected before and after the measurement of the studied isotope. Examples of different types of time history spectra recorded during the measurements are shown in Fig.3.21. The black open circles indicate the reference time spectra preceding and following the spectrum of the studied isotope, shown as the red solid data points. If the fluctuation is not element depended, the sum of counts over the entire mass spectrum can be used instead of the sum of counts contained in a single mass peak. This helps to improve the statistical uncertainty especially for the less intensive yields of exotic isotopes. For example, the time history of ^{133}Sn with 80 counts over 151 scans would be rather difficult to interpret as such. As can be observed from Fig.3.20, the short-time fluctuations are not element dependent and therefore the approach used here is appropriate. The x - axis in Fig.3.21 shows the time scale in minutes. Different time gaps between the reference and studied isotope measurements, as discussed earlier, are clearly visible, particularly in panel (d) of the figure.

The ideal case of the time evolution is shown in panel (a) of Fig.3.21. No significant fluctuation in time can be observed and therefore the yields of both the reference and the studied isotope can be easily compared by using simple linear approximations, in other words, the arithmetic mean of the yields. The same can be applied to the case shown in panel (b) with an almost linearly declining yield. However, the situation becomes slightly more difficult in panel (c). Although the trend of the fluctuation in a single reference measurement is rather linear, a clear change of the yield can be observed in the yield of the studied mass. The use of the linear approximation in such a case would be misleading. Panel (d) shows a real challenge for the reference yield estimation. The sharp peak in the last reference measurement results in a completely incorrect linear approximation. Even if the peak was ignored, the deduction of the correct reference level would be very difficult. The yields of the references are clearly shifted without any evidence of the fluctuation. It is thus impossible to accurately deduce whether the yield shift has occurred before or after the measurement of the studied isotope.

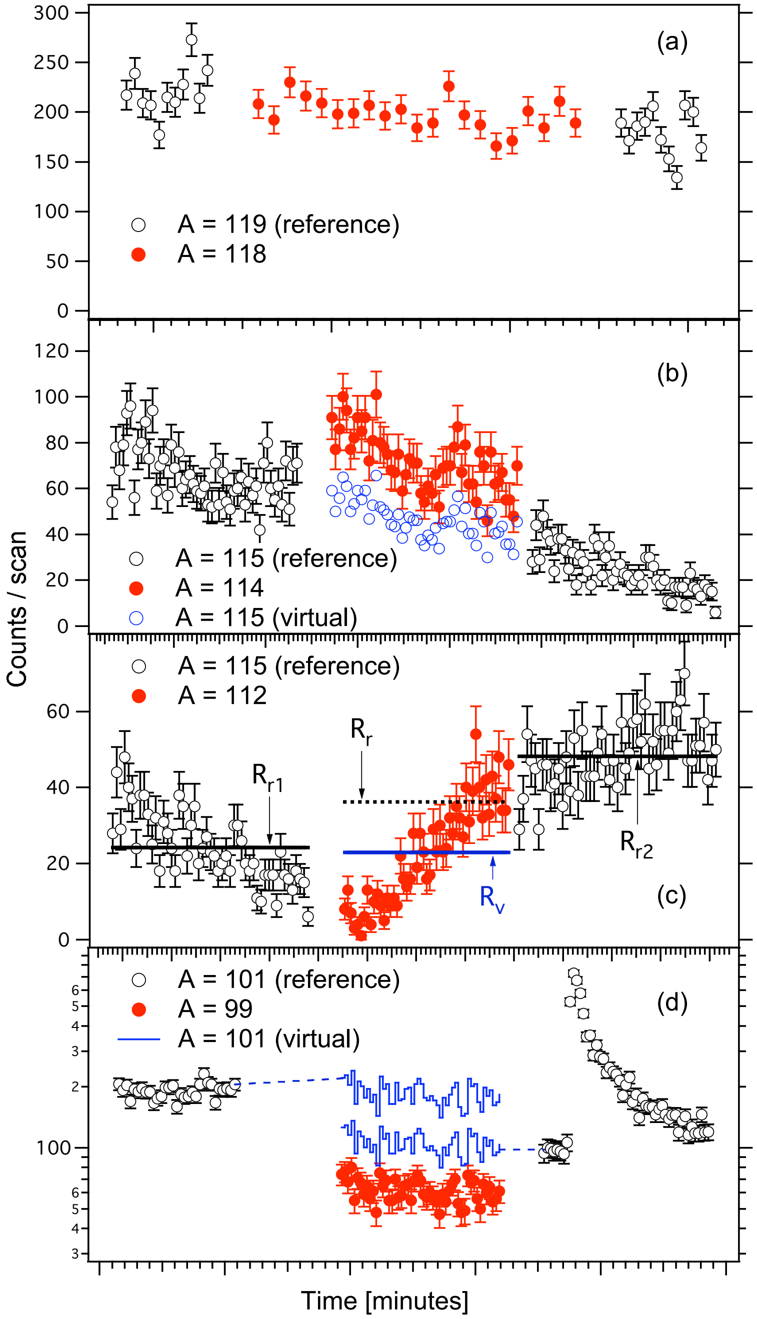

Figure 3.21.: Time histories for the total yields of a few measurements. The time histories of the reference measurements are shown as the black open circles and the time history of the studied mass between the references is shown as the red solid circles. The virtual references needed for the fluctuation correction are shown as the blue circles in the second panel and as the blue lines in the fourth panel. An absolute time is not given; each tick of the time axis represents one minute. See text for more details.

As long as the fluctuation is element independent, there is no reason why the reference elements would behave in a different way to the studied elements. Therefore, the time history of the studied mass can be used as a basis for the virtual reference. The level of the virtual reference can then be estimated by scaling the history of the studied mass in such a way that the trend of the reference yields, coupled by this virtual reference, becomes continuous. The uncertainty of the virtual reference is estimated in a subjective manner by searching for minimum and maximum levels of the virtual reference that still provide a continuous coupling between the actual reference measurements. In Fig.3.21, the deduced virtual reference is indicated as a blue color for the cases (b) - (d).

In panel (c), only the arithmetic mean of the virtual reference, R_v, is shown for the sake of clarity. The arithmetic means of the reference histories, R_{r1} and R_{r2}, are indicated as horizontal lines. The arithmetic mean of the reference measurements, R_r, is 36.2 while the mean of the virtual history, R_v, is only 22.9. Therefore, the obtained correction factor R_v/R_r due to the non-linearity of the reference history is 0.63. The resultant uncertainty of the virtual reference is quite high, about 15 %, due to the subjective estimation of the minimum and maximum levels. In this work, the uncertainty of virtual references varied typically between 5 % and 20 %.

In panel (d), it is not obvious how the virtual reference should be matched to the reference history. In this case the virtual reference matching can be done as follows. The connection between the first reference and the studied isotope (the leftmost dashed horizontal line) is first matched. Then, a similar matching process is repeated for the second connection (the rightmost dashed horizontal line). The results of these operations are shown as the blue curves. In this case, it is obvious that either history curve is the correct representation of the reference history. However, additional information is required before the selection of the correct history curve can be made.

This particular measurement of $A = 99$ isotopes was repeated a couple of hours later because the original measurement was observed to be erroneous. The latter measurement took place under stable conditions resulting in the yields of 166 ± 7 %, 37 ± 2 % and 9.7 ± 1.0 % for ^{99}Zr, ^{99}Nb and ^{99}Mo, respectively. These yields are given with respect to the reference yield of the corresponding $A = 101$ isotopes. The uncertainties of the results contain the statistical uncertainty, the radioactive decay correction and, for ^{99}Nb, the uncertainty due to irresolvable isomers with different half-lives. If both joints of the original measurement are used to adjust the virtual reference, the yield values are only ~60% of those of the repeated measurement. Using only the latter joint, yields of 142 ± 7 %, 36 ± 2 % and 8.6 ± 0.9 % can be deduced for ^{99}Zr, ^{99}Nb and ^{99}Mo isotopes, respectively. In the latter case, the agreement with the values from the repeated measurement is good, especially when taking into account the poor quality of the original data. Although the remeasured values were used in the selection of the correct joint in this particular case, this example illustrates the adequacy of the virtual reference method as a correction tool for fluctuations. In some cases, it may be possible to deduce the correct joint via interpolation from the yields of neighboring isotopes. In a general case, however, if no additional information is available, the different virtual histories represent only the upper and the lower limits of the virtual reference and the yields cannot be accurately deduced.

3.7.10. Yield calculations

Once the data has been sorted and all erroneous ion bunches removed, the intensities of the mass peaks can be deduced for both the studied and the reference isotopes. Since the measurements of the reference and actual isotope may consist of a different number of scans, the intensities are scaled as equal samples of the yields (as "counts per scan" units). The radioactive decay corrections, if needed, are then applied to the deduced peak intensities and the arithmetic mean of the reference peak intensities is calculated (see R_r in panel (c) of Fig.3.21). This corresponds to a linear change of the overall efficiency. If the efficiency change is not linear, the mean of the reference isotope intensities is finally multiplied with the correction factor R_v/R_r provided by the virtual reference approximation as described in the previous section. In this phase, all possible corrections due to the mass dependence of the facility should be applied to the intensities. In this work however, those mass dependencies were negligible compared to the fluctuations of the yield and thus could not be studied. All possible uncertainties contributing to the final intensities are considered as independent and are added quadratically.

Finally, the mean of the reference isotope intensity and the intensity of the studied isotope should be comparable to each other. The comparison between these two intensities results in the relative intensity of the studied isotope with respect to the selected reference isotope. The intensities of several isotopes produced in fission form an isotopic fission yield distribution, once again, with respect to the selected reference isotope. In order to convert this distribution to the independent fission yield of isotopes or the independent fission cross-sections of isotopes, the independent fission yield or fission cross-section of an isotope participating in the distribution is required.

3.8. Results

The new method of relative fission yield determination with JYFLTRAP has been developed and tested in three separate experiments during the years 2005 - 2007. Within three weeks of experiment time, the relative yields were measured for 240 isotopes in 25 MeV proton-induced fission and for 54 isotopes in 50 MeV proton-induced fission of ^{238}U. Since the main focus of this work has been the development of the method, only results that are relevant to the discussion of the capabilities and drawbacks of the method are given. These results include the independent yield of Ge, Ag and In for 25 MeV proton-induced fission and Rb and Cd yields for 50 MeV proton-induced fission.

The results are given in arbitrary units for the distributions shown in Fig.3.22 and Fig.3.23 or are normalized to the cross sections of previous works for the distributions shown in Figs.3.24, 3.25 and 3.26. In Fig.3.23 the arbitrary unit has been chosen in such a way that the observed yield distribution coincides with the cross section in millibarns as deduced from Ref. [85]. The cross section given in [85] has been normalized to theoretical calculations and therefore the final unit shown in this work is still considered as arbitrary. Where possible, the normalization to existing cross sections is done by equalizing the Gaussian fitted areas of the distributions. Since each available data point has been used in the fit, possible fluctuation effects of a single data point reduces and the quality of the normalization improves. The only exception is the normalization of the yield distribution of the cesium chain (Fig.3.26), in which only the neutron rich side has been used in the fit due to the asymmetry of the distribution.

3.8.1. Consistency of measured yields

In this work, the overall uncertainty of the results includes four independent sources of possible errors. Though these sources have been detailed in the previous sections, a short review is given below:

1. Uncertainty in the intensity of the mass peak. For typical cases this is only the statistical uncertainty and thus it is relatively small. For those mass peaks whose intensities are deduced by fits, the uncertainty of the fit is used because it already contains the statistical uncertainty.

2. Uncertainty due to possible radioactive decay corrections. The magnitude of this uncertainty greatly depends on the error of the half-lives of decaying nuclei. For very short and inaccurate half-lives, the applied uncertainty is

asymmetric. In this work however, the symmetric approximation has been used for each case.

3. Uncertainty due to poorly known isomeric state ratios for close-lying isomers with different half-lives. This is a special case of (2), in which accurate isomeric state ratios of the irresolvable isomers are required for a proper radioactive decay correction.
4. Uncertainty due to chemical reactions in the RFQ. This uncertainty occurs only if different RFQ cycles have been used in the measurements of the reference and the studied isotopes.

These are the sources that are included in the error analysis of the results handled in this work. In addition, there are two other sources of uncertainty:

5. Uncertainty due to mass dependence of the IGISOL and JYFLTRAP facilities. It is likely that only the mass dependence of the mass separator is significant enough to disturb the measurements within the selected mass range. This uncertainty is systematic in nature and it should be taken into account in the analysis. In this work however, this uncertainty was dominated by (6) and hence could not be studied.
6. The final source of uncertainty is the rapid time-scale yield fluctuations. These fluctuations are most probably related to the manual control of the IGISOL dipole magnet, are random in nature and are treated by using the virtual reference tool. This tool produces the best possible estimate for the yield fluctuations based on the observed trends of the time histories. This uncertainty is applied to the results of this work where needed. The estimated uncertainty of the virtual reference is large, typically of order 5 - 20 %.

The output of these experiments was performed in such a way that the maximum amount of information from the studied reaction was measured. Therefore, there are a few cases that have been measured twice in separate experiments. One example is Ag, which was measured using both ^{119}Ag and ^{115}Ag as a reference isotope. It thus provides a perfect test for the reproducibility of the method. The isotopic silver distributions measured in both experiments are shown in the top panel of Fig.3.22. Both distributions are normalized to one at mass $A = 119$ which is one of the reference isotopes. Even though the linear approximation was used for the reference yield calculation, the distributions are consistent with each other. Small differences are seen at $A = 117$ and $A = 118$ but those discrepancies are not significant. The error bars for the data of the top panel contain the error sources (1)-(3).

The same distributions, now corrected with the virtual references, are shown in the bottom panel. In order to emphasize the uncertainty of the virtual reference method, no other error sources have been included in the error analysis. Due to the virtual reference, the overall agreement between the distributions is better although the discrepancy between the yields of $A = 120$ has slightly increased. This discrepancy is, however, insignificant as the yields stay well within the error margins. The main conclusion of this test is that the yield determination using the Penning trap coupled to IGISOL is very reproducible. Fission yield distributions can be accurately repeated using separate experiments as well as separate reference isotopes.

3.8.2. Comparison to the other ion guide works

The IGISOL facility has been previously utilized in the fission yield measurements of $^{71-74}$Cu, $^{74-79}$Zn, $^{76,78-81}$Ga and $^{78-82}$Ge [85] and in $^{99-103}$Y, $^{105-110}$Nb, ^{111,112}Tc, $^{127,128,130-133}$Sn, $^{130-134}$Sb and ^{133,134}Te [86]. The independent yield of the Tc chain can be extended as far as ^{114}Tc based on [88]. In all experiments, 25 MeV proton-induced fission of ^{238}U was used. Unlike this work however, the yields of fission fragments of other works have been determined via β-γ-spectroscopy located at the central beam line of the IGISOL. Hence, a direct comparison between two different yield detection methods can be provided. Yet another ion guide experiment, introduced in [87], provides independent fractional mass yields for the products of 24 MeV proton-induced fission of ^{238}U. This latter work was, however, focused on the most probable charge of fission products and thus the data given in the article cannot be compared with the present yield distributions.

Germanium isotopes from 25 MeV proton-induced fission

A comparison between the isotopic yields of germanium is shown in Fig.3.23. The red diamonds represent the distribution obtained in Ref. [85], while the black solid points show the distribution deduced in this work. In [85], the mass separated fragments were implanted in a thin tape and measured using a $\beta - \gamma$ detector setup in saturation mode. The tape was moved on occasion in order to remove a build-up of activity in front of the detectors and improve thus the detection sensitivity for the most exotic isotopes. The error bars of the data points observed in this work contain the uncertainties of the peak intensity and radioactive decay correction. Extended lines over the error bars indicate the uncertainty caused by the corrections due to the fluctuating yields. Detailed information about the error analysis of [85] is not explicitly introduced in the article.

The overall agreement between the results is relatively good. The only exception

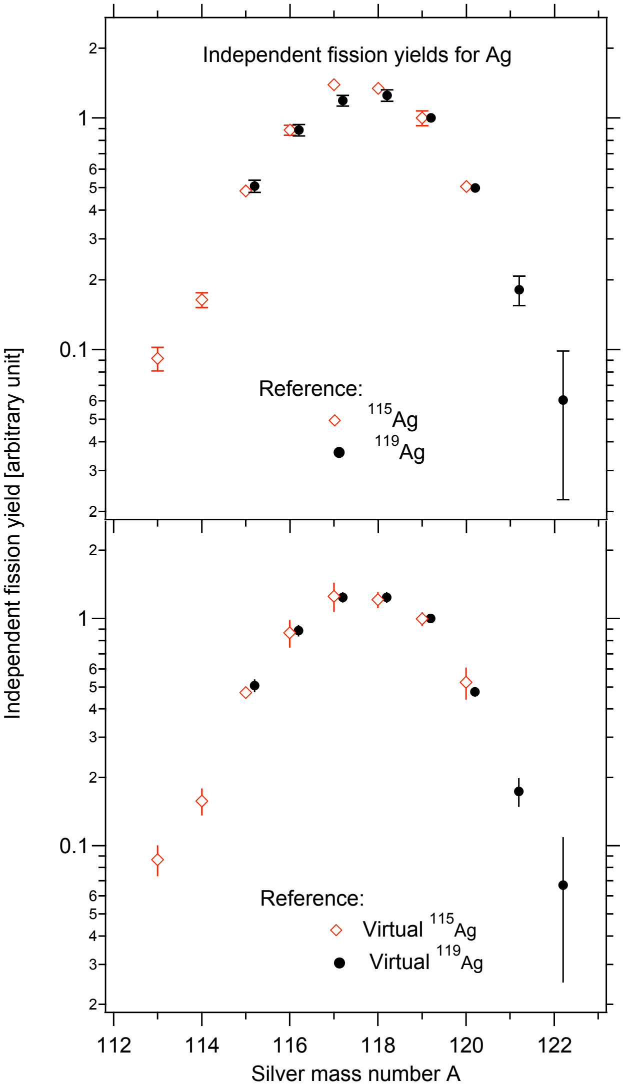

Figure 3.22.: The isotopic yield distributions of the silver isotopes in 25 MeV proton-induced fission obtained in two separate measurements. The comparison between two distributions measured with ^{115}Ag and ^{119}Ag as reference isotopes and deduced without virtual reference correction are shown in the top panel while the same distributions, now corrected with the virtual references, are shown in the bottom panel. See text for more details.

occurs at mass $A = 81$, in which a clear discrepancy between the data points can be observed. The deduced yield of ^{81}Ge from [85] is anomalously high and does not coincide with the expected Gaussian-shaped distribution. The over estimation of this yield may be due to the use of an incorrect γ-branching ratio for the $9/2^+$ ground state of ^{81}Ge, whose β-decaying $1/2^+$ isomeric state is also produced in fission. Both states have the same half-life of 6.5 s but their decay patterns are different [122]. Due to the identical half-lives, the isomeric state has probably not been taken into account correctly. On the other hand, the different decay schemes of the isomers may cause a mixing of the decay branching ratios and thus a skewing of the results. In addition, the production ratio of the isomeric states of ^{81}Ge given in [122] has been deduced from thermal neutron-induced fission and it may be different for proton-induced fission. In the current work, the production ratio of the isomeric states is insignificant since the half-lives of the states are the same and both can be counted in the same mass peak. This illustrates the benefit of direct ion counting as a method of yield measurement.

3.8.3. Comparison to other mass separator works

The comparison between different IGISOL measurements strengthens the confidence that the yield distributions obtained by decay spectroscopy can be reproduced with the Penning trap-based ion counting method. When comparing to other facilities, the experimental yield distributions of Rb, Cs and In isotopes for proton-induced fission of ^{238}U are available in [13, 14]. These elements are highly volatile and relatively easy to ionize, which has allowed the use of chemically selective ion sources. Due to the chemical selectivity, pure beams of single isotopes have been produced by means of simple magnetic separators. The yields of these volatile fission products were determined very precisely by using an ion multiplier to directly count the ions. Since the problems and inaccuracies related to the traditional decay spectroscopy could be avoided, the distributions offered by these works provide an excellent test case for the method of the present work.

Indium isotopes from 25 MeV proton induced fission

The independent production cross sections for $^{119-129}$In isotopes in 30.4 MeV proton-induced fission of ^{238}U are reported in [13]. An ion source heated up to 1800 ^{o}C was used to release the indium isotopes from a target system [78, 79]. The isotopes were then ionized by surface ionization at the exit slit, were mass separated by a magnetic mass spectrometer and finally, were individually counted by means of an electron multiplier. The target system used in [13] consisted of 23 carbon blocks implanted

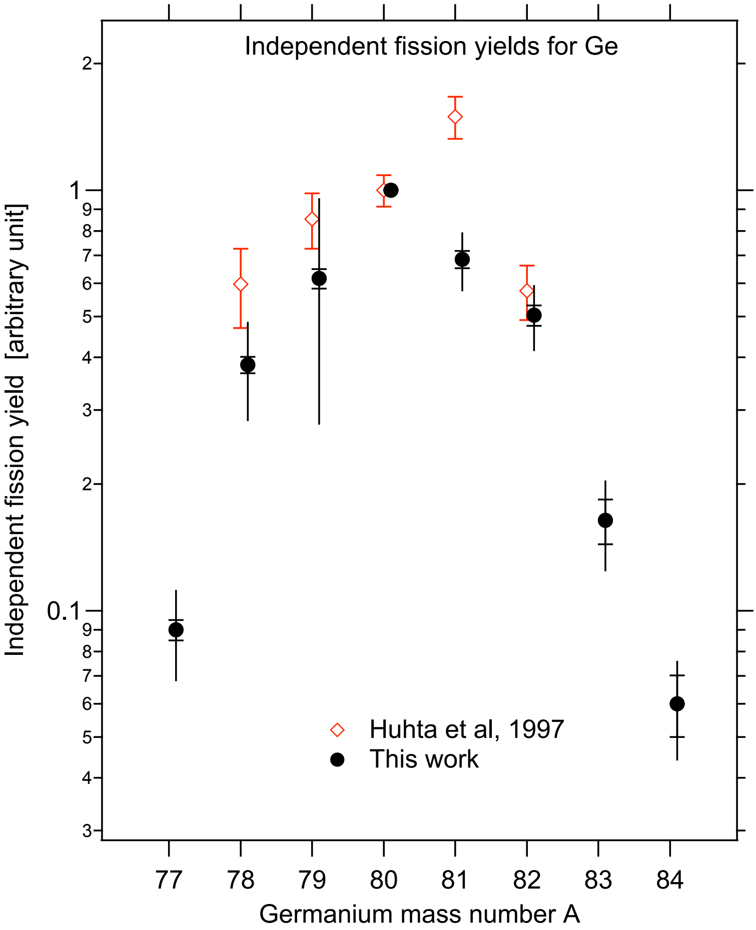

Figure 3.23.: The isotopic yield distributions of the neutron rich Ge isotopes in 25 MeV proton-induced fission of ^{238}U. The red diamonds are from [85] and the solid black points show the distribution deduced in this work. The error bars of the present work contain the statistical uncertainty as well as the uncertainties from the radioactive decay corrections. The virtual reference method was utilized in order to correct the yield fluctuations. Additional uncertainties due to this are indicated as extended lines of the error bars. ^{80}Ge was used as a reference isotope in the present work.

with uranium oxide $^{(238)}U_3O_8$. The total thickness of the carbon blocks was 650 mg/cm^2 and the total thickness of the uranium oxide layers deposited on the carbon blocks was 120 mg/cm^2. As a result, the energy loss of a 30 MeV proton beam in such a target system is about 15 MeV, which is large compared to ~1.0 MeV energy loss of the 25 MeV proton beam in the self supported metallic uranium target used in the present work. However, the average energies of the proton beams in the targets are quite similar in both cases and it is thus reasonable to expect that the resultant yield distributions of indium isotopes are similar enough to be able to make a proper comparison.

Due to the larger energy distribution of the protons in the target in [13], the isotope distribution reported should be slightly wider than that measured in the present work. Indeed, this was observed for the stable side of the isotopes, as can be seen from Fig.3.24, in which the distributions of In isotopes measured in [13] and the present work are compared to each other. On the other hand, it is also possible that the enhancement indicates an accumulation of the long lived isotopes at the target system in [13]. An enhancement of the yields on the neutron rich side of the curve would also be expected in the case of [13] since the proton energies in such a target system can be as low as 15 MeV. However, this effect is not seen in the figure.

Rubidium isotopes from 50 MeV proton-induced fission

The independent cross sections of $^{131-145}$Cs and $^{86-98}$Rb isotopes in 50 MeV proton-induced fission of ^{238}U are reported in [14], in which a similar experimental arrangement as in [13] was used. In [14], the uranium salt had been deposited on 70 μm thick carbon strips forming a target system that consisted of 280 mg/cm^2 carbon and roughly 80 mg/cm^2 uranium. The target stack was resistively heated up to 2000 ^{o}C and bombarded by a 50 MeV proton beam. The isotopes of $^{131-145}$Cs and $^{86-98}$Rb were ionized at the exit of the ion source, were mass separated by a mass spectrometer and were counted by means of an ion multiplier. The total energy loss for a 50 MeV proton beam in such a target stack is 3.5 MeV. At IGISOL, for an equally energetic proton beam, the energy loss is about 0.5 MeV. Since the difference of the energy distributions is rather small, a similar isotopic distribution between [14] and the present work can be expected.

In the present work, an ambitious attempt was made in order to measure Rb isotopes starting from stable ^{85}Rb. For this reason, the measurement of the isotopes was realized in two separate sets. In the first set, ^{91}Rb was selected as a reference isotope for the measurements of $^{85-93}$Rb isotopes. In order to keep the yields of reference and studied isotopes at the same level, the reference isotope was later changed to ^{94}Rb for the measurements of $^{93-98}$Rb isotopes. However, this attempt

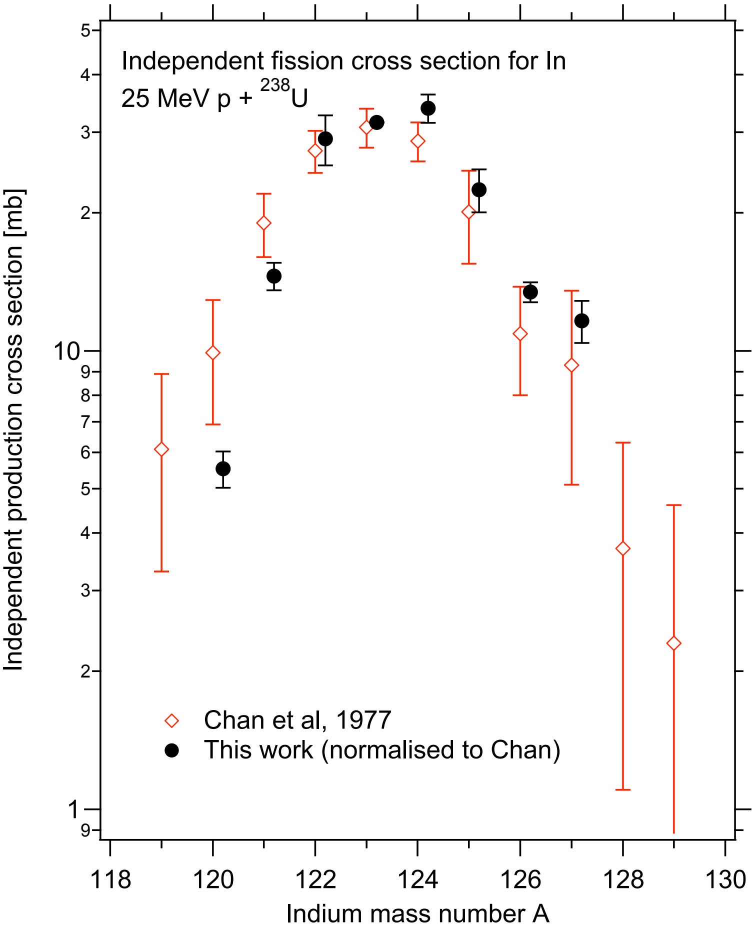

Figure 3.24.: The independent yields of neutron rich In isotopes in 25 MeV proton-induced fission of ^{238}U. The red diamonds are from [13] and the data obtained in this work is represented by the black solid points. The uncertainty in [13] is large partly due to low yields and partly to the absolute cross section normalization point, ^{117}In, lying outside the measurement range.

was not successful due to the encountered difficulties that are typically related to all measurements close to stability.

At mass $A = 85$ the mass peaks of ^{85}Rb and ^{85}Kr could not be resolved from each other. In general, the yield of ^{85}Kr is about ten times higher than that of ^{85}Rb. In this particular measurement however, the observed yields of Kr isotopes were dramatically suppressed as can be observed from Fig.3.8. This was due to a gas leak in the RFQ, which led to losses of Kr isotopes via charge-exchange reactions. The yield of ^{85}Kr could be extrapolated from the yield of ^{87}Kr and from the distribution of Kr isotopes determined in a separate set of measurements. After the correction, the yield of ^{85}Rb was observed to be about 260 times higher than expected from the results of [14], from the theoretical calculations based on [7] and from the extrapolation of the yields of the other Rb isotopes. In a similar manner, an enhancement was observed in the yield of ^{87}Rb. Both isotopes are stable and therefore the front end of IGISOL must have been contaminated by natural rubidium. The yield of the fission-produced ^{87}Rb was estimated from the known abundances of the natural isotopes and from the yield of the stable ^{85}Rb. The appearance of stable isotopes in this work is discussed more in detail in section 3.9.2

At mass $A = 86$, the mass peak of ^{86}Rb overlapped with ^{86}Kr, a stable isotope of krypton. The intensity of ^{86}Kr was large, despite the leak in the RFQ, since it is present as an impurity in the helium gas. For this reason, it was not possible to approximate the amount of ^{86}Kr by using the separately measured distribution. If the yield of ^{86}Rb is estimated in a similar manner as that of ^{85}Rb, it is found that the rate of ^{86}Kr after the trap is about 40 times higher than the rate of ^{86}Rb. This ratio is too high for the proper fitting of multiple peaks and therefore the yield of ^{86}Rb could not be deduced either.

Fortunately, the deduction of the yields of $^{88-93}$Rb was straightforward since no overlapped peaks are found in this region. The measurements with ^{94}Rb as a reference were not so successful. In the mass region of $A = 96$ - 98, some very intense mass peaks appeared in the spectra. The origin of these peaks remains unsolved and since their masses do not match any atomic nucleus, they are interpreted as belonging to molecular ion beams. Therefore, the yields could be deduced only for $^{93-95}$Rb isotopes.

As seen from Fig.3.25, the general agreement between the distributions of [14] and the present work is excellent, particularly for the isotopes in which ^{91}Rb was used as a reference. Also the ratio of the yield of ^{94}Rb and ^{95}Rb agrees with that given in [14], although their nominal values seem to be about 30% lower. The data between the two measurement sets of the present work has been linked together via one duplicate measurement of ^{93}Rb. Even though no error could be traced in the

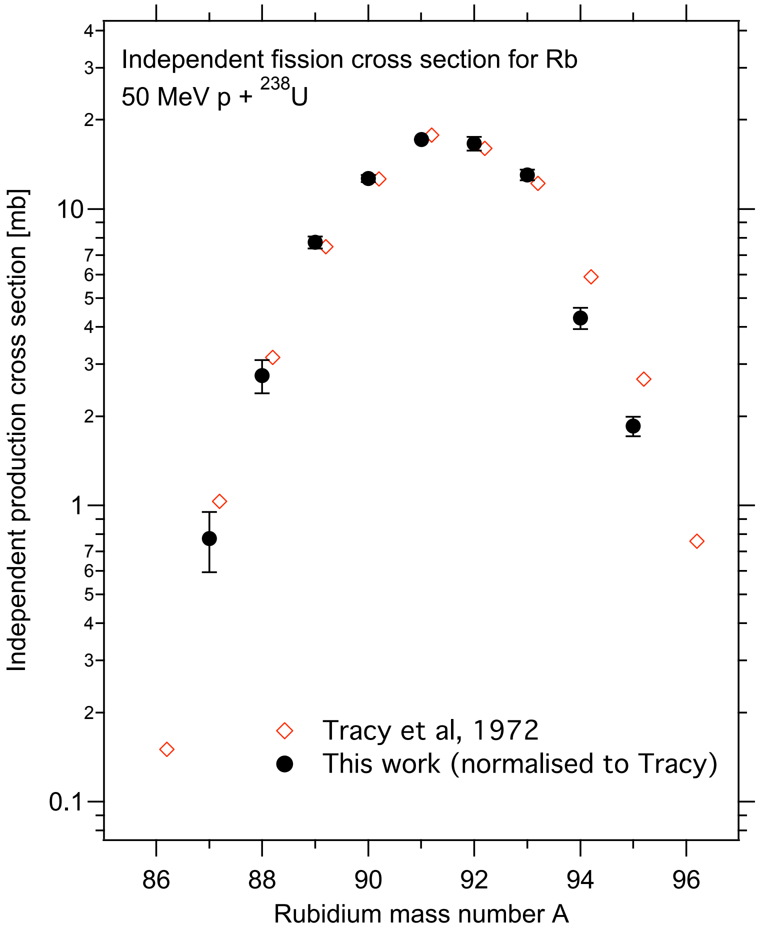

Figure 3.25.: The independent yields of neutron rich Rb isotopes for 50 MeV proton-induced fission of ^{238}U. The red diamonds are from [14] and the data from the present work is indicated as black points. The uncertainties of the present work include statistical and decay corrections. The statistical uncertainties in [14] are small and they are effectively screened by the size of the data points.

linking process, the difference may be a result of unobserved yield fluctuations. Due to this difference, the data points of $^{94-95}$Rb were not used in the normalization of the present distribution to the cross-section values given in [14].

Cesium isotopes from 50 MeV proton-induced fission

In this work, the yields could been deduced only for $^{137-146}$Cs isotopes since the measurements of the lighter Cs isotopes were influenced by the most abundant stable xenon isotopes, $^{128-132,134,136}$Xe. The xenon gas is used in tuning and calibration of the mass separator facility and hence it was intentionally added to the helium gas. Residual xenon gas was then ionized by energetic fission fragments inside the ion guide. The intensity of the xenon isotopes was high enough to cause a space charge effect inside the Penning trap, effectively preventing a proper purification of any other isotopes sharing the same mass number. In the masses of $A = 133$ and 135, Cs mass peaks overlapped with the peaks of Ba and Xe, now attributed to the fission reaction. It was impossible to interpolate the yields from neighboring isotopes since they could not be deduced due to the stable xenon isotopes.

The deduced yield distribution for $^{137-146}$Cs is shown in Fig.3.26. The results of this work are normalized to the independent fission cross sections reported in [14] by using Gaussian fits. Due to the asymmetric nature of the yield distribution, only the neutron rich wings were used in the fit. The agreement between the results is reasonably good. The large uncertainty of ^{137}Cs in the present work is due to the overlap with the mass peak of ^{137}Ba, which was resolved by a relatively inaccurate Gaussian fit. The yield of ^{146}Cs is based on a very poor mass peak lying on a high background level, which results in a relatively high uncertainty for this data point.

3.9. Discussion

3.9.1. Advantages of the method

The goal of this work was to develop a new method for a rapid, accurate determination of the isotopic fission yield distributions. The previous works have been mainly limited to highly volatile elements produced in thick target systems or have been hindered by inaccurate and slow yield detection methods in the IGISOL-based system. The introduced method is a successful combination of the features of the previous works. The non-selectivity of the IGISOL method has been coupled to the unambiguous particle identification ability of JYFLTRAP. This combination, used together with high efficiency MCP detectors, provides a fascinating and fast tool for the studies of isotopic yield distributions of fission reactions.

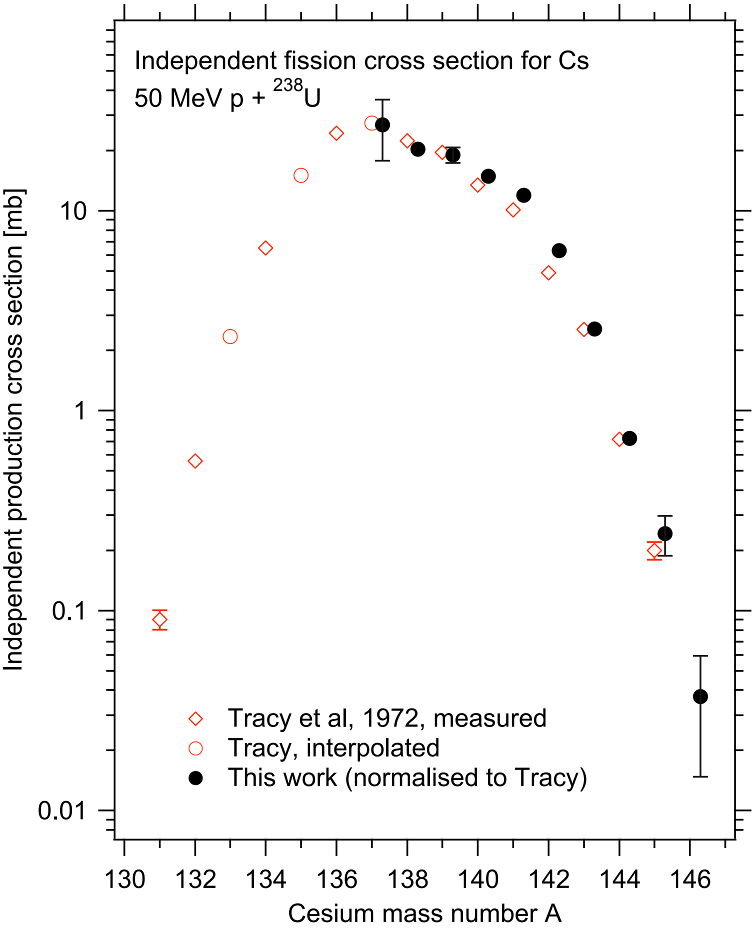

Figure 3.26.: The independent yields of neutron rich Cs isotopes in 50 MeV proton-induced fission of ^{238}U. The red diamonds are from [14] and the open red circles are interpolated values. The uncertainties of the present work (the black points) include statistical uncertainties as well as applied decay corrections. For the data of [14], only the statistical uncertainties are used.

The applicability of the method is highlighted in the chart of the measured masses shown in appendix C; yields of about 300 isotopes were measured within roughly a month of beam time. Following the development of the new techniques, the analysis time of measured data is significantly shorter. Moreover, the analyzing time can still be reduced by improving the data sorting program. There are still many manual steps, such as decay correction and error analysis, that can be applied to the analyzing software.

The reliability of the method has been tested in several ways. It has been shown that the results are reproducible from one experiment to another and that the selection of the reference isotopes does not play a significant role. The results of previous experiments with and without the IGISOL facility are in reasonable agreement. The accuracy of the method should be very good as can be observed from some distributions shown in this work. In many cases however, a higher accuracy could not be reached due to the unexpected short-term yield fluctuations. Some of the present drawbacks have already been resolved and others are still waiting for a solution.

3.9.2. Known problems of the method

Yield fluctuations and mass selectivity of the measurement facility

Several measurements in this work were disturbed by the short-term yield fluctuations. These fluctuations have been traced to an unstable operation of the manual control system of the dipole magnet. This problem has been addressed by a new, computer based digital control system, which is able to provide an accuracy of a few hundredths of mass units over a time period of several hours.

The mass range of the JYFLTRAP facility and especially that of the RFQ has been studied in separate works and is stated to be sufficient over a significantly larger mass range than required for this work. However, the mass dependencies of the IGISOL front-end could not be studied in the present experiments due to the fluctuation of the dipole magnetic field. In principle, some mass dependency is caused by each active element of the IGISOL front-end; the ion guide, the SPIG and the mass separator. This mass dependence of the transmission efficiency introduces an additional uncertainty in the final results. The comparison of the data between the present and previous works reveals that the contribution to the total uncertainty must be rather small. Moreover, this uncertainty is mainly systematic in nature and hence it can be treated, at least partially, by a careful calibration of the measurement facility. The mass dependence of the IGISOL front-end and mass separator will be studied in forthcoming fission yield distribution experiments.

Stable isotopes and molecular beams

Although the helium gas is additionally purified by a LN_2 cooled cold trap, the presence of gas impurities cannot be fully removed. After purification, a trace amount of impurities such as oxygen, nitrogen and water as well as noble gases Ne, Ar, Kr and Xe still exists in the buffer gas. Due to these impurities, molecular ions can be observed in almost in any mass number, especially at the lower masses. As long as the intensity of the molecular beam is not sufficient to exceed the charge handling capacity of the JYFLTRAP system, these beams can be tolerated.

Compared with molecules, more problematic are the gaseous stable isotopes that are ionized inside the ion guide. Noble gases cannot be efficiently removed from the buffer gas even by the cold trap. In addition to the impurities of the helium gas, Ar and Xe are often used as calibrants for the mass separator and therefore are intentionally mixed with the helium gas [123]. Noble gases do not favor formation of molecular compounds and therefore the mass differences to neighboring isotopes are usually very small. Moreover, the beams produced by these impurities are typically very intense causing space charge problems. In this work for example, stable xenon isotopes effectively prevented the mass scans of isobars $A = 129$, 130 and 132. This situation can be improved by avoiding or limiting the use of such calibration gases. It was estimated that about an order of magnitude reduction of the xenon concentration could have been enough to avoid most of the problems.

Also, non-gaseous stable isotopes were observed in excess of their expected production in fission. Unlike the gaseous isotopes, their abundances are significantly weaker, often less than the most abundant fission isotope of the same isobar. For example, the observed yield of stable ^{80}Se was about 20 times higher than that of neighboring ^{81}Se, produced only in fission. It was, however, lower than the yield of ^{84}Se, the most abundantly produced selenium isotope in 25 MeV proton-induced fission of ^{238}U. A correction due to the stable isotopes is possible to some level since their natural abundances are often precisely known. If the excess of even one stable isotope can be deduced, the required correction can be estimated for the other stable isotopes of the same element. In the case of ^{87}Rb, the correction was based on the excess observed in the yield of ^{85}Rb and the known abundance ratios of stable rubidium isotopes. An enhancement was observed in the yields of stable isotopes of Se, Br, Rb, Mo, Cd and Ba. For Sn and Sb, there was only a weak indication of yield enhancement of stable isotopes.

One concern was whether the presence of stable isotopes might be a sign that the decay products of the fission fragments remaining in the walls of the ion guide would return to the gas phase, be ionized by the plasma and finally be observed as known for some β-recoil daughters. Fortunately, the observed excesses strictly followed the natural abundances of the isotopes. Since no clear sign of enhancement was observed in the yields of the long-lived isotopes, the excesses were likely due to a contamination of stable isotopes instead of accumulated fission products. The sources of the additional stable isotopes are thus far unknown. Some of them might be sputtered from the nickel foil by energetic fission fragments. According to the manufacturer however, the impurities in the nickel foil do not match with the observed elements.

3.9.3. Unresolvable isotopes

If the isomeric cases are excluded, about 30 overlapping mass peaks were observed among the measured 294 isotopes. Some had been separated sufficiently such that they could be resolved by a multipeak fitting algorithm. However, other mass peaks were lying so close to each other that they could not be separated even by a fit. These unresolvable mass peaks typically belong to adjacent isotopes located close to stability, wherein the mass differences are very small. From the point of view of fission yield distributions, those isotopes are not the most interesting cases. It is, however, possible to improve the mass resolving power of JYFLTRAP by increasing the purification time or by using a recently developed Ramsey cleaning technique [124]. A direct consequence of changes in trap settings and in purification time is that the equal treatment between long and short-lived isotopes is lost. This is mainly due to the chemical reactions that are heavily time-dependent. As long as the study is only focused on the isotopic yield distributions, these changes can be corrected by a proper calibration of the measurements. For example, two unequal measurements can be reasonably matched if a sufficient overlap between the measured isotopes can be guaranteed.

From the aspect of the yield distribution, isomeric states are not a significant problem as they are usually counted with the ground state. Therefore, there is no need for a high quality separation. Problems arise however, if the half-lives of short-lived isomeric states clearly differ from each other. In such cases, separation of the isomeric states is required for a sufficient decay correction. If the mass peaks of close-lying isomeric states cannot be resolved from each other, the only possibility is to use information about the population ratios of the states produced in fission. Unfortunately, these ratios are not usually precisely known if at all. If Ramsey cleaning is utilized, isomeric states with an energy difference greater than 200 keV should be easily separated. This makes it possible to determine the population ratios of many isomeric states, including the case of ^{120m}Ag discussed in Section 3.7.4. Moreover, once these ratios have been determined during the same experiment as the yield distributions, the uncertainties due to different decay parameters are reduced.

The Ramsay cleaning technique is not limited only to long-lived isotopes. This technique can be even faster than the conventional purification method used in this work, allowing thus a better purification efficiency for the more exotic species. It is hence worth studying the applicability of the Ramsey cleaning method for yield determination in future experiments.

3.9.4. Future developments of the method

The computer software that was developed for sorting and handling raw fission yield data is limited in many ways. This software was developed in a very early phase of the experiments when accurate requirements for the data processing were not precisely known. Presently, there are many procedures in the analyzing process that need to be performed manually. For example, the decay correction, error estimations as well as the virtual reference method, can be directly applied to the computer code reducing the time required for the data analysis.

The IGISOL move to a new experimental hall connected to a new MCC30/15 high current light-ion cyclotron opens up new possibilities for this method. Even though there are no major improvements planned for the front-end of IGISOL in the first stage of the move, the high current light-ion beams provided by the new cyclotron make it possible to increase the production rate of the fission fragments up to the capacity of the present fission ion guide. In many cases, the saturation of the production has been already reached with the beam intensities provided by the present K130 cyclotron. This means that, without further development of the ion guides, the full benefit of the high intensity beams cannot be exploited. The maximum beam intensity of the new MCC30/15 cyclotron can, however, be used in indirect reactions, whereby the secondary beams are used as inducing projectiles. The most interesting example of such a case is the use of a neutron converter, in which an adequate neutron flux is produced via neutron emitting reactions by bombarding suitable target material with a high intense proton or deuteron beam. This allows the extension of the studies of fission yield distributions covering neutron-induced fission reactions. Such reactions are most interesting since they have many direct applications in the field of nuclear energy production and safety.

Advanced beam monitoring and distribution systems offer a change to the on-line monitoring of the yields during the measurements of studied isotopes. Hence, it will be possible to trace the fluctuations of the beam in parallel with the measurement of the isotope of interest. This will eliminate the need for determination of the virtual reference in such cases wherein a significant fluctuation occurs. In addition to the aforementioned Ramsey cleaning method, the mass resolving power of JYFLTRAP can be improved by upgrading the JYFLTRAP facility. In the new measurement hall, available space has been reserved for future projects such as a charge breeder and a multi-reflection time-of-flight mass spectrometer (MR-TOF-MS) [125].

A. SPIG control system

A.1. An overview of the control system

The SPIG system and its electronics are located in a very hazardous area. Due to the high voltage platform of the IGISOL front-end and relatively high radiation level, a local tuning of the SPIG and the front-end parameters is impossible. In order to control the SPIG parameters during an on-line experiment, a proper remote control system is required. Due to the high voltage platform, the remote control system must be optically isolated from the ground voltage platform. Since the IGISOL facility is also used to test new ion guide designs that often require additional parameters, the expandability of the control system is also essential. Several options that offer both easy optical isolation and scalability are commercially available and one of them is a modular WAGO I/O system [126], which was selected as the basis of the SPIG remote control. A schematic illustrating the principle of this remote control system is shown in Fig.A.1.

The control system can be divided into two separate sections: a ground platform containing a computer and optical fiber repeaters and a high voltage platform, which contains the WAGO I/O system, a function generator and a second set of optical fiber repeaters. The communication between ground and high voltage occurs via USB (Universal Serial Bus) [127] and CAN (Control Area Network) [128] buses, both isolated with optical fibers. The USB bus is mainly used to adjust the function generator but the network can be extended to other USB devices, such as stepper motor interfaces, for example. The CAN bus is used to communicate between the WAGO I/O system and the control computer only. It would be possible to extend the CAN network to cover other devices, though the CAN network is not very commonly supported by the laboratory electronics.

A.2. Ground section

A.2.1. Computer interface

The computer section has been realized with two separate programs: a user interface program and a CAN server program. Both programs were built using the National Instruments LabView software developing package [129].

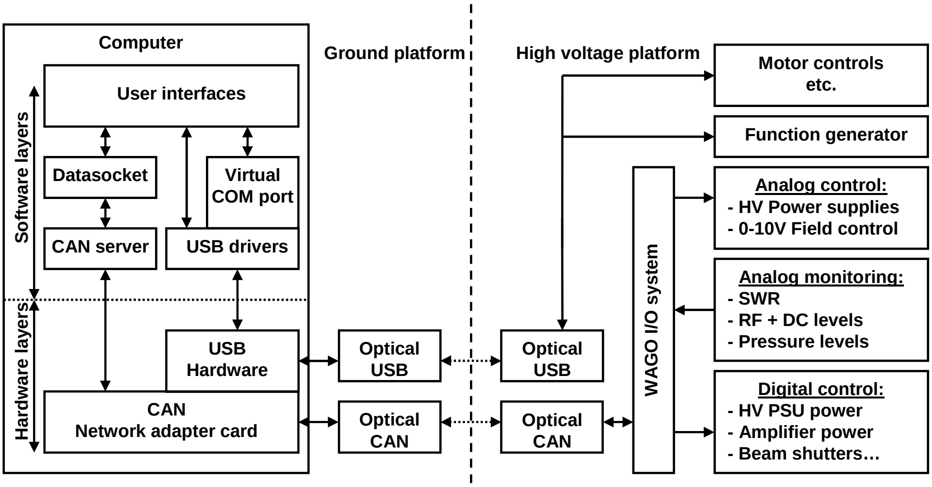

Figure A.1.: A schematic of the SPIG computer-based control system.

The CAN server program, named as “LIST server.vi”, together with a datasocket server, a built-in feature of LabView, forms a link between the CAN network hardware and user interface programs (see fig.A.1, left side). It continuously communicates with each device applied to the CAN network, updates the data related to the device operation and exchanges this data with different user interface programs. It is thus a very useful tool for the system, in which the resources of certain network devices have to be shared between several interface softwares. At the moment, this is option is not needed in the SPIG control system since only one user interface software is used to control all devices in the network. Nevertheless, this feature has been added to the control system for future needs.

An actual user interface software, which carries name ’LIST vista’, is shown in Fig.A.2. This program permits users to adjust all necessary SPIG parameters. It also shows all monitored parameters of the front-end. As can be observed from Fig.A.3, this program communicates with the WAGO system via the datasocket server and the "list server" program. There is, however, a parameter group excluded from the WAGO system. This group contains all rf parameters. Since many modern function generators have been equipped with the USB interface only, it is a natural choice for the communication channel. The USB devices typically generate virtual ’com’ ports inside the computer (see Fig.A.3) that are visible as standard serial communication ports for the user interface softwares.

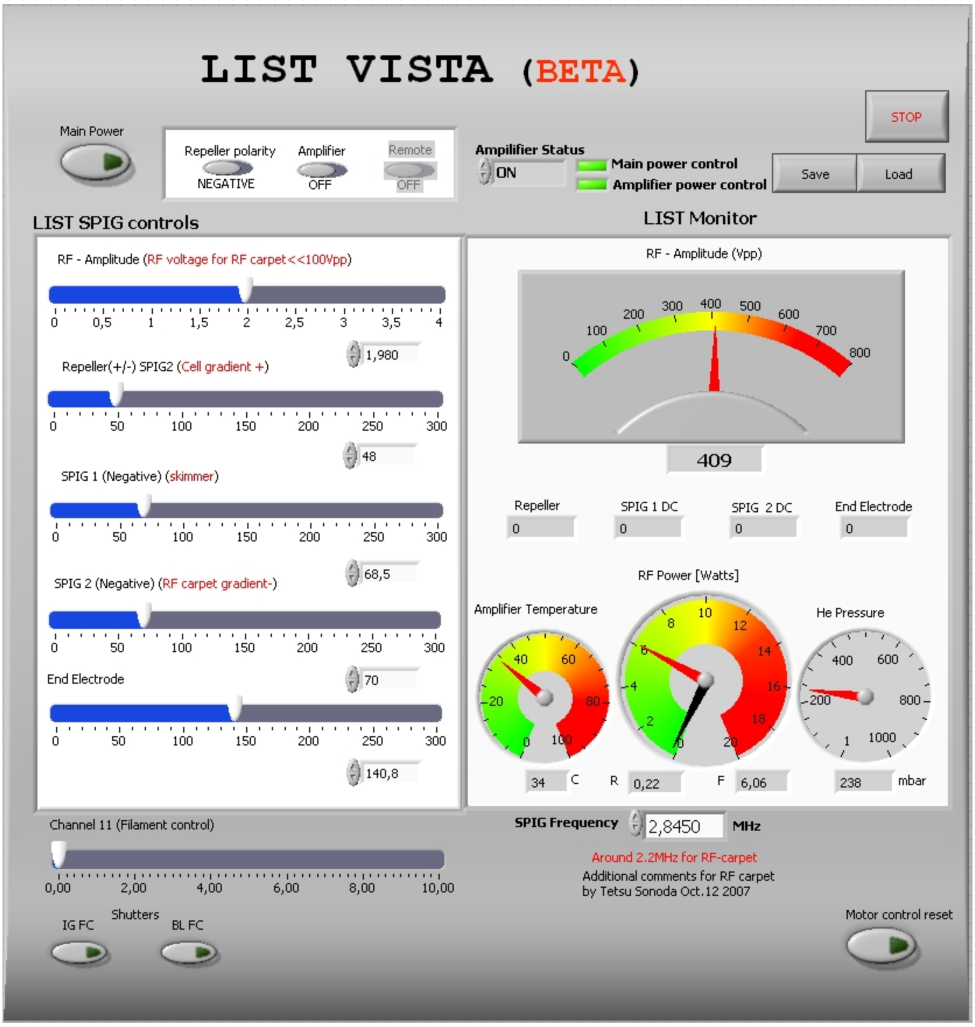

Amplifier Status ON

RF - Amplitude 1,980

Repeller(+/-) SPIG2 48

SPIG 1 (Negative) 68,5

SPIG 2 (Negative) 70

End Electrode 140,8

RF - Amplitude (Vpp) 409

Repeller 0

SPIG 1 DC 0

SPIG 2 DC 0

End Electrode 0

Amplifier Temperature 34 C

R 0,22

F 6,06

He Pressure 238 mbar

SPIG Frequency 2,8450 MHz

Around 2.2MHz for RF-carpet

Additional comments for RF carpet
by Tetsu Sonoda Oct.12 2007

Figure A.2.: A screen shot of the SPIG control program, LIST vista. All SPIG-related electrical parameters can be adjusted via this program (white panel at the left side of the figure) it is used to monitor the most important values of the SPIG operation (the white panel at the right side of the figure). In addition to the SPIG control this program can be used to control many other peripherals that may be needed in various experiments (filament heating control, shutters etc.)

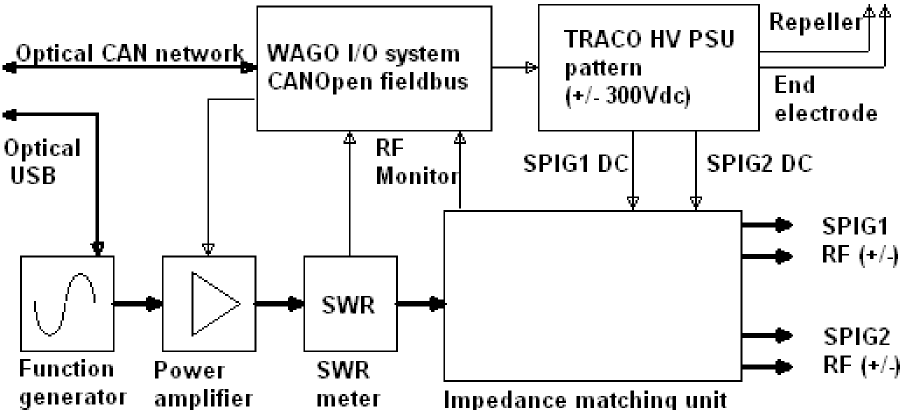

Figure A.3.: A schematic presentation of the SPIG rf and dc system. The lines between the components illustrate signal paths and the arrow heads of the lines indicate the data flow direction.

A.3. High voltage section

The high voltage section is located on the high voltage platform of IGISOL. As shown in FigA.3, this section contains the rf system, high voltage dc power supplies and the WAGO I/O system. The main components of the rf system are introduced in Table A.1.

A.3.1. RF system

The rf system of the SPIG consists of a function generator, an amplifier, an SWR (standing wave ratio) meter and an impedance matching unit. A sinusoidal signal is created with the function generator, directly controlled by the computer interface via the optical USB bus. The signal is amplified with a 300 W power amplifier. Even though the actual power requirement of the rf signal is much smaller, ~10 W at maximum, more powerful broadband amplifiers are easily available at lower cost.

The impedance of the SPIG system is mainly formed by capacitive couplings between the rods of different phases and between the rods and other electrodes. This capacitive impedance may slightly vary due to changes of ambient conditions. This variation is usually harmless but may sometimes cause small shifts to the resonance

Table A.1.: Main rf and dc components of the SPIG system.

Component	Model
Function generator	Agilent 33210A
Amplifier	KL501A
SWR meter	Daiwa CN101L
Impedance matching	'in-house' design
SPIG dc power supplies	Traco MHV12-300
End electrode power supply	Spellman MP1N

frequency of the impedance matching unit. Because of this, the amplified signal is transmitted to the impedance matching unit via the SWR meter, which is used for tuning and monitoring the quality of impedance matching. The selected SWR meter is able to deduce the power of both the fed and reflected rf signal. This power information is also available as analog signals for the WAGO system (see A.3.4) and therefore the SWR meter can be also used as an additional check of the existence of the rf signal.

In the impedance matching unit, the output impedance of the amplifier is matched to an input impedance of the SPIG system in such a way that the SPIG operates in a resonance mode. In addition to this, the rf signal is split into two opposite phases. Each phase is then divided into two dc - isolated rf signals, which are then superimposed to corresponding dc voltages. As a result, four separate rf signals carrying two different phases and voltage levels are sent to the rods of SPIG system. The impedance matching unit also contains a so-called "amplitude to dc" converter that can be used to monitor the rf amplitude. The operation of the impedance matching unit is described more in detail in section A.3.2.

A.3.2. Impedance matching

For a MHz range signal, the impedance of the SPIG is of order several kilo-ohms, which clearly differs from the 50 ohm output impedance of the amplifier. Since the rf signal can not be efficiently transferred over such a high impedance difference, an impedance matching between the amplifier and the loads is needed. In this case, the impedances are matched using "point-like" impedance matching, which generates a narrow resonance frequency band for the optimal signal transfer. A schematic of the impedance matching circuit is shown in Fig.A.4

The heart of the impedance matching unit is the impedance transformer T_1. It

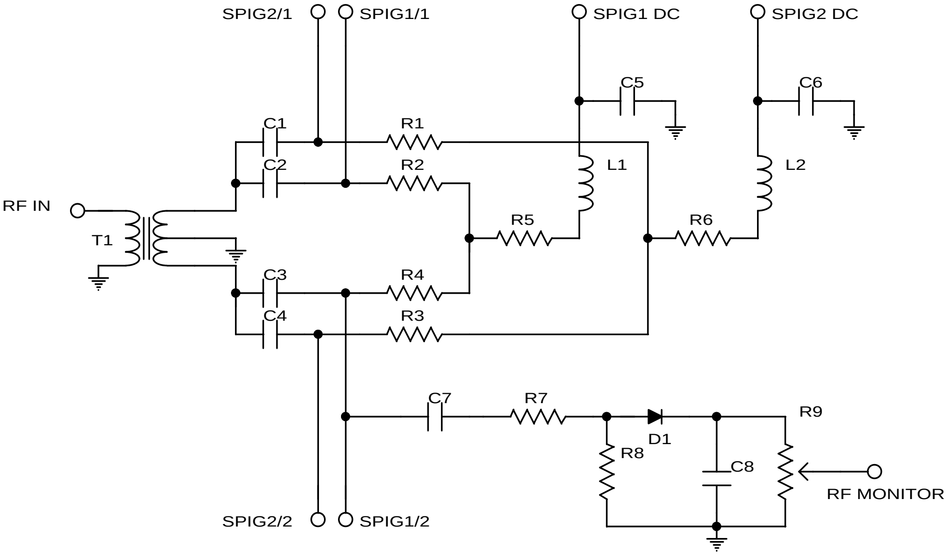

Figure A.4.: A schematic of the impedance matching circuit. Only one of two rf-dc converters is shown in the figure. A second identical converter appears in the SPIG1/1 (= First SPIG, phase 1) line.

consists of two T-200 iron powder cores wound with 2 mm thick enameled copper wire. A total winding ratio of the transformer typically varies from 1:14 to 1:20 (∼2 - 4 Mhz) depending on the desired resonance frequency. As shown in Fig.A.4, the primary side of the transformer is directly coupled to the incoming rf signal (from the SWR meter) while the secondary side is divided into two equal sized coils. These coils are connected in series and the connection point is grounded. Such a structure divides the rf signal into two separate signals with equal amplitudes but opposite phases. Those signals are later superimposed to the dc levels and finally coupled to the SPIG rods.

Capacitors C_1-C_4 are nearly invisible to the rf signals but they prevent the dc currents flowing to the ground through the transformer windings. Resistors R_1 - R_4 in turn limit the current flow between the opposite rf phases and resistors R_5 - R_6, together with simple low pass filter structures (L_1, C_5 and L_2, C_6), reduce the visibility of the rf signal towards the dc power supplies. The impedance matching unit also contains two "amplitude-dc" converters, of which only one is shown in Fig.A.4. These converters do not play a significant role in the impedance matching process. Instead, they are only used to monitor the amplitude of the rf signal fed to the SPIG rods. Each converter unit includes a tank capacitor (C_8), which is loaded on every positive rf cycle via a fast rectifier diode (D_1). Resistors before the diode (R_7 and R_8) can be used to reduce the rf amplitude to within the operational limits of the tank capacitor. In addition to this, resistor R_7 limits the visibility of the tank capacitor towards the actual rf circuit. Capacitor C_7 blocks the DC - component that was earlier superimposed to the rf signal and trimmer R_9 provides a fine tuning and calibration for the conversion result. Due to the non-linearity of the rectifier diode at small voltages (< 0.7 V), the operation of this converter is not very accurate at low amplitude levels. When the rf amplitude increases, the operation of the rectifier diode becomes more linear and the converter provides a rather good estimation for the rf amplitude.

A.3.3. DC system

The SPIG system contains several dc levels that are used to provide an axial acceleration for the ions. All power supply units (PSU) can be controlled with an analog reference voltage provided by the WAGO system. The accuracy requirement of these dc levels is not very strict and thus a low cost Traco MHV12(±)300 (± 300 V, 2.5 W) PSU was selected as a basis for the SPIG voltage platform. The only exception is the end electrode voltage, which is provided from a Spellman MP1N (-1 kV, 10 W) PSU. This power supply is also used to provide the skimmer voltage when installed. Two Traco PSU are used to provide the negative voltages for the

SPIG rods. The same voltages are also provided to the metallic covers of the SPIG elements in order to minimize the dc gradient between the rods and the covers. The LIST operation requires a polarity control of the repeller voltage. This is realized with two separate PSU of which one provides a positive and the other a negative voltage. Both voltages are controlled with the same reference voltage. The polarity of the repeller electrode can be selected with a mechanical relay, which can be controlled via the WAGO system.

A.3.4. WAGO I/O system

The modular WAGO I/O system has a quite long history within the IGISOL facility. It was first applied as a part of the JYFLTRAP control system [130]. A similar WAGO package was later adapted to the vacuum control system of the IGISOL front-end, which was developed during the major upgrade of the IGISOL facility in 2003 [131]. The CAN network of the vacuum control system was later expanded to the high voltage region of the IGISOL front-end, making it possible to use the WAGO system also in the control of the SPIG system.

The WAGO I/O system selected for this work is based on the modular WAGO 750 series. A fully working I/O system consists of at least a fieldbus coupler unit, one or more I/O modules and an end module. The fieldbus coupler unit takes care of the data transfer between a master device (computer in this work) and the I/O modules. The selected unit (750-337) translates CANOpen messages into internal fieldbus commands for the I/O modules and vice versa. The end module terminates the internal data bus (fieldbus) of the WAGO system, which is used to control the I/O modules. The I/O modules in turn convert internal fieldbus commands from the fieldbus coupler to the physical signals (outputs) and vice versa (inputs).

One fieldbus coupler unit can control no more than 256 digital or 64 analog I/O modules. Module types can be freely mixed in such a way that the WAGO I/O module system may contain several digital and analog inputs and outputs as well as thermocouple readers, serial interfaces and so on. The modules used in the control system of the SPIG are tabulated in TableA.2.

The WAGO 750 series supports many kind of physical signal interfaces, which makes it an easily scalable solution for various control purposes and applications. Expandability of the control system is a crucial feature for IGISOL case, since the front-end assembly often varies from one experiment to another.

Table A.2.: The I/O modules of the WAGO 750 series that are used in the SPIG control system.

Module type	**Description**	**Use**
750-337	CANOpen fieldbus coupler	Main unit of the system
750-519	4 ch, 5 V digital output	TTL level control of : -Solenoid arms -Voltage switches
750-504	4 ch, 24 V digital output	Repeller polarity Power state control of : -Amplifier -DC PSU's
750-468	4 ch, 0-10 V analog output	DC PSU control 0 - 10 V field control for items
750-559	4 ch, 0-10 V analog input	Monitoring of : -DC levels -RF power/amplitude -Gas pressure
750-612	Supply module 0-230 V	+5 V power supply for 750-519
750-600	End module	Fieldbus termination

B. SPIG trouble shooting

Even though the SPIG control system is quite simple, a lot of effort for tracing and fixing possible problems may be required. Therefore, some solutions for the most typical problems are given in this chapter.

B.1. Typical reasons of failures

The most typical sources of the failures are high voltage discharges of the IGISOL front-end. The seriousness of the discharge damage depends on the location. If a device of the control system is directly exposed to the discharge, it most probably breaks.

Another source is the aging of the control devices due to a high radiation level, an intensive usage or just time. In these cases it is often very difficult to identify the reason of the problem, since the devices are not actually broken. Especially in the case of radiation damages, devices may operate in a correct way when tested, but malfunctioning occurs over a significantly longer period of use. The damaged devices can be only rarely repaired and in many cases, the only solution is to replace the damaged device.

B.2. Tracing and fixing problems

In order to make the tracing of the problems easier, the control system can be roughly divided into four different sections: a computer, communication, control electronics and the SPIG (including the impedance matching unit). Typical problems and solutions of each section is given below.

B.2.1. Communication related problems

Both communication channels, CAN and USB, are isolated using optical links. Failures in the CAN bus are quite rare. However, the USB bus is very sensitive to the IGISOL high voltage platform. Network failures occur every now and then due to a non-robust design of the bus.

The most problematic issue related to USB is the complexity of the protocol it uses. The plug and play feature associated with the hardware of USB automatically executes many processes when the device is applied to the computer. In practice this means that after any failure, the USB device needs to be physically reinstalled to the computer before these automatic processes will be executed. USB related problems are the most typical for the present control system. Fortunately, they usually are also quite easy to identify and solve. When a USB network failure appears, any USB related action (an attempt to change the rf parameters, for example) results in an error message. If the problem is a pure communication failure without any physical damages in the hardware the following steps should restore the connection:

1. Turn off the LIST Vista control program by pressing the “stop” - button of the program (not the "‘stop"’ button of the LabView engine).
2. Initialize the USB connection by unplugging and replugging in the USB cable.
3. Restart the LIST Vista program.

After these steps, the USB connection should be operational again. If not, the reset of the function generator may be required before the USB cable is plugged back to the computer. If the problem still exists, it may be related to the function generator, the optical isolator or the USB bus hardware. In such a case, it can be traced by testing these apparatuses separately with USB devices and interfaces that are known to be working correctly.

CAN related failures are quite rare but sometimes they may occur due to discharges of the IGISOL high voltage or lose connections of the CAN cables. The majority of CAN network errors are indicated as a red “X” mark in the “CAN Out” frame of the LIST server software. Another sign of the CAN communication problem is that none of the WAGO-based indicators are alternating or showing reasonable values. Sometimes, it may be enough to reset the LIST server software by pressing the “Control” button twice and starting the server again by pressing the white arrow button. This should help if the problem was related to failure of the server program. If the problem is related to the network or WAGO I/O failure, a full reset of the control system is needed. This can be done as follows:

1. Turn off all LabView related programs including also the LabView engine and the datasocket server.
2. Turn off the WAGO I/O system, located in the cave downstairs of the IGISOL, by shutting down the associated KERT power supply.
3. Wait until all led indicators in the WAGO system have gone out and restart the power supply again. (Note that the 5 V digital outputs are fed via separate

power supply, so the led indicators associated to these outputs may not be affected by this operation).

4. Start the IGISOL vacuum control system by clicking the IGISOL vacuum start shortcut. Then, start the LIST server and Vista programs.

Once these steps have been strictly followed, the red “X” mark in the “CAN Out” frame should turn to a green “V” mark indicating that the communication system is operational again. If this does not happen, the problem is most likely related to the CAN hardware (CAN interface card, optical repeaters or cables) or the WAGO I/O system or the both. In order to identify the problem, those devices need to be tested separately with CAN devices and interfaces that are known to be working properly.

B.2.2. Hardware related problems

Unlike the communication problems, the hardware related problems of the SPIG control system are quite unusual. The most sensitive parts are modules of the WAGO I/O system, particularly +10 V analog inputs that are directly used in the monitoring of the SPIG rf - parameters. The first step of solving these problems is to understand whether the problem is related to the rf or the WAGO section of the control system. Sometimes, if the origin of the problems has been the discharging of the high voltage both sections may have been damaged.

If the failure is related to the DC levels or the monitoring of the SPIG parameters (e.g. voltage levels do not properly respond to the control or unexpected values are shown in the monitoring screens) the problem is most probably related to the WAGO system. In such a case, the damaged part may be either the discrete I/O channel or module of the WAGO system or the device being controlled or monitored. The damaged part can be traced by disconnecting the faulty device from the WAGO system and by measuring the output signal from the device (in the case of monitoring failure) or measuring the output signal of the WAGO output channel (in the case of control failure). If the problem is related to the WAGO I/O failure, it can be repaired by replacing the broken module with a working one, or by using some other free and working I/O channel. In the latter case, a new channel must be separately defined for the control software. If the problem cannot be repaired by replacing the suspected WAGO modules and if the devices applied to the WAGO system work properly, it is worth to test the functionality of the WAGO fieldbus coupler unit and the CAN network system including optical isolators, power supplies and CAN interface hardware.

If the problem is related to the rf - section, it usually results in poorly matched or fully missing rf - signal. The easiest way to check this is to read the rf power values directly from the SWR meter. Since the computer monitoring of rf-power is realized with the WAGO system, this eliminates the possibility of WAGO failure. If there is a reason to suspect that the SWR meter itself is damaged, the presence of the rf signal can be verified by measuring the amplifier output with an oscilloscope having a 50 ohm termination. In the case where the rf signal has been totally lost, the problem is in the function generator or the amplifier or both. The resetting of devices and the checking of the operational parameters of the function generator can be done. If this does not solve the problem, testing both devices separately with an oscilloscope and a working function generator. Since the power stage of the rf amplifier is controlled via the WAGO system (+24 V digital output), the lack of the rf signal may also reflect a WAGO problem. The same I/O channel is also used to control the fan of the amplifier and, if this fan is not rotating, no signal is provided from the WAGO system.

B.2.3. The SPIG and the impedance matching related problems

If the rf signal exists but it cannot be correctly matched, the problem may be found from the SPIG structure or from the impedance matching unit. Over the course of time and especially due to the intensive use of discharge and filament ion sources, the surfaces of the SPIG insulators tend to be coated and their electrical insulation becomes worse. Such a slightly conducting insulator between the rf rods increases the risk of rf discharge or in the worst case, leads to an electrical short circuit between the rods. Such problems can be easily avoided by regular cleaning and maintenance of the SPIG apparatus. In addition to the dirty surfaces, impedance matching problems may be also related to loose connections of the cables between the SPIG and the impedance matching unit.

If the problem cannot be solved from the SPIG side, the problem is related to the impedance matching unit. The easiest way fix such a problem is to replace all components of it with new ones. The impedance matching unit is located on the top of the target chamber where it is continuously exposed to a high radiation level. This radiation reduces the expected life time of the components and therefore the stability of the unit can be reasonably maintained only by a regular renewing of the components.

C. Isotopic chains measured in this work

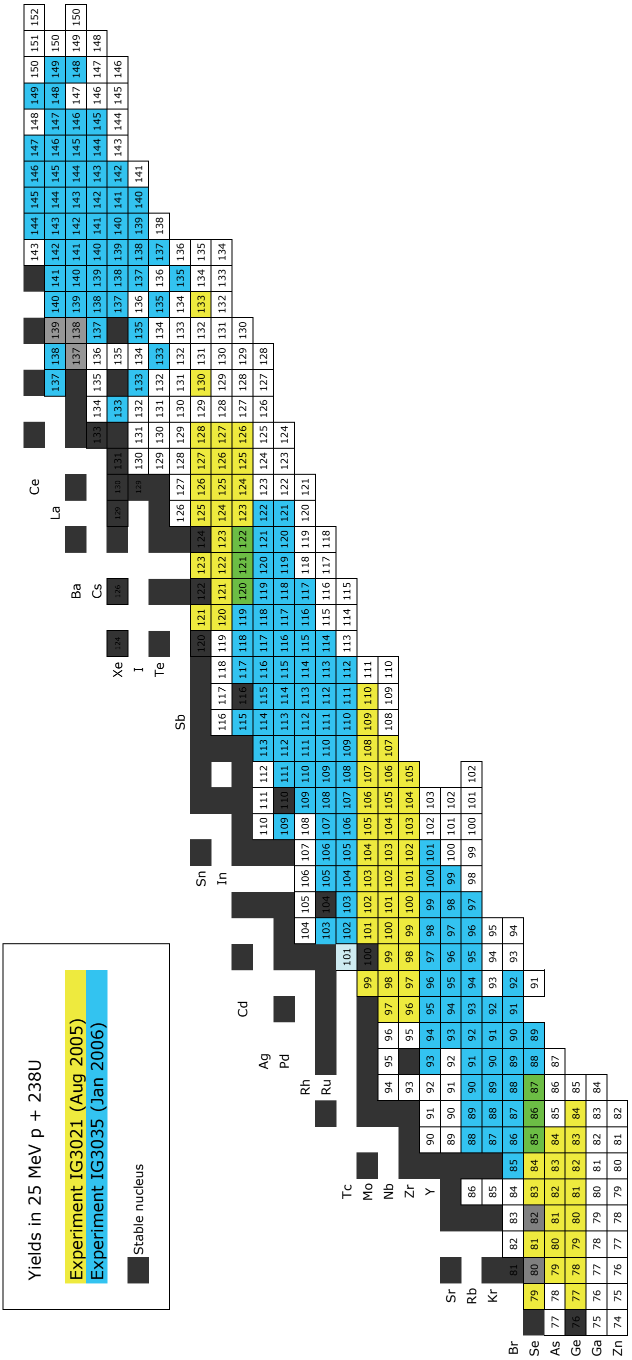

Figure C.1.: Isotopic yields in 25 MeV proton-induced fission of ^{238}U measured in this work.

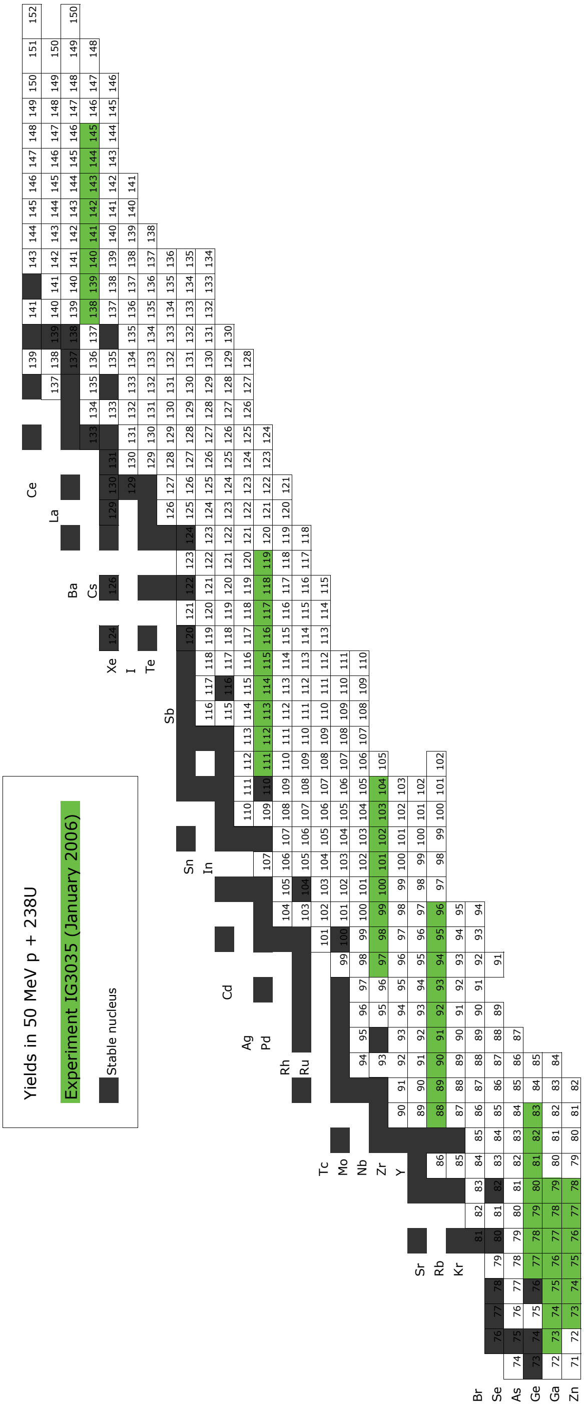

Figure C.2.: Isotopic yields in 50 MeV proton-induced fission of ^{238}U measured in this work.

D. Isotopic chains reported in literature

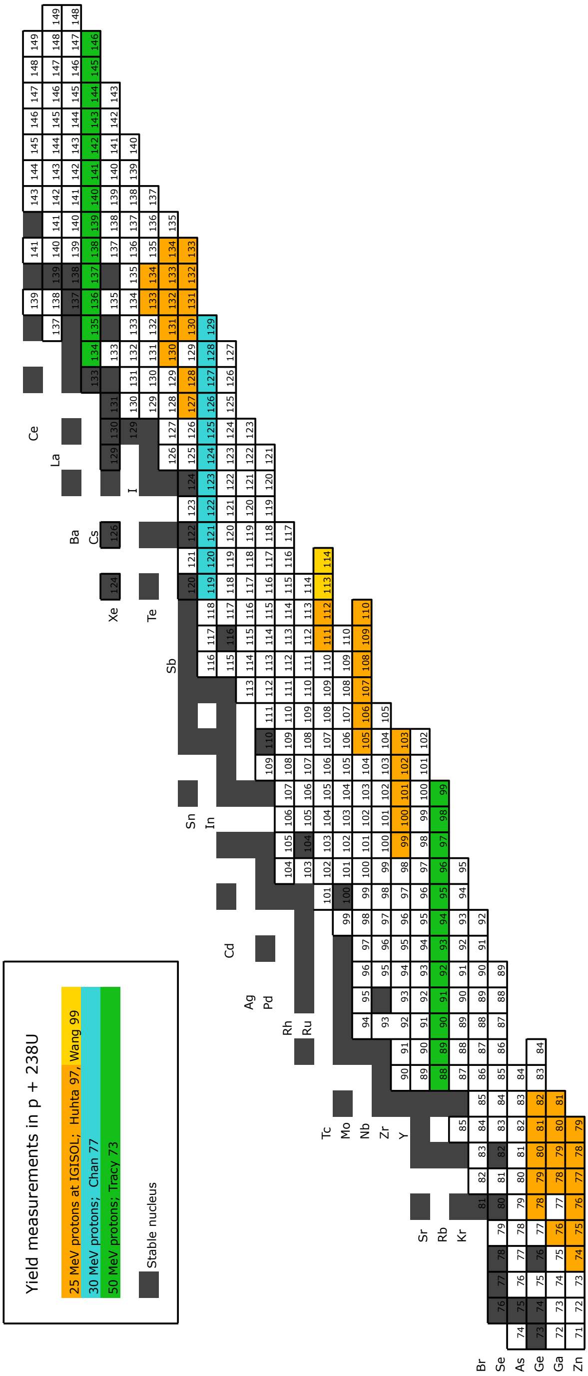

Figure D.1.: Isotopic yields in 25 MeV [85, 86, 88], 35 MeV [13] and 50 MeV [14] proton-induced fission of ^{238}U reported in literature.

Bibliography

[1] J. Ärje and K. Valli, Nucl. Instr. and Meth. **179**, 533 (1981).

[2] J. Ärje *et al.*, Nucl. Instr. and Meth. **186**, 149 (1981).

[3] H. J. Xu *et al.*, Nucl. Instr. and Meth. A **333**, 274 (1993).

[4] K. Blaum *et al.*, Nucl. Instr. and Meth. B **204**, 331 (2003).

[5] I. D. Moore *et al.*, J. Phys. G: Nucl. Part. Phys. **31**, S1499 (2005).

[6] SIMION3D ion optics simulator, <www.sisweb.com/simion>.

[7] V. A. Rubchenya, Phys. Rev. C **75**, 054601 (2007).

[8] Final Report of the EURISOL Design Study, 2009.

[9] Compilation and evaluation of fission yield nuclear data, IAEA-TECDOC-1168, 2000.

[10] Fission Product Yield Data for the Transmutation of Minor Actinide Nuclear Waste, IAEA report, ISBN 92-0-115306-6, 2008.

[11] European Research Infrastructures for Nuclear Data Applications, ERINDA, Fission-2010-4.2.1, 2010.

[12] E. Moll *et al.*, Nucl. Instr. and Meth. **123**, 615 (1975).

[13] K. Chan *et al.*, Journal of Inorganic and Nuclear Chemistry **39**, 1915 (1977).

[14] B. L. Tracy *et al.*, Phys. Rev. C **5**, 222 (1972).

[15] V. S. Kolhinen *et al.*, Nucl. Instr. and Meth. A **528**, 776 (2004).

[16] P. V. den Bergh *et al.*, Nucl. Instr. and Meth. B **126**, 194 (1997).

[17] J. Huikari *et al.*, Nucl. Instr. and Meth. B **222**, 632 (2004).

[18] P. Dendooven, Nucl. Instr. and Meth. B **126**, 182 (1997).

[19] J. Äystö, Nuclear Physics A **693**, 477 (2001).

[20] K. Peräjärvi *et al.*, Nucl. Instr. and Meth. A **546**, 418 (2005).

[21] P. Dendooven, IGISOL web pages, «www.jyu.fi/fysiikka/en/research/accelerator/igisol/ionguide.html».

[22] P. H. Dawson, Quadrupole mass spectrometry and its applications, 1995.

[23] D. Gerlich, *Inhomogeneous RF fields: A verstile tool for the study of processes with slow ions, State-Selected and State-to-State Ion-Molecule Reaction Dynamics. Part 1: Experiment* (John Wiley & Sons, 1992).

[24] U. Köster, V. N. Fedoseyev, and V. I. Mishin, Spectrochimica Acta Part B: Atomic Spectroscopy **58**, 1047 (2003).

[25] K. Wendt *et al.*, Radiochim. Acta **79**, 183 (1997).

[26] F. Schwellnus *et al.*, Nucl. Instr. and Meth. B **266**, 4383 (2008).

[27] T. Sonoda *et al.*, Nucl. Instr. and Meth. B **267**, 2918 (2009).

[28] M. Huyse *et al.*, Nucl. Instr. and Meth. B **187**, 535 (2002).

[29] Y. Kudryavtsev *et al.*, Nucl. Instr. and Meth. B **267**, 2908 (2009).

[30] T. Kessler, Ph.D. thesis, University of Jyväskylä, 2008.

[31] B. Marsh, Ph.D. thesis, University of Manchester, 2007.

[32] T. Kim, Ph.D. thesis, Department of Physics, McGill University, Montreal, Canada, 1997.

[33] A. Kellerbauer, T. Kim, R. B. Moore, and P. Varfalvy, Nucl. Instr. and Meth. A **469**, 276 (2001).

[34] D. A. Dahl, J. E. Delmore, and A. D. Appelhans, International conference on ion sources **61**, 607 (1990).

[35] D. A. Dahl, Int. J. Mass Spectrom. **200**, 3 (2000).

[36] S. Henry *et al.*, Trapped charged particles and fundamental physics **457**, 120 (1999).

[37] A. D. Appelhans and D. A. Dahl, Int. J. Mass Spectrom. **216**, 269 (2002).

[38] L. Ding, M. Sudakov, and S. Kumashiro, Int. J. Mass Spectrom. **221**, 117 (2002).

[39] A. D. Appelhans and D. A. Dahl, Int. J. Mass Spectrom. **244**, 1 (2005).

[40] P. Karvonen *et al.*, Nucl. Instr. and Meth. B **266**, 4794 (2008).

[41] D. Manura, Hard sphere collision model for SIMION3D, <http://www.simion.com/info/Collision_Model_HS1/>.

[42] COSMOSFloWorks 2004 standard SP0. build: 304 Version 2004231.

[43] A. Bondi, Journal of Physical Chemistry **63**, 441 (1964).

[44] Periodic Table,< http://periodictable.com/Properties/A/VanDerWaalsRadius.v.html>.

[45] H. Wiedemann, *Particle accelerator physics, second edition* (Springer-Verlag Berling Heidelberg, 1999).

[46] T. Kessler *et al.*, Nucl. Instr. and Meth. B **266**, 681 (2008).

[47] S. Baba, H. Umezawa, and H. Baba, Nuclear Physics **A175**, 177 (1971).

[48] National Nuclear Data Center, Brookhaven National Laboratory, <http://www.nndc.bnl.gov/nudat2/>.

[49] A. Kankainen *et al.*, The European Physical Journal A **29**, 271 (2006).

[50] P. Ronkanen, Master's thesis, University of Jyväskylä, 2007.

[51] M. Oinonen *et al.*, Nucl. Instr. and Meth. A **416**, 485 (1998).

[52] S. Purushothaman, Ph.D. thesis, University of Groningen, 2008.

[53] W. X. Huang *et al.*, Nucl. Instr. and Meth. B **204**, 592 (2003).

[54] F. Paschen, Ann. Phys. **47**, 177 (1889).

[55] K. T. A. L. Burm, Contrib. Plasma Phys. **47**, 177 (2007).

[56] G. Auday, P. Guillot, J. Galy, and H. Brunet, Journal of Applied Physics **83**, 5917 (1998).

[57] L. Ledernez, F. Olcaytug, H. Yasuda, and G. Urban, A modification of Paschen law for Argon, 29th ICPIG, July 12-17, 2009, Cancun, Mexico, 2009.

[58] M. A. Hassouba, F. F. Elakshar, and A. A. Garamoon, FIZIKA **A 11**, 81 (2002).

[59] J. D. Cobine, *Gaseous conductors: Theory and engineering applications* (Dover Publications, New york, 1958).

[60] I. Pohjalainen, Master's thesis, University of Jyväskylä, 2010.

[61] V. Lisovskiy *et al.*, EPL **82**, 15001 (2008).

[62] M. Reponen, I. Moore, P. Karvonen, and H. Penttilä, Submitted to Nucl. Instr. and Meth. A (2010).

[63] S. Schwarz *et al.*, Nucl. Instr. and Meth. B **204**, 474 (2003).

[64] A. Takamine, M. Wada, and T. Sonoda, RIKEN Accel. Prog. Rep. **40**, 147 (2007).

[65] W. D. Myers and W. J. Swiatecki, Nuclear Physics **81**, 1 (1966).

[66] Interactive chart of nuclides, maintained at the Brookhaven National Laboratories. <http://www.nndc.bnl.gov/nudat2/>.

[67] G. P. Ford and R. B. Leachman, Phys. Rev. **137**, B826 (1965).

[68] M. Petit *et al.*, Nuclear Physics A **735**, 345 (2004).

[69] Evaluated Nuclear Data File, «www.nndc.bnl.gov/endf/».

[70] T. Yoshida, *Assessment of Fission Product Decay Data for Decay Heat Calculations*, OECD-NEA Nuclear Science report NEA/WPEC-25, NEA-no. 6284, 2007.

[71] M. Chadwick *et al.*, Nuclear Data Sheets **107**, 2931 (2006), evaluated Nuclear Data File ENDF/B-VII.0.

[72] JEFF-3.1 Evaluated Data Library Project,
«www.nea.fr/dbforms/data/eva/evatapes/jeff_31/».

[73] Nuclear energy agengy, CENDL library,
«http://www.nea.fr/dbforms/data/eva/evatapes/cendl_31/».

[74] Japanese Evaluated Nuclear Data Library,
«http://wwwndc.jaea.go.jp/jendl/jendl.html».

[75] P. Rullhusen, ed., Nuclear Data Needs for Generation IV Nuclear Energy Systems, Antwerpen, 2005 (World Scientific Publishing Co. Pte. Ltd., Singapore, 2006).

[76] A. Andrighetto *et al.*, The European Physical Journal A **23**, 257 (2005).

[77] S. Manohar, A. Goswami, and B. Tomar, Journal of Radioanalytical and Nuclear Chemistry **203**, 331 (1996), 10.1007/BF02041516.

[78] J. K. P. Lee, G. Pilar, B. L. Tracy, and L. Yaffe, Journal of Inorganic and Nuclear Chemistry **37**, 2035 (1975).

[79] L. Nikkinen, B. Pathak, L. Lessard, and J. Lee, Nucl. Instr. and Meth. **175**, 425 (1980).

[80] C. Lau *et al.*, Nucl. Instr. and Meth. B **204**, 257 (2003).

[81] U. C. Bergmann *et al.*, Nucl. Instr. and Meth. B **204**, 220 (2003).

[82] M. Leino *et al.*, Phys. Rev. C **44**, 336 (1991).

[83] P. P. Jauho *et al.*, Phys. Rev. C **49**, 2036 (1994).

[84] H. Kudo *et al.*, Nucl. Instr. and Meth. B **126**, 209 (1997).

[85] M. Huhta *et al.*, Physics Letters B **405**, 230 (1997).

[86] M. Huhta *et al.*, Nucl. Instr. and Meth. B **126**, 201 (1997).

[87] H. Kudo *et al.*, Phys. Rev. C **57**, 178 (1998).

[88] J. C. Wang *et al.*, Physics Letters B **454**, 1 (1999).

[89] S. Goto *et al.*, J. Radioanal. Nucl. Chem. **239**, 109 (1999).

[90] G. Lhersonneau *et al.*, Eur. Phys. J. A **9**, 385 (2000).

[91] D. Kaji *et al.*, Journal of Nuclear and Radiochemical Sciences **Vol.3, No.2**, 7 (2002).

[92] L. Stroe *et al.*, The European Physical Journal A **17**, 57 (2003).

[93] K. Kruglov *et al.*, The European Physical Journal A **14**, 365 (2002), 10.1140/epja/i2002-10013-1.

[94] J. K. Dickens and J. W. McConnell, Phys. Rev. C **23**, 331 (1981).

[95] J. K. Dickens and J. W. McConnell, Phys. Rev. C **24**, 192 (1981).

[96] J. K. Dickens and J. W. McConnell, Phys. Rev. C **27**, 253 (1983).

[97] A. Oed *et al.*, in *Dynamics of Nuclear Fission and Related Collective Phenomena*, Vol. 158 of *Lecture Notes in Physics*, edited by P. David, T. Mayer-Kuckuk, and A. van der Woude (Springer Berlin / Heidelberg, ADDRESS, 1982), pp. 128–137, 10.1007/BFb0021515.

[98] A. Oed *et al.*, Nucl. Instr. and Meth. **219**, 569 (1984).

[99] G. Diiorio and B. Wehring, Nucl. Instr. and Meth. **147**, 487 (1977).

[100] J. Benlliure *et al.*, EPJ Web of Conferences **2**, 07003 (2010).

[101] V. S. Kolhinen *et al.*, Nucl. Instr. and Meth. B **204**, 502 (2003).

[102] V. Kolhinen, Ph.D. thesis, Department of Physics, University of Jyväskylä, 2003.

[103] G. Gabrielse, L. Haarsma, and S. L. Rolston, International Journal of Mass Spectrometry and Ion Processes **88**, 319 (1989).

[104] G. Savard *et al.*, Physics Letters A **158**, 247 (1991).

[105] A. Nieminen *et al.*, Nucl. Instr. and Meth. A **469**, 244 (2001).

[106] T. Eronen *et al.*, Physics Letters B **636**, 191 (2006).

[107] A. Bey *et al.*, The European Physical Journal A **36**, 121 (2008).

[108] S. Rinta-Antila *et al.*, Phys. Rev. C **70**, 011301 (2004).

[109] U. Hager *et al.*, Nuclear Physics A **793**, 20 (2007).

[110] U. Hager *et al.*, Phys. Rev. C **75**, 064302 (2007).

[111] J. R. Taylor, *An introduction to error analysis: the study of uncertainties in physical measurements* (University Science Books, 1997).

[112] B. Fogelberg, A. Bäcklin, and T. Nagarajan, Physics Letters B **36**, 334 (1971).

[113] M. Tanikawa *et al.*, Zeitschrift für Physik A Hadrons and Nuclei **347**, 53 (1993).

[114] D. G. Madland and T. D. England, Nucl. Sci. Eng. **64**, 859 (1977).

[115] A. Herlert *et al.*, New Journal of Physics **7**, 44 (2005).

[116] A. H. Snell and F. Pleasonton, Phys. Rev. **107**, 740 (1957).

[117] A. H. Snell and F. Pleasonton, Phys. Rev. **111**, 1338 (1958).

[118] A. Nieminen *et al.*, Phys. Rev. Lett. **88**, 094801 (2002).

[119] O. Almen, W. Hartmann, K. Frank, and J. Christiansen, Journal of Physics E: Scientific Instruments **22**, 382 (1989).

[120] P. Karvonen *et al.*, Nucl. Instr. and Meth. B **266**, 4454 (2008).

[121] J. He *et al.*, Rapid Commun. Mass Spectrom. **22**, 3327 (2008).

[122] C. M. Baglin, Nuclear Data Sheets **109**, 2257 (2008).

[123] P. Taskinen *et al.*, Nucl. Instr. and Meth. A **281**, 539 (1989).

[124] T. Eronen *et al.*, Nucl. Instr. and Meth. B **266**, 4527 (2008).

[125] W. R. PlaSS *et al.*, Nucl. Instr. and Meth. B **266**, 4560 (2008).

[126] WAGO Kontakttechnik GmbH, <http://www.wago.com/>.

[127] USB implementers Forum Inc. <http://www.usb.org/>.

[128] Controller Area Network (CAN)-CAN in Automation (CiA), <http://www.can-cia.org/can/>.

[129] National Instruments LabVIEW, <http://www.ni.com/labview/>.

[130] J. Hakala *et al.*, Nucl. Instr. and Meth. B **266**, 4628 (2008).

[131] P. Karvonen, Master's thesis, University of the Jyväskylä, 2004.